



HAL
open science

CFD/DDA coupling for fluid-structure interactions with applications to environmental problems

Dong Ding

► **To cite this version:**

Dong Ding. CFD/DDA coupling for fluid-structure interactions with applications to environmental problems. Mechanics [physics.med-ph]. Université de Technologie de Compiègne, 2021. English. NNT : 2021COMP2597 . tel-03593852

HAL Id: tel-03593852

<https://theses.hal.science/tel-03593852>

Submitted on 2 Mar 2022

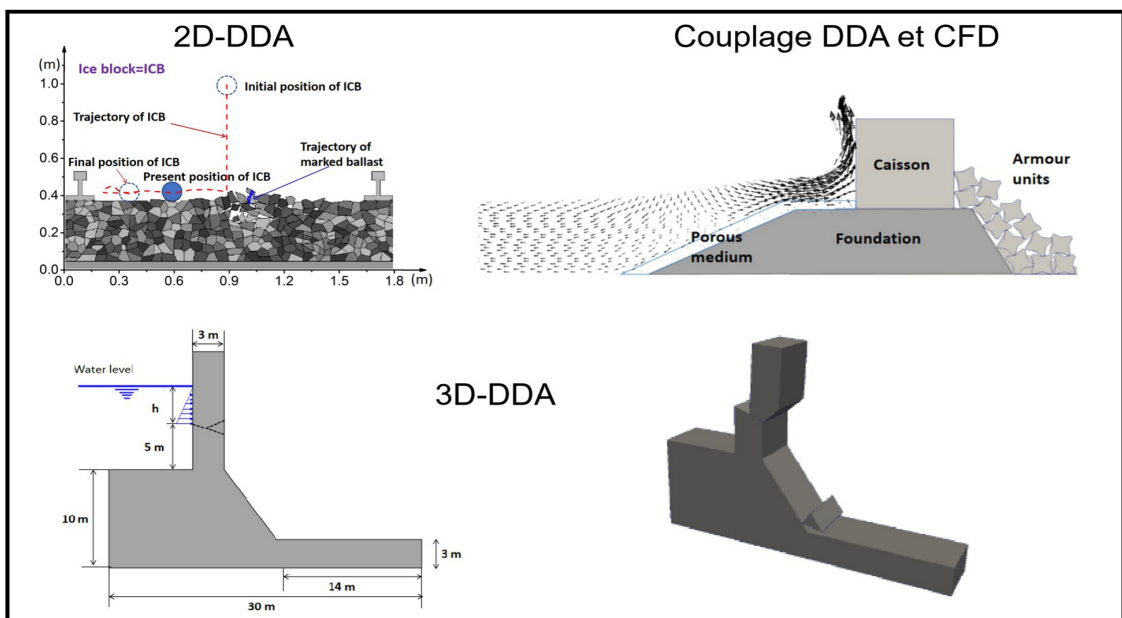
HAL is a multi-disciplinary open access archive for the deposit and dissemination of scientific research documents, whether they are published or not. The documents may come from teaching and research institutions in France or abroad, or from public or private research centers.

L'archive ouverte pluridisciplinaire **HAL**, est destinée au dépôt et à la diffusion de documents scientifiques de niveau recherche, publiés ou non, émanant des établissements d'enseignement et de recherche français ou étrangers, des laboratoires publics ou privés.

Par Dong DING

*CFD/DDA coupling for fluid-structure interactions
with applications to environmental problems*

Thèse présentée
pour l'obtention du grade
de Docteur de l'UTC



Soutenue le 23 mars 2021

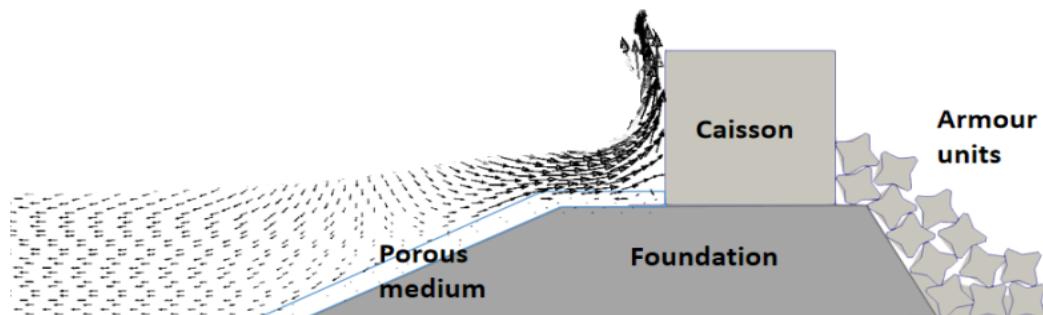
Spécialité : Mécanique Numérique : Unité de recherche en Mécanique - Laboratoire Roberval (FRE UTC - CNRS 2012)

D2597

Dong DING

***CFD/DDA Coupling for Fluid-structure Interactions
with Applications to Environmental Problems***

Thèse présentée pour l'obtention du grade de Docteur de l'Université de
Technologie de Compiègne (UTC).



Membres du Jury :

S.-S. GUILLOU	Professeur des Universités, ESIX Normandie	Rapporteur
H. NACEUR	Professeur des Universités, INSA Hauts-de-France	Rapporteur
A. Ibrahimbegovic	Professeur des Universités, UTC	Examineur
A. Rassineux	Professeur des Universités, UTC	Examineur
E. Hadzalic,	Assistant Professeur, University of Sarajevo	Examineur
D. Brancherie	Professeur des Universités, UTC	Invitée
A. Ouahsine	Professeur des Universités, UTC	Directeur de thèse

Soutenue le : 23 Mars 2021

Laboratoire Roberval, Unité de Recherche en Mécanique

Spécialité : Mécanique Numérique

CFD/DDA Coupling for Fluid-structure Interactions with Applications to Environmental Problems

Thesis submitted for the degree of
Doctor
at the UT Compiègne-Sorbonne University

by

Dong DING
Roberval Laboratory
UT Compiègne-Sorbonne University
Compiègne, France

23 March 2021

Couplage CFD / DDA pour les
interactions fluide-structure avec des
applications aux problèmes
environnementaux

Thèse présentée pour l'obtention
du grade de Docteur
de UT Compiègne-Sorbonne Université

par

Dong DING
Laboratoire Roberval
UT Compiègne-Sorbonne Université
Compiègne, France

23 Mars 2021

I would like to dedicate this thesis to my loving family.

Acknowledgments

This thesis is sponsored by the China Scholarship Council (CSC) and finished in the Laboratoire Roberval, UT Compiègne-Alliance Sorbonne université under the supervision of Prof. Abdellatif Ouahsine. I would like to sincerely thank Prof. Ouahsine for his encourages and helps both in my work and life. His wisdom, knowledge above all his high standards stimulated me a lot. I benefited a lot from each conversation with him and I also learned how to pursue my study and career. He not only taught me professional knowledge but also a scientific way of thinking and technical skills required in research.

I sincerely thank my thesis committee members, Professor Hakim Naceur and Professor Sylvain S. Guillou for thoroughly reviewing my thesis work, as well as Professors Adnan Ibrahimbegovic, Alain Rassineux, Delphine Brancherie and Dr. Emmina Hadzalic for participating in my thesis jury.

I would like to give my sincere gratitude to some people who give me help during my PhD study. Dr. Peng Du (Northwestern Polytechnical University) is acknowledged for discussing the numerical methods in CFD. Dr. Shengcheng Ji (Beijing Aeronautical Science & Technology Research Institute of COMAC) is acknowledged for sharing his valuable opinions in simulations. Dr. Weixuan Xiao (Université Clermont Auvergne) is thanked for cooperating with me to program 3D-DDA code and sharing some useful C/C++ programming tips in this research. Dr. Ernesto III Paruli (Université de Technology de Compiègne) is thanked for his friendship, encouragement, especially for his useful paper writing skills. Special thanks go to Prof. Guoqing Jing (Beijing Jiaotong University) for his encouragement and guidance in high-speed railway engineering. I would like to thank all the colleagues who work in UTC. They give me lots of help in my french study and life.

Finally, I would like to thank my fiancée Dr. Bei Wu, she not only gave me care and encouragement in life but also gave me many suggestions in my research. I would also thank my parents, who are the strongest support behind me.

Abstract

In numerous applications of environmental fluid mechanics, problems of retroactive interaction between the fluid medium and the discrete solid medium are encountered. This requires the implementation of appropriate numerical coupling techniques and of discrete element methods to take into account the discrete nature of the solid units of the studied medium. This is the case, for example, when studying the problems concerning the stability of rockfill dikes or even the flight of high-speed train ballasts, where the solid medium consists of discrete blocks.

In this thesis, the Discontinuous Deformation Analysis (DDA) method is adopted to study discontinuous and discrete problems. In the first part of the thesis, two-dimensional Discontinuous Deformation Analysis (2-D DDA) is initially used to study the ballast flight caused by dropping snow / ice blocks on high-speed railways and to analyze the dynamic behavior of ballast particles during their collision with a snow / ice block. The numerical results show that the velocity, shape and incident angle of the snow / ice block play an important role in the ballast flight. Specifically, the number and the maximum displacement of ballast particles increase with the speed of the train while the incident angle greatly affects the direction of motion of the ballast particles. The shape of the ice block affects the amount and the extent of the ballast flight. Afterward, the coupling between 2D-DDA and the Computational Fluid Dynamics (CFD) equations (2D-DDA / CFD) is carried out to study the stability of a breakwater under violent wave impacts by using a triple-coupled Fluid-Porous-Solid model. Here, the fluid model is described by the Volume-Averaged Reynolds-Averaged Navier-Stokes equations in which the non-linear Forchheimer equations for the porous medium are added to the inertia terms. The 2D-DDA method is used to analyze the movement and the stability of the caisson and armor units by taking into account the shapes of the armor units, as well as the contact between blocks.

In the second part of the thesis, the 3D version of the DDA method is developed by programming in the C ++ language. Particular attention is given to the detection of contacts between blocks, considered as rigid solids. Thus, the techniques of the Common Plane and of the soft contact method are used to avoid the processes of penetration between solid blocks. The 3D-DDA method is verified and validated first of all by academic test cases. Then, the 3D-DDA model is tested by a fluid-structure interaction procedure which concerns the stability of a hydraulic gravity

dam with pre-existing cracks. The stability and damage of the structure are examined as the water level rises and as a function of the cohesion between the blocks.

Résumé en Français

Les travaux dans cette thèse concernent le développement de méthodes numériques pour des applications de couplage fluide-structure en mécanique des fluides de l'environnement. Il s'agit de mettre en oeuvre des techniques numériques adaptées au couplage d'un modèle d'éléments discrets (DEM) basé sur la méthode d'Analyse des Déformations Discontinues (DDA), avec un modèle avec maillage basée sur la méthode d'Eléments finis (FEM). Ces travaux concernent tout d'abord (i) le développement et la mise en place de la version bidimensionnelle (2D), ensuite (ii) le développement de la version 3D de la méthode DDA.

(i) La première partie a nécessité la programmation en langage C++ de la version 2D du modèle numérique avec la DDA, ceci en adoptant la méthode de 'Pénalité' pour la gestion de contacts entre blocs (solides). La validation et l'application de cette version 2D du modèle numérique ont été réalisées dans deux cas d'étude:

- le premier cas concerne la Dynamique et l'envol de ballasts par le déplacement des trains à Grande Vitesse TGV. L'objectif principal de cette application est de déterminer les facteurs d'influence du vol du ballast et d'analyser le comportement dynamique des particules de ballast lors de leur collision avec un bloc neige / glace, ceci en tenant compte de la forme des blocs de glace et les contacts entre les particules de ballast, ainsi que de la vitesse, de la forme et de l'angle incident des blocs neige / glace. Les résultats de ce premier travail ont fait l'objet d'un article publié dans le journal "Transportation Geotechnics", Elsevier.

- le deuxième cas d'étude, concerne le déplacement d'un caisson induit par des impacts hydrodynamiques. Un modèle basé sur le couplage de trois milieux (fluide-poreux-solide) est développé. Le milieu fluide est décrit par les équations 3D de Navier-Stokes auxquelles sont ajoutées les équations de turbulence à deux équations (K-epsilon). Le milieu poreux est décrit par les équations non linéaires de Forchheimer, lesquelles sont ajoutées aux termes d'inertie du milieu fluide. Enfin, les mouvements du milieu solide sont évalués par la méthode d'analyse de déformation discontinue (DDA), laquelle fait partie des Methods des Elements Discrets (DEM). Les résultats de ce deuxième travail ont fait l'objet d'un article publié dans le dans journal "Ocean Engineering", Elsevier.

(ii) La deuxième partie, a également nécessité la programmation en langage C++,

porte sur le développement et l'implémentation de la version 3D de la méthode DDA. Une attention particulière a été portée sur la détection des contacts entre blocs, considérés comme des solides rigides. Ainsi les techniques du Plan Commun et de pénalité ont été utilisées pour éviter les processus d'interpénétration entre blocs solides.

Les résultats du modèle 3D-DDA ont été vérifiés et validés tout d'abord par des cas tests académiques, sans milieu fluide. Ensuite, le modèle 3D-DDA a été testé par une procédure d'interaction fluide-structure qui concerne la stabilité d'un barrage hydraulique présentant des fissures. Dans cette application, il a été examiné la stabilité et l'endommagement de l'ouvrage, au fur et à mesure que le niveau d'eau augmente et en fonction de la cohésion entre les blocs.

Contents

Preface	I
Acknowledgments	IX
Abstract	XI
Résumé en Français	XV
Contents	i
List of figures	vii
List of tables	xiii
Nomenclature	xv
1 Introduction	1
1.1 Motivation and background	1
1.2 Objective of this thesis	3
1.3 Outline of this thesis	3
2 State of the art of the DDA method	5
2.1 Introduction	5
2.2 Validations	5

2.3	Improvement of DDA	6
2.3.1	Modification of the DDA Method for rotation error	6
2.3.2	High-order displacement function	9
2.3.3	Contact mechanics	10
2.4	Extensions	13
2.4.1	Circular DDA	13
2.4.2	Numerical manifold method	13
2.4.3	DDA-FEM coupling	15
2.4.4	Fluid-DDA coupling	16
2.5	Applications	19
2.6	Development of 3D-DDA	20
2.7	Concluding remarks	20
3	Theory of 2D-DDA and CFD/DDA Coupling approach	23
3.1	Introduction	23
3.2	Governing equations of 2D-DDA	23
3.3	Validations of 2D-DDA	27
3.3.1	Case 1: Frictionless impact - Free fall	27
3.3.2	Case 2: Multi-blocks under seismic loading	28
3.4	Governing equations of fluid	30
3.4.1	RANS equations for turbulent flow	30
3.4.2	Extended Forchheimer equations for porous medium	30
3.4.3	Volume-averaged RANS equation for incompressible fluid- porous medium coupling	31
3.4.4	VOF method	32

3.5	Coupling procedure of Fluid-Solid interaction	33
3.6	Concluding remarks	34
4	Mathematical formulation of the 3D-DDA method	35
4.1	Introduction	35
4.2	Displacement function and global equilibrium equations	35
4.2.1	Displacement function	35
4.2.2	Global equilibrium equations	38
4.3	Governing equations of sub-matrices	39
4.3.1	Sub-matrix of elastic strain	39
4.3.2	Sub-matrix of initial stress	42
4.3.3	Sub-matrix of point loading	42
4.3.4	Sub-matrix of body force	43
4.3.5	Sub-matrix of inertia force	44
4.4	Contact between blocks	47
4.4.1	Common-Plane Method	48
4.4.2	Sub-matrix of normal spring stiffness	53
4.4.3	Sub-matrix of shear spring stiffness	58
4.4.4	Sub-matrix of friction spring stiffness	61
4.4.5	Open-close iterations	63
4.5	Simplex integration for 3D-DDA	66
4.6	SOR iteration method	68
4.7	Procedure for 3D-DDA program	69
4.8	Concluding remarks	71

5	2D-DDA results application to ballast flight in high speed railways	73
5.1	Introduction	73
5.2	Background	73
5.3	Validation: Dynamic behavior of ballast after collision.	75
5.4	Simulation results	77
5.4.1	Velocity of ice block	77
5.4.2	Incident angle of ice block	82
5.4.3	Shape of ice block	85
5.5	Concluding remarks	89
6	Fluid-Solid coupling application to stability of breakwater	91
6.1	Introduction	91
6.2	Background	91
6.3	Numerical model and validation	93
6.3.1	Boundary conditions	93
6.3.2	Mesh and time step convergence	94
6.4	Simulation results	95
6.4.1	Flow patterns around the breakwater	95
6.4.2	Solution behavior with the breakwater seaward slopes	98
6.4.3	Solution behavior with the shape of shoreward armour units	100
6.4.4	Solution behavior with breakwater shoreward slopes	101
6.4.5	Effect of cohesion	106
6.5	Concluding remarks	109
7	Validations and application for 3D-DDA	111

7.1	Introduction	111
7.2	Validations	111
7.2.1	Case 1: Free fall	111
7.2.2	Case 2: Sliding on an inclined plane	113
7.2.3	Case 3: Multi-blocks under gravity loading	115
7.3	Application: gravity dam failure	117
7.3.1	Numerical model	117
7.3.2	Fluid-structure coupling	117
7.3.3	Simulation results	119
7.4	Concluding remarks	123
8	Conclusions and future work	125
8.1	Conclusions	125
8.2	Future work	126
	Bibliography	127
	Appendix A List of publications	145
A.1	Articles	145
A.2	Conferences	146

List of figures

2.1	Rotation error due to linear displacement function [40]	8
2.2	Interaction between two contacting blocks	11
2.3	Rotation and deformation of an ellipse	14
2.4	Illustration of an NDDA model [63].	15
2.5	HYDRO–DDA interface: conversion of fluid pressure into equivalent vertex forces [65]	17
2.6	DDA and fluid interface: (a) finite element mesh and DDA block; (b) fluid pressures around a DDA block and (c) conversion of fluid pressures into equivalent vertex forces [68].	17
2.7	DDA and SPH interaction [70].	18
2.8	Applications of the DDA method	19
2.9	DDA state of the art	21
3.1	The structure of stiffness matrix in the case of three blocks:(a) Loca- tion of three blocks; (b) Structure of stiffness matrix	26
3.2	Interaction between two contacting blocks	27
3.3	Falling block for testing frictionless impact and elastic rebound: (a) Schematic diagram of free fall motion; (b) Comparison between the theoretical value (Equation (3.16)) and DDA results for different con- tact stiffness	28

3.4	Comparison between the experimental results [36] and the numerical results computed by DEM and DDA. The dimension of one block is $48\text{ mm} \times 48\text{ mm} \times 29\text{ mm}$, the mass is 135.5 g , the contact stiffness is 10^7 N/m , the friction angle is $\phi = 34^\circ$, and the peak ground accelerations is 2.15 m/s^2	29
3.5	Comparison between the experimental values of $a_{initiate}$ [36] and DDA results.	30
3.6	Fluid/solid interface: (a) fluid finite element mesh and solid; (b) fluid pressures in the mesh points; (c) conversion of fluid pressures into equivalent vertex forces.	33
4.1	Basic contact types between two 3-D blocks	48
4.2	Definition of distances and sign convention of a point to a plane.	49
4.3	Two blocks contacts and the CP: (a) Non-contact, (b) Potential contact, (c) Real contact	50
4.4	Flowchart of the Common-Plane Method	52
4.5	Contact between vertex and face, P_1 is the penetrate vertex, and $P_2P_3P_4$ is the entrance face.	53
4.6	Contact types and CP position: (a) Vertex-to-vertex; (b) Vertex-to-edge; (c) Edge-to-edge	57
4.7	Contact vertex and the entrance face, and the position of shear spring	59
4.8	Flowchart of open-close iteration	65
4.9	Creating oriented simplexes on a face [100].	66
4.10	Flow chart of 3D-DDA procedure.	70
5.1	Schematic illustration of the mechanism and process of ballast flight caused by dropping ice block.	74
5.2	Comparison between the numerical and experimental responses [137] of the blocks for the DDA method.	76
5.3	Comparison between the numerical and experimental values of N_{33} [137] for the DDA.	76

5.4	Track bed model	77
5.5	Computed ballast flight depending on the initial vertical velocity: (a) $V_y = 0$ m/s (free fall); (b) $V_y = 5$ m/s; (c) $V_y = 10$ m/s	79
5.6	Relationship between (a) number of flying ballast particles and initial vertical velocity of ice block, (b) maximum flying height and initial vertical velocity of ice block	80
5.7	The displacement of (a) ice block and (b) marked ballast for different initial vertical velocity in cross section	80
5.8	Relationship between ballast flight and longitudinal velocity: (a) $V_x = 100$ km/h; (b) $V_x = 200$ km/h; (c) $V_x = 300$ km/h; (d) $V_x = 400$ km/h	83
5.9	The displacement of (a) ice block and (b) marked ballast for different velocities in longitudinal section	84
5.10	Relationship between (a) number of flying ballast particles and initial longitudinal velocity of ice block; (b) maximum flying height and initial longitudinal velocity of ice block	84
5.11	Three ice dropping types and incident angles	85
5.12	Ballast flight at different incident ejection angles: (a) $\alpha = 0^\circ$; (b) $\alpha = 30^\circ$; (c) $\alpha = 60^\circ$; (d) $\alpha = 90^\circ$	86
5.13	The displacement of (a) ice block and (b) marked ballast for different angles in longitudinal section	87
5.14	Relationship between ballast flight and ice block shape: (a) Triangle; (b) Circle; (c) Square	88
5.15	The displacement of (a) ice block and (b) marked ballast of different shapes	89
6.1	Schematic illustration of the computational domain. Wave type: solitary wave; wave height $h_w = 6$ m; water depth $d_w = 10$ m; armour layer thickness $T_a = 2$ m; breakwater caisson height $h_c = 13$ m; caisson position: $x/h_c = 15.96$. The precise location of gauges P1-P5 is $2h_c$, $11h_c$, $13h_c$, $14h_c$ and $15.5h_c$ (m), respectively.	93

6.2 (a) Horizontal velocity and free surface elevation of mesh, and (b) time step convergence at gauge P1 (see Figure 6.1 for the wave parameters and gauges location).	95
6.3 Pattern changes: (a) $t = 19.5 \text{ s}$; (b) $t = 20.5 \text{ s}$; (c) $t = 21.5 \text{ s}$. The impacting wave is a solitary wave with a wave height 6 m and a water height 10 m . The caisson height is 13 m . The thickness of the porous medium (porosity = 0.49) is 2 m . The slope is 1:2.	96
6.4 Pressure distribution along the vertical caisson. The impacting wave is a solitary wave with a wave height 6 m and a water height 10 m . Point A is located at the bottom of the caisson. Points B-D are $\frac{1}{3}h_c$, $\frac{2}{3}h_c$, and h_c away from point A.	97
6.5 Water height evaluation at the vicinity of breakwater (The precise location of gauges P2-P5 see Figure 6.1)	97
6.6 Surface wave deviation with various seaward slopes (1:S). For the wave parameters, see Figure 6.1. The IWH_{max} of the four slopes are: (a) 1.86 m , (b) 3.71 m , (c) 5.57 m and (d) 9.28 m , respectively. . . .	98
6.7 Variation of IWH_{max} (see Figure 6.6) for various seaward slopes. . . .	99
6.8 Turbulent kinetic energy K for various porous layer thickness in $t=24.0 \text{ s}$. (see Figure 6.1 for the wave parameters).	99
6.9 Shapes of armour units used in the simulation.	100
6.10 Simulated movement for various shapes of armour units: (a) Cube, (b) Accropod, (c) Tetrapod. The breakwater was subjected to solitary wave impacts whose input external force is calculated by Equation (3.27). (See Figure 6.1 for the wave parameters).	102
6.11 Variation of standard deviations for three shapes of armour units. . . .	103
6.12 Standard deviations for three slopes	104
6.13 Slope of breakwater: (a) slope= $\sqrt{3}$:1; (b) slope=1:1; (c) slope=1:2. The shape of armour unit is cube. The breakwater was subjected to solitary wave impacts whose input external force is calculated by Equation (3.27). (See Figure 6.1 for the wave parameters).	105

6.14	Standard deviations for three slopes	106
6.15	Standard deviations for three slopes	107
6.16	Comparison of the motion of cubic units at final position: (a) cohesion=0 Pa, tensile strength $\sigma_t = 0.7$ MPa; (b) cohesion= 2 MPa, tensile strength $\sigma_t = 0.7$ MPa; (c) Comparison of the effect of cohesion. The breakwater was subjected to solitary wave impacts whose external force is calculated by Equation (3.27) (See Figure 6.1 for the wave parameters).	108
6.17	Displacement of cubic armour units 2 and 5 with and without cohesion	109
7.1	Schematic representation of a block in free fall. Falling height $h = 10.60$ m, $g = 9.81$ m/s ² , initial velocity $V_0 = 0$ m/s.	112
7.2	Comparison of analytical and numerical velocities. Falling height $h = 10.60$ m, $g = 9.81$ m/s ² , initial velocity $V_0 = 0$ m/s.	112
7.3	(a) Initial and (b) final positions of sliding model. $\alpha = 30^\circ$, $\phi=0$	113
7.4	Time step convergence at the sliding block. Slope angle $\alpha = 30^\circ$, friction angle $\phi = 0^\circ$, time interval $\Delta t = 0.1$ s, 0.01s and 0.001s, respectively. Analytical results calculated by the Equation (7.1).	114
7.5	Variation of the (a) velocity and (b) displacement for different interface friction angles. Slope angle $\alpha = 30^\circ$, friction angle $\phi= 0^\circ$, 10° and 20° , respectively, time interval $\Delta t = 0.01$ s. Analytical results calculated by the Equation (7.1).	114
7.6	Variation of the (a) velocity and (b) displacement for different slope incline angles. Slope angle $\alpha = 15^\circ$, 30° and 45° , respectively, friction angle $\phi= 0^\circ$, time interval $\Delta t = 0.01$ s. Analytical results calculated by the Equation (7.1)	115
7.7	Multi-blocks model under gravity loading. $\Delta t = 0.01$ s, time steps = 60.	116
7.8	Comparison of 2D and 3D velocity at marked point	116
7.9	Comparison of 2D and 3D displacement at marked point	117
7.10	Numerical model of gravity dam with pre-existing cracks	118

7.11 Fluid-solid interface.	119
7.12 Fluid force acting on solid vertex calculated by Equation (7.4).	120
7.13 Failure behavior of the gravity dam; water height above the cracks $h = 4.0\ m$	121
7.14 Variation of displacement of block No. 1 for three water levels.	122
7.15 Variation of displacement of block No. 2 for three water levels.	122
7.16 Variation of displacement of block No. 1 for different cohesion, water height above the cracks $h = 4.0\ m$	123

List of tables

2.1 DDA validation by comparing with mathematical analysis	7
2.2 DDA validation by comparing with DEM and tests	8
2.3 Summary of contact algorithm	11
4.1 Contact types detected by Common-Plane Method	51
4.2 Criteria for contact mode change	64
5.1 The material parameters of ice and ballast	77
6.1 Material parameters used for simulations	100

Nomenclature

List of abbreviations

CFD	Computational Fluid Dynamics
CP	Common-Plane
CPM	Common-Plane Method
CRTL	Small positive tolerance defined in CPM
DDA	Discontinuous Deformation Analysis
DEM	Distinct Element Method
DIANE	Discontinuous, Inhomogeneous, Anisotropic and Non-elastic
FDM	Finite Difference Method
FEM	Finite Element Method
FSI	Fluid Structure Interaction
FVM	Finite Volume Method
IBM	Immersed Boundary Method
ICB	Ice Block
IWH	Impacting Wave Height
NMM	Numerical Manifold Method
OCS	Overhead Contact System
PIMPLE	Merged PISO-SIMPLE
PISO	Pressure Implicit with Split Operator
RANS	Reynolds-Averaged Navier Stokes
SIMPLE	Semi-Implicit Method for Pressure Linked Equations
SOR	Successive Over-Relaxation
SPH	Smoothed Particle Hydrodynamics
TKE	Turbulence Kinetic Energy
TGV	Trains à Grande Vitesse
UDEC	Universal Distinct Element Code
VARANS	Volume-Averaged Reynolds-Averaged Navier-Stokes
VOF	Volume-of-Fluid

List of symbols

d_n	Displacement at normal direction
d_τ	Displacement at shear direction
d_{ri}	Displacement variable of block i
\mathbf{f}_b	Body forces applied on a block
g	Gravity acceleration
h	Water height above the cracks
h_w	Water depth
k_s, k_τ	Normal and shear contact stiffness
\mathbf{p}, \mathbf{q}	Two arbitrary orthogonal axes are selected in the CP
(x_0, y_0, z_0)	Coordinate of Centroid
$\left(u_0, v_0, \gamma_0, \varepsilon_{xx}, \varepsilon_{yy}, \varepsilon_{xy} \right)$	Translations, rotations, normal and shear strains of 2D block
(u, v, w)	Displacement of a block
r_g	Refinement radio
C_f	Cohesion
C_A	Added mass term
D_{50}	Mean diameter of porous material
\mathbf{D}	Displacement sub-matrices
$\ddot{\mathbf{D}}, \dot{\mathbf{D}}$	Acceleration and velocity matrices
E	Young's modulus
\mathbf{K}	Stiffness sub-matrices
K_C	Keulegan-Carpenter number
\mathbf{E}	Elastic matrix of deformation plane
\mathbf{F}	Force sub-matrices
(F_x, F_y, F_z)	Point loading in x,y,z direction
F_f	Friction force
$\check{\mathbf{L}}, \hat{\mathbf{R}}$	Strictly lower and upper triangular components of matrix \mathbf{K}
M	Mass per unit volume
M_{ice}	Mass of ice block
N_{33}	Number of ballast particles thrown higher 330 mm
P	Penalty spring stiffness
Re	Reynolds number
\mathbf{U}	Fluid velocity
$\langle \mathbf{U} \rangle$	Volume-averaged velocity
V	Total volume
V_f	Volume of fluid

V_{fall}	Velocity during the falling process
V_{Amax}	Vertex on particle A nearest to the CP
V_{Bmin}	Vertex on particle B nearest to the CP
T_o	Period of the oscillation

Greek symbols

α	Fluid volume fraction
β_1, β_2	Coefficients in Newmark method
χ	Diagonal component of submatrix \mathbf{K}
δ	Penetration distance between blocks
μ_{eff}	Effective viscosity
μ_t	Eddy viscosity
ν	Poisson's ratio of block material
ρ	Fluid density
λ_k	Contact force at k-th iteration
σ	Surface tension
σ_0	Initial stress
$(\sigma_x, \sigma_y, \sigma_z, \tau_{yz}, \tau_{zx}, \tau_{xy})$	Stress of block
ω	Relaxation factor for SOR convergence
Ω_i	Entire volume of block i
φ	Friction angle
$(\varepsilon_x, \varepsilon_y, \varepsilon_z, \gamma_{yz}, \gamma_{zx}, \gamma_{xy})$	Strain of block
ϕ	Friction angle
Π	Total potential energy
$\Pi_{elastic}$	Elastic strain energy
$\Pi_{initialstress}$	Initial stress potential energy
$\Pi_{pointload}$	Point loading energy
$\Pi_{bodyforce}$	Body force potential energy
$\Pi_{inertia}$	Inertial energy
Π_{fluid}	Potential energy contributed due to fluid hydrodynamics
$\Pi_{contact}$	Potential energy contributed due to contacts between blocks
Δt	Time step

Introduction

1.1 Motivation and background

During the environmental engineering practice, problems of the discontinuous media are often encountered. For example, the ballast particles in the track and the armour units in the breakwater, etc. The blocks are largely discontinuous, inhomogeneous, anisotropic, and non-elastic (DIANE) material [1]. Correctly establishing the corresponding numerical models based on the real conditions is quite challenging and significant to provide suggestions for the discontinuous environmental problems.

Traditionally, several modified continuum approaches are used to investigate the discontinuous and discrete medium, which can be divided into two types [2]:

- Continuum with joint interface approach;

The continuum with the joint interface method introduces the discontinuity interface in the form of "joint element" [3] or "discontinuity of displacement" [4] to model the discontinuity.

- Equivalent continuum approach;

The equivalent continuum method modifies the constitutive equation of the rock mass to include the mechanical effects of the joints.

These two continuum-based methods have been implemented in Finite Element (FE), Finite Difference (FD) and Boundary Element (BE) methods [5, 6, 7]. They have also been successfully used in applications where no large deformation of the rock mass occurs.

The discrete element method based on discontinuous medium mechanics is used to simulate the motion and collision characteristics of a bulk system. It gives a better solution to investigate the large deformation problems. The most commonly used

discrete element approaches are Distinct Element Method (DEM) [8] and Discontinuous Deformation Analysis (DDA) . The Discontinuous Deformation Analysis (DDA) method was developed by Gen-hua Shi in the late 1980s [9]. Since its publication, DDA has been verified and applied in numerous studies worldwide and is now considered as a powerful and robust method to address both static and dynamic engineering problems [10]. DDA is somewhat similar to the Finite Element Method (FEM) for solving stress-displacement problems, but accounts for the interaction of independent particles (blocks) along discontinuities in fractured and jointed rock masses. DDA is typically formulated as a work-energy method, and can be derived using the principle of minimum potential energy [9]. Once the equations of motion are discretized, a step-wise linear time marching scheme in the Newmark family is used for the solution of the equations of motion. The relation between adjacent blocks is governed by equations of contact interpenetration and accounts for friction. DDA adopts a stepwise approach to solve the large displacements that accompany discontinuous movements between blocks. Since the method accounts for the inertial forces of the blocks' mass, it can be used to solve the full dynamic problem of block motion. The formulation of DDA overcomes the problem of energy dissipation due to algorithmic damping especially when the penalty method is used to handle the contact mechanics between blocks [11, 12] comparing with FEM method. Although DDA and DEM are similar in the sense that they both simulate the behavior of interacting discrete bodies, they are quite different theoretically. While DDA is a displacement method, DEM is a force method. The advantage of DDA over other rigid body discrete element approaches is DDA gives real dynamic solution with correct energy consumption and utilizes simple or even higher-order deformability of complex shapes [13].

DDA has been widely-used for discontinuous medium simulations. However, the original DDA method still has some limitations which limited its applications. For example, it is rarely used to study the problem of a large number of particles; furthermore, it cannot incorporate water pressures in the joints, as well as there is a gap between two dimensions in reality and no open-source code released for 3D-DDA.

1.2 Objective of this thesis

This thesis aims to investigate the discontinuous and discrete environmental problems based on the DDA method. The 2D-DDA method will be introduced and the CFD/DDA coupling approaches will be proposed. Furthermore, the 3D-DDA method will be developed and validated. The most important aspects include:

- The literature review of the DDA method will be presented. The validations, modifications, extensions and applications will be introduced in detail.
- The 2D-DDA equations with penalty method will be presented; A coupling strategy that transmit the pressure of the fluid mesh nodes to the solid polygon vertices will be proposed to achieve fluid-solid coupling.
- The 3D-DDA equations will be developed and programmed. The common-plane method will be used to detect contact; the soft contact method and open-close iteration method will be used to avoid penetration; the Successive Over-Relaxation (SOR) method will be used to solve linear system equations.
- A numerical model based on the 2D-DDA method will be proposed to study the ballast flight caused by dropping snow / ice blocks in high-speed railways. The dynamic behavior of ballast particles during their collision with a snow / ice block will be investigated.
- A coupled Fluid-Porous-Solid model will be used to study the stability of breakwater. The fluid model will be described by the Volume-Averaged RANS equations. The solid model, which is based on the DDA method, will be used to compute the movement of the caisson and armour units.
- The 3D-DDA code will be verified by comparing with the analytical results and 2D-DDA results. Then a fluid and solid coupling procedure will be proposed to study the failure of gravity dam due to the rising water level. The effect of the increasing water level and cohesion between structures will be studied.

1.3 Outline of this thesis

This thesis is organized as follows:

- **Chapter 2** presents the start-of-the-art literature review of the Discontinuous Deformation Analysis method;

- **Chapter 3** introduces the brief theory of the 2D-DDA method and the 2D-CFD/DDA coupling approach;
- **Chapter 4** is devoted to developing the 3D-DDA program, including the common plane method, the open-close iteration method and SOR method.
- **Chapter 5** simulates ballast flight caused by dropping snow / ice blocks in high-speed railways. The dynamic behavior of ballast particles during their collision with a snow / ice block is investigated.
- **Chapter 6** carries out the coupled Fluid-Porous-Solid model to study the stability of breakwater. The flow patterns around the breakwater and the movement of the caisson and armour units are simulated.
- **Chapter 7** verifies the 3D-DDA by comparing with the analytical results and proposes a 3D fluid and solid coupling procedure to study the gravity dam failure.
- **Chapter 8** concludes this thesis and gives suggestions for future work.

State of the art of the DDA method

2.1 Introduction

In this chapter, the state-of-the-art review of the DDA method is presented. The following aspects are emphasized:

- The validations of the DDA method are introduced. The DDA method has been verified by comparing with the mathematical analysis, other computational techniques and experimental data;
- The extensions of the DDA method are presented. The DDA method has been coupled with many numerical methods, for example, FEM, SPH and NMM ect.
- The applications of the DDA method are summarized and the development of 3D-DDA method is briefly introduced.

2.2 Validations

The validation works of DDA can be classified into three categories [14]: (1) Comparison with mathematical analysis; (2) Comparison with other computational techniques; and (3) Comparison with experimental data. For the first type, the accuracy of DDA was verified in different aspects, for example, sliding, rotation, tensile strength, impact, and time integration, as shown in Table 2.1. DDA simulations show high acceptable accuracy in most of the common engineering phenomena; however, large body rotation always accumulates the first-order approximation error and causes the block volume expansions; therefore, several modifications have been proposed and will be described in Section 2.3.1. For the second type, other discrete numerical technologies were studied to valid the DDA method, as shown in Table 2.2. Dong et al. [15] used a tunnel model to compare the displacement results between the DDA and FEM predictions. Although the FEM model seems to predict a larger horizontal displacement component, the displacement patterns

caused by the slope excavation predicted by the FEM and DDA models are similar. Furthermore, MacLaughlin et al. [16] compared DDA with another widely used DEM code: Universal Distinct Element Code (UDEC). The instability and deep failure of the rock model which has five dip angles combined with three rock mass are investigated by DEM and UDEC. 73% of simulations of the two methods are essentially identical. Khan [2] examined the time integration of those two methods in parallel. UDEC uses an explicit scheme while DDA uses an implicit scheme. The explicit scheme has low computational cost while the implicit scheme enhanced stability [17, 18].

Validation with respect to experiments are summarized in Table 2.2, where the sliding, shaking and impacting process were investigated. McBride et al. [19] established a joint rock slope model, patterned after Cundall et al. [20]. The DDA simulation can simulate the failure modes observed experimentally. Ishikawa et al. [21] and Ding et al. [22] studied the dynamic behavior of railroad ballast. Results from the DDA simulations qualitatively agree with experimental results from triaxial tests and air cannon impact tests [14].

2.3 Improvement of DDA

Many modifications and improvements to the DDA method have been proposed to overcome some of its limitations and make it more efficient, suitable and practical on engineering computations.

2.3.1 Modification of the DDA Method for rotation error

Ohnishi et al. [26] and MacLaughlin et al. [40] found large rigid body rotation causes block expansion. According to the first-order approximation of DDA, the displacement of block due to rigid translation and rotation is written as:

$$\begin{aligned} u &= u_0 - (y - y_0)r_0 \\ v &= v_0 + (x - x_0)r_0 \end{aligned} \quad (2.1)$$

while the real displacement should expressed as:

$$\begin{aligned} u &= u_0 + (x - x_0)(\cos\theta - 1) - (y - y_0)\sin\theta \\ v &= v_0 + (x - x_0)\sin\theta + (y - y_0)(\cos\theta - 1) \end{aligned} \quad (2.2)$$

Table 2.1: DDA validation by comparing with mathematical analysis

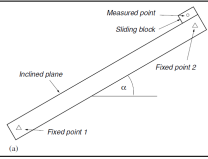
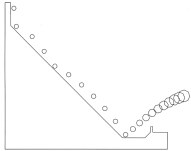
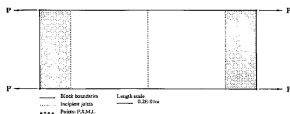
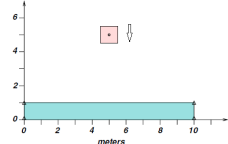
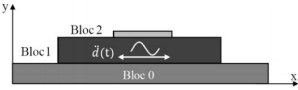
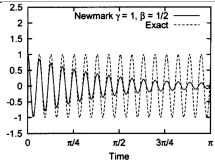
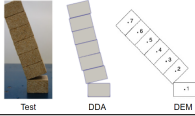
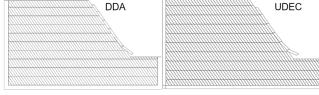
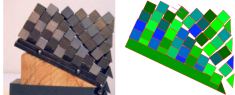
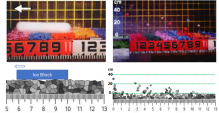
Content	Illustration	Results	Ref
Sliding		<ul style="list-style-type: none"> • DDA meets the analytical equation, the relative error is less than 0.1%. • Lower friction angle values inducing less initial perturbation. 	[23] [24] [25]
Rotation		<ul style="list-style-type: none"> • Large body rotation accumulates error and causes block expansion; • Using a second-order equation, when the rotation is less than 0.2 radians, the error is negligible. 	[26] [27] [28]
Tensile strength		<ul style="list-style-type: none"> • Jointed rock specimen subjected to horizontal uniaxial tension; • Load factor 100 N/s has an error of about 0.01%. 	[29]
Impact		<ul style="list-style-type: none"> • DDA shows a qualitatively good agreement using high contact stiffness. • Smaller contact stiffness, larger penetration, inelastic. 	[30] [31] [32] [22]
Multiblocks		<ul style="list-style-type: none"> • Accumulated displacement is proportional to the input amplitude; • The relative error is between 1% and 2%. 	[33] [34]
Time integration		<ul style="list-style-type: none"> • Newmark approach used to solve the kinematic system; • Smaller time step size has higher accuracy than higher time step size. 	[12] [35]

Table 2.2: DDA validation by comparing with DEM and tests

Content	Illustration	Results	Ref
DEM Multi-blocks		DDA simulations show similar responses to test observations; Here, DDA has better accuracy than DEM.	[36]
UDEC: Slopes		DDA and UDEC produce a similar result; Explicit DEM has faster computational speed than implicit DDA.	[2] [37]
Test: Sliding		Experiment and DDA simulation failure patterns correspond well.	[38] [24]
Test: Shaking		Slope failure verified by DDA; DDA can be applied to seismic issues.	[39]
Test: Impact		The number of flying blocks agrees with the test; A large number of blocks also have good accuracy	[22]

where u_0 and v_0 are the rigid body translations, and r_0 is the rotation angle of the rigid body around its gravity center (x_0, y_0) . When the body rotation is very small, Equation (2.2) can be approximated as Equation (2.1). However, the rigid body area usually gets expansive if it moves with large rotation, the error due to linear displacement function is shown in Figure 2.1.

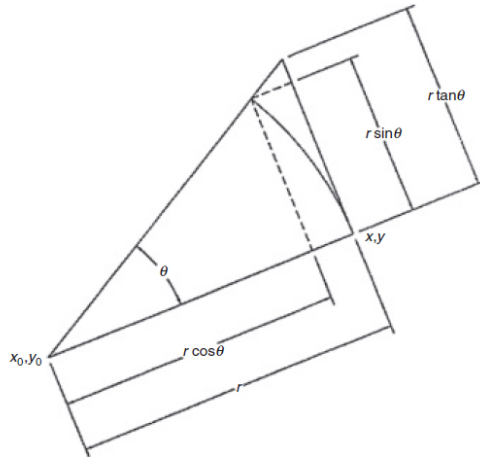


Figure 2.1: Rotation error due to linear displacement function [40]

In order to solve the problem of block expansion, three approaches have been proposed:

- (1) Use an exact displacement function with nonlinear terms [40, 41];

In the first approach, the trigonometric functions in Equation (2.2) can be expressed using Taylor's series polynomial approximations, as shown in Equation (2.3). This is a more accurate displacement function, while the error still occurs when the high-order terms are omitted. When the block rotation angle is not greater than 0.4 radians, the error is small, but the error will increase with the accumulation of time steps.

$$\begin{aligned} \sin(r_0) &= \frac{r_0}{1!} - \frac{r_0^3}{3!} + \frac{r_0^5}{5!} - \dots \\ \cos(r_0) &= 1 - \frac{r_0^2}{2!} + \frac{r_0^4}{4!} - \dots \end{aligned} \quad (2.3)$$

- (2) Use linear displacement function and post-correction [27, 42].

In the second approach, the simplified linear displacement function Equation (2.1) is adopted. Further to modify the error, the block vertices' positions are recalculated using the exact displacement function after each step of the calculation. It should be noted that although this method can prevent the increase of block volume, it did not consider the cumulative effect of higher-order terms.

- (3) Increase the order of the polynomial [43, 44].

This approach will be described in detail in the next section 2.3.2.

2.3.2 High-order displacement function

In the original 2D-DDA method, a first-order polynomial displacement function approximation was assumed. However, this approximation not only has rotation error but also limits the application of DDA in areas with large stress concentrations. Therefore, some attempts were made to develop the N-order displacement formulation.

Koo et al. [28, 43] firstly developed the second and third-order displacement functions by incorporating the complete high-order term. However, these extents still cannot selectively achieve higher accuracy or more efficiency in calculation. Then, Hsiung et al. [45] developed a more general formulation of the DDA that be able to accept any order of polynomial displacement function by reducing the total degree of freedom for different problems. Furthermore, Wang et al. [46] addressed the difficulties associated with the implementation of high-order in DDA and generalized

the displacement function in a series form:

$$\begin{cases} u = \sum_{j=1}^m d_{2j-1} f_j(x, y) \\ v = \sum_{j=1}^m d_{2j} f_j(x, y) \end{cases} \quad (2.4)$$

where the functions $f_j(x, y)$ are defined as $(j - 1)^{th}$ order polynomial, and d_{2j-1} , d_{2j} are variables representing the displacements and deformations of the block. Assuming $q = 2m$, Equation (2.4) can be written in matrix form:

$$\begin{pmatrix} u \\ v \end{pmatrix} = \mathbf{T}_i \mathbf{d}_i = \begin{pmatrix} f_1 & 0 & f_2 & 0 & \cdots & f_m & 0 \\ 0 & f_1 & 0 & f_2 & 0 & \cdots & f_m \end{pmatrix} \begin{pmatrix} d_1 \\ d_2 \\ d_3 \\ \vdots \\ d_{q-1} \\ d_q \end{pmatrix}. \quad (2.5)$$

where i represents the i -th block, (u, v) are the displacements of point (x, y) , \mathbf{T}_i is a $2 \times q$ matrix and \mathbf{d}_i is a $q \times 1$ matrix.

2.3.3 Contact mechanics

Traditionally, the penalty method and the Lagrange multiplier method are two commonly used approaches to avoid interpenetration between blocks. The Augmented Lagrangian method is introduced and the soft contact approach developed from the penalty method is introduced in this section. The summary of these contact mechanics methods is shown in Table. 2.3.

The penalty method was originally used by Shi [9] in the DDA method to enforce contact constraints at block interfaces. Considering two blocks i and j , where point P_1 of block i penetrates a depth, δ , into edge P_2P_3 of block j . Using the penalty method is equivalent to placing a spring between point P_1 and the edge P_2P_3 , as shown in Figure 2.2.

The formulation for the strain energy of contact spring between block i and j is:

$$\Pi_{contact} = \frac{1}{2} P \delta^2 \quad (2.6)$$

where p is a penalty number which is also the spring stiffness

This method has proved to be effective in many areas of numerical modeling [47,

Table 2.3: Summary of contact algorithm

Approach	Formula	Limitations
Penalty method	$\Pi_{contact} = \frac{1}{2}P\delta^2$	<ul style="list-style-type: none"> • Penalty number P should be very large • Contact constraints are only approximately satisfied • Governing equation number is increased
Lagrange multiplier method	$\Pi_{contact} = \lambda\delta$	<ul style="list-style-type: none"> • Very large extra computational effort
Augmented lagrangian method	$\Pi_{contact} = \lambda_k^*\delta + \frac{1}{2}P\delta^2$ $\lambda_{k+1}^* = \lambda_k^* + P\delta$	<ul style="list-style-type: none"> • Iterations of Lagrange multiplier λ_k^* increase calculation time
Soft contact approach	$\Pi_{contact} = \frac{1}{2}(k_n d_n^2 + k_s d_s^2)$	<ul style="list-style-type: none"> • Contact stiffness may be difficult to obtain.

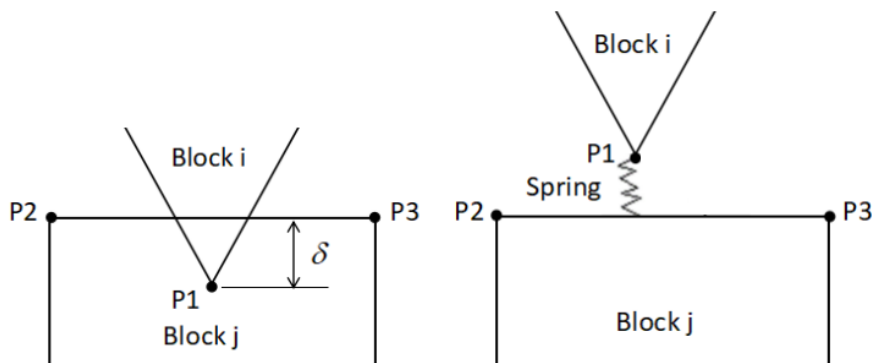


Figure 2.2: Interaction between two contacting blocks

48]. However, the main limitation with the penalty approach is the choice of the penalty number, since the solution significantly depends on this number. Furthermore, the contact constraints are only approximately satisfied.

The Lagrange multiplier method is another one of the most commonly used approaches to solve block contact problems [49, 50, 51]. This method assumes the penetration δ is caused by an unknown contact force λ , therefore the strain resulting from the contact force is defined as:

$$\Pi_{contact} = \lambda\delta \quad (2.7)$$

This method satisfies the contact conditions exactly, whereas the number of governing equations is increased so that extra computational effort is required. The Lagrange approach is rarely used in DDA due to its large consuming computation time.

Combing the above two approaches, Amadei et al. [51] and Lin et al. [52, 53] proposed the augmented Lagrangian formulation to model the contact between blocks in the DDA method. The augmented Lagrangian method contains both the penalty method and the classical Lagrange multiplier method. In this method, a Lagrange multiplier λ^* , which represents the contact force, is iteratively calculated until the penetration δ below a specified tolerance. The strain energy of contact spring and force is expressed in the following form:

$$\Pi_{contact} = \lambda_k^*\delta + \frac{1}{2}P\delta^2 \quad (2.8)$$

where the term $\lambda_k^*\delta$ accounts for the work done by the contact forces between the blocks and the term $\frac{1}{2}P\delta^2$ represents the elastic potential energy associated with the contact between the blocks. An iterative process is used to calculate the first order updated of the Lagrange multiplier, λ_k^* , as follows:

$$\lambda_{k+1}^* = \lambda_k^* + P\delta \quad (2.9)$$

Furthermore, the mechanical model of contacts in other DEM codes also can be learned and used in the DDA method. In the original DDA method, the interpenetration between blocks is considered non-physical, and with the help of penalty functions, algorithms are used to prevent any intersection of the two contacting bodies [54]. This is a hard contact approach while other DEM codes most use the soft contact approach in which the interpenetration causes contact forces according to the actual contact stiffness, and the arising contact forces are calculated from

the depth of the interpenetration [55, 56]. The strain energy due to the normal and tangential contact spring is presented as:

$$\Pi_{contact} = \frac{1}{2}(k_n d_n^2 + k_s d_s^2) \quad (2.10)$$

where k_n and k_s are the actual normal and tangential contact stiffness, d_n and d_s are normal and tangential penetration distances

The soft contact approach is a more realistic method but the appropriate properties are hard to obtain; the penalty method is simple and easy to add to the program but the contact constraints meet contact constraints only approximate, and the penalty spring stiffness has a significant influence on accuracy and convergence. Khan et al. [2] implements the soft contact approach to DDA code that shows good agreement with analytical results and less residual error.

2.4 Extensions

2.4.1 Circular DDA

An advantage of the original DDA is that the irregular blocks can be investigated; however, it may have contact problems when studying the circular blocks which are modeled as polygons with many edges. In order to extend the application of the DDA method, many researchers have developed the circular DDA method based on the original equations. Ohnishi et al. [57] first implemented the mathematical derivation to the DDA with the elliptical elements. Then, they improved the contact mechanism to study the time-dependent deformation of elliptic disc elements, as shown in Figure 2.3. This method was also applied in soil mechanics and geotechnical engineering fields [58, 59].

2.4.2 Numerical manifold method

The numerical manifold method (NMM) was developed based upon the DDA method and mathematical manifold method [60], which can compute the movement and deformation of continuous and discontinuous blocks by the finite cover and displacement cover. The fracture of blocks also can be modeled by dividing a cover into two or more disconnected domains.

For finite covers, the cover displacement functions can be defined by the weight

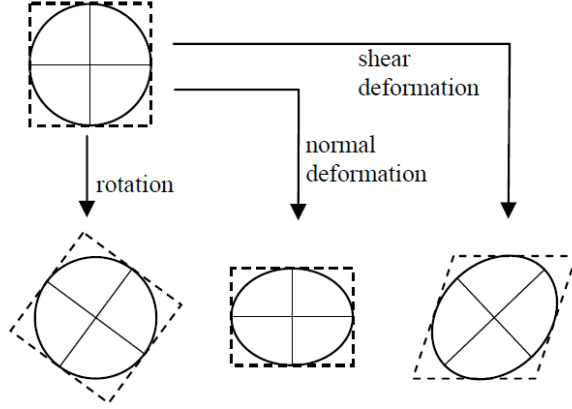


Figure 2.3: Rotation and deformation of an ellipse

functions:

$$\begin{Bmatrix} u(x, y) \\ v(x, y) \end{Bmatrix} = \begin{pmatrix} w_i(x, y) & 0 \\ 0 & w_i(x, y) \end{pmatrix} \begin{pmatrix} u_i \\ v_i \end{pmatrix} = \sum_{i=1}^n \mathbf{T}_i(x, y) \mathbf{D}_i \quad (2.11)$$

Here we assume the weighting functions satisfies:

$$w_i(x, y) \geq 0, \quad (x, y) \in U_i; \quad w_i(x, y) = 0, \quad (x, y) \notin U_i \quad (2.12)$$

where U_i represent the finite meshes.

Taking a triangle element as an example, for element e and $(x, y) \in e$, the Equation (2.11) can be written as:

$$\begin{Bmatrix} u(x, y) \\ v(x, y) \end{Bmatrix} = \sum_{r=1}^3 \mathbf{T}_e(r) \mathbf{D}_e(r) \quad (2.13)$$

where

$$\mathbf{T}_e(r) = \begin{pmatrix} f_{1r} + f_{2r}x + f_{3r}y & 0 \\ 0 & f_{1r} + f_{2r}x + f_{3r}y \end{pmatrix} \quad (2.14)$$

For the displacement function, the first-order approximation follows the minimum potential law which is similar to the DDA method. Besides, DDA and NMM the kinematics constraints and contact detection method. It should be mentioned that when a discrete block coincides with the manifold element, the NMM is DDA, which is one of the special cases in NMM.

2.4.3 DDA-FEM coupling

Coupling DDA with the FEM means adding the FEM meshes inside the DDA blocks to get more accurate descriptions of the block's deformation [61]. The system equilibrium of FEM and DDA is obtained by the principle of total potential energy minimization.

The nodal-based DDA (NDDA) method, which couples the FEM and the DDA, in which the DDA kinematics are incorporated with the finite-element mesh, was first developed by Shyu [62]. Take the triangular elements as an example (see Figure 2.4), each element has three nodes (i, j, m) and six displacement variables ($u_i, v_i, u_j, v_j, u_m, v_m$). The displacement (u, v) of any point (x, y) within a triangular element can be written as:

$$\begin{Bmatrix} u \\ v \end{Bmatrix} = \begin{bmatrix} N_i & 0 & N_j & 0 & N_m & 0 \\ 0 & N_i & 0 & N_j & 0 & N_m \end{bmatrix} \begin{Bmatrix} u_i \\ v_i \\ u_j \\ v_j \\ u_m \\ v_m \end{Bmatrix} \quad (2.15)$$

where N_i, N_j and N_m represent the shape functions of the triangular element.

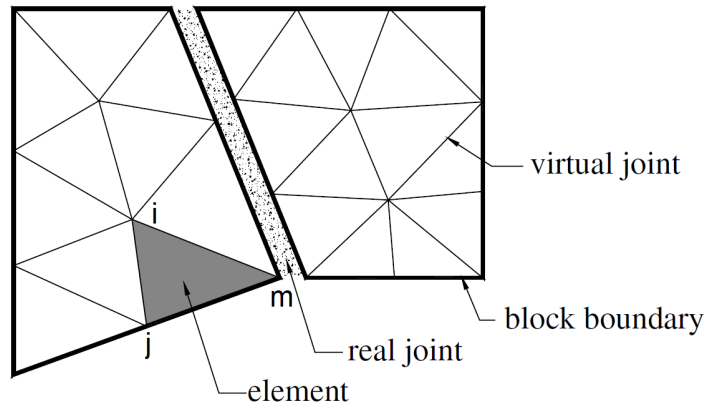


Figure 2.4: Illustration of an NDDA model [63].

Then, Bao et al. [63] extended the NDDA program by employing the Mohr-Coulomb failure criterion to provide a good representation of residual strength conditions to analyze the fracture. Indeed, by discretizing the block into finite elements, the accuracy of the DDA method and its ability to resolve stress changes can be improved. Furthermore, the sub-block analysis method [64] can also be used to achieve the same determination, where each block is divided into smaller sub-blocks, which

also can study the fracture by implementing the Mohr-Coulomb failure criterion.

2.4.4 Fluid-DDA coupling

In the original DDA method, no hydrodynamic forces are considered, however, the fluid flow pressure in the joint usually has a profound effect on the deformation of the rock mass, especially on the stability of the rock block.

Rouainia et al. [65] developed a HYDRO-DDA model to evaluate the responses of fluid flow in deforming discontinuous media. The fluid has been described by the means of Darcy's law using a FEM mesh, responds to pressure on the solid boundary and to porosity changes in the discontinuity patterns. However, this model can only be used in steady state fluid flow and linear problems. Indeed, some different fluid flows coupled with DDA were proposed [66, 67]. Kaidi et al. [68] presented a finite element model for solving the complete two dimensions vertical (2DV) Navier–Stokes equations with the free-surface flow. This model is proposed for coupling with the DDA method to analyze non-linear wave–structure effects. Mikola and Sitar [69] presented a fluid-structure coupling between Smoothed Particles Hydrodynamics (SPH) and DDA for modeling rock-fluid interactions. The Navier-Stokes equation is simulated using the SPH method and the motions of the blocks are tracked in the DDA formulation.

In order to couple the fluid and solid, some transmission strategies were proposed. The first approach operates by establishing an initial fluid pressure distribution in the fluid element nodes of the boundary conditions and passing this information to the vertex of DDA [65], as shown in Figure 2.5.

The normal forces acting on the vertices associated with an edge (from vertex 1 to vertex 2) of a block are written as:

$$\begin{aligned} F_1 &= \frac{L}{2} \left(P_{1m} + \frac{1}{3}(P_{2m} - P_{1m}) \right) \\ F_2 &= \frac{L}{2} \left(P_{1m} + \frac{2}{3}(P_{2m} - P_{1m}) \right) \end{aligned} \quad (2.16)$$

where L is the length of the edge, and P_{1m} and P_{2m} are the pressure at the centroid of the corresponding finite element in the fluid mesh where the two block vertex are located.

Based on this approach, a more accurate solution was developed [68]. The procedure is first calculated the fluid pressure by the fluid flow model, and then the distributed fluid pressures are converted to the corner nodal points hydrodynamic forces (f_i, f_j) of the finite element mesh, as shown in Equation (2.17). This method

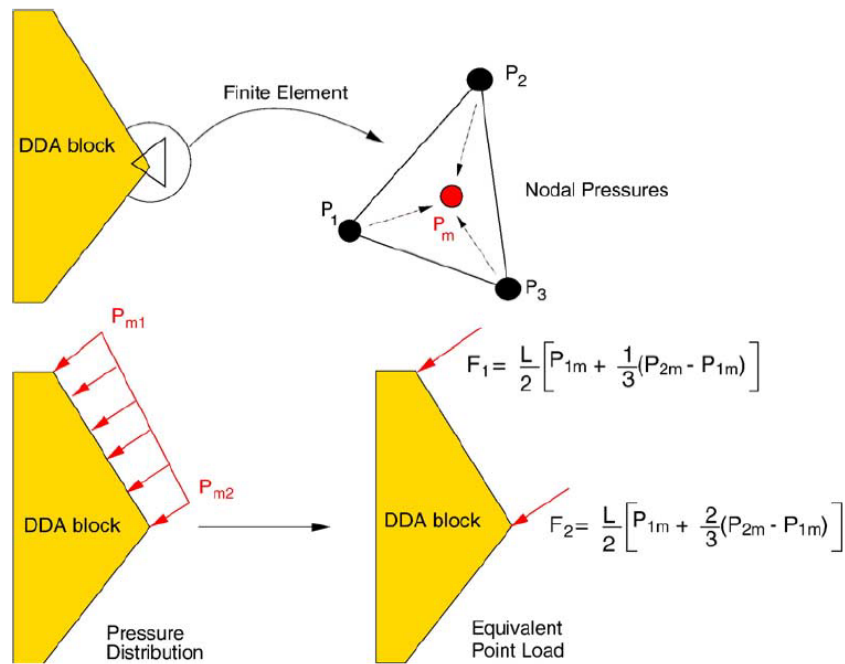


Figure 2.5: HYDRO-DDA interface: conversion of fluid pressure into equivalent vertex forces [65]

fully considers the distance between the nodes and the two vertices of an edge.

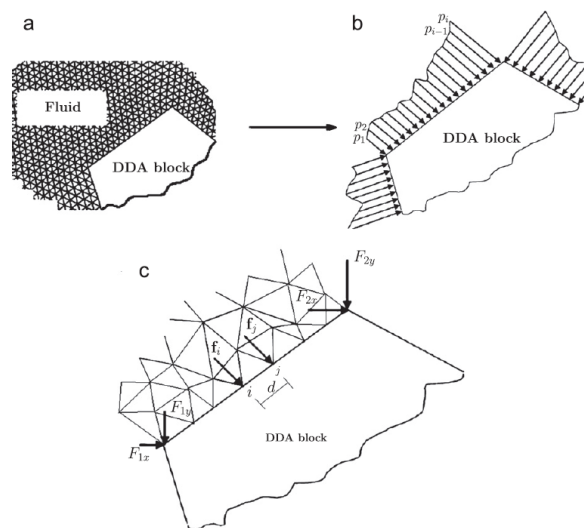


Figure 2.6: DDA and fluid interface: (a) finite element mesh and DDA block; (b) fluid pressures around a DDA block and (c) conversion of fluid pressures into equivalent vertex forces [68].

$$f_i = p_i \frac{d}{2}; f_j = p_j \frac{d}{2} \quad (2.17)$$

where p_i and p_j are the fluid pressure at nodes i and j , and d is the distance of the finite element edge from node i to node j . Finally, the global forces (F_1, F_2) acting on the DDA block can be written as:

$$\begin{aligned} F_{1x} &= \sum_{i=1}^n f_i n_x \left(\frac{d_2}{d_1 + d_2} \right), & F_{1y} &= \sum_{i=1}^n f_i n_y \left(\frac{d_2}{d_1 + d_2} \right) \\ F_{2x} &= \sum_{i=1}^n f_i n_x \left(\frac{d_1}{d_1 + d_2} \right), & F_{2y} &= \sum_{i=1}^n f_i n_y \left(\frac{d_1}{d_1 + d_2} \right) \end{aligned} \quad (2.18)$$

where n is the total number of nodes on the edge, d_1 and d_2 are the distance from the given node to vertex 1 and 2, n_x and n_y represent the directions.

The coupling with the meshless methods can be implemented by a new strategy. The SPH-DDA interaction can be considered as the sphere-to-face contact type [70]. The interaction force consists of the normal and tangential force respecting the contact surface, as shown in Figure 2.7. The force \mathbf{F} applied on the fluid particles when in

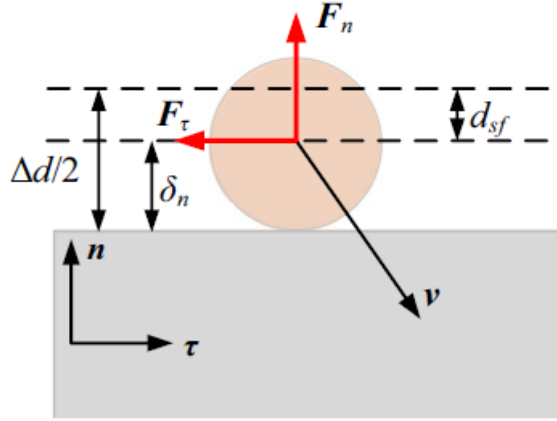


Figure 2.7: DDA and SPH interaction [70].

contact with the DDA solid, expressed as:

$$\mathbf{F} = \mathbf{F}_n + \mathbf{F}_\tau \quad (2.19)$$

where the normal components of force \mathbf{F}_n and the tangential components of the force \mathbf{F}_τ are:

$$\begin{aligned} \mathbf{F}_n &= [p\delta - k_d(\boldsymbol{\nu} \cdot \mathbf{n})] \cdot \mathbf{n} \\ \mathbf{F}_\tau &= -k_f |\mathbf{F}_n| \cdot \boldsymbol{\tau} \end{aligned} \quad (2.20)$$

where p is the penalty spring stiffness; k_d and k_f are the damping and friction coefficient, respectively; δ is the penetration distance; \mathbf{n} and $\boldsymbol{\tau}$ are the unit vector normal and tangential, respectively; $\boldsymbol{\nu}$ is the relative velocity vector.

The contact force also applied on the solid block i , which can be treated as a point loading and added to the force sum-matrices of DDA. The potential energy of the fluid loading is:

$$\begin{aligned}\Pi_{fluid} &= - (u, v) \begin{pmatrix} F_n \\ F_\tau \end{pmatrix} \\ &= -D_i^T T_i^T \begin{pmatrix} F_n \\ F_\tau \end{pmatrix}\end{aligned}\quad (2.21)$$

Then, the derivatives of the potential energy Π_{fluid} is added to the global matrix as an external loading.

2.5 Applications

Due to the unique advantages and continued development of the discontinuous deformation analysis method, it has been widely applied in geotechnical engineering. It is noted that a number of high-profile projects were analyzed by the DDA method, for example, the three gorges in China[15, 71], Gjovik Olympic Cavern in Norway [72], Pueblo Dam in Colorado[73], King Herod's Palace [74] and Masada national monument [75] in Israel and so on. Specifically, the original DDA was used for the rockfall [76, 77, 78], tunnel [79, 80, 81], and earthquake problems [82, 83, 84]; the extended DDA is widely applied for the blast [85, 86], fracture [87, 63] and wave impact [68], etc. The applications of the DDA method are shown in Figure 2.8.

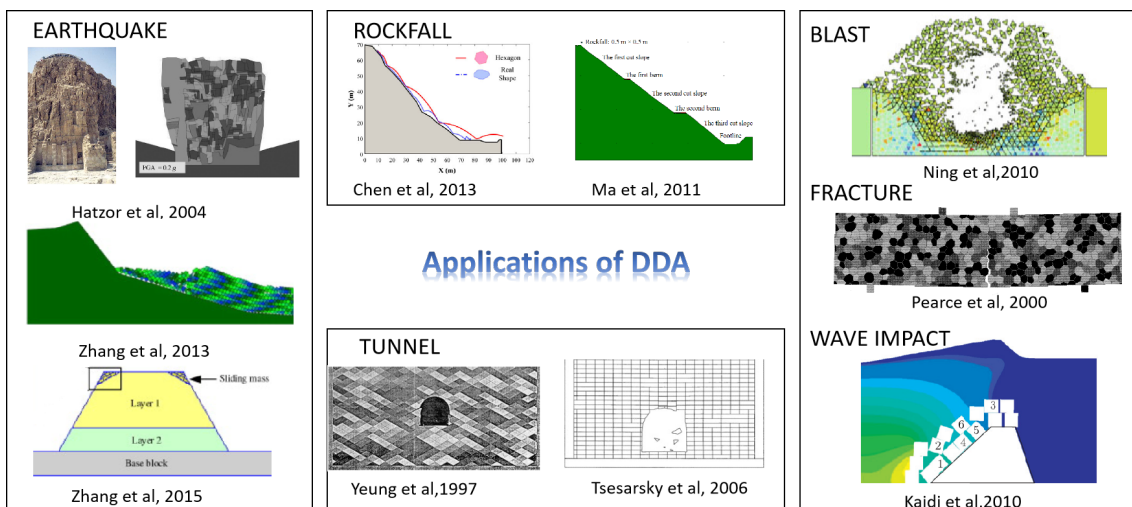


Figure 2.8: Applications of the DDA method

2.6 Development of 3D-DDA

3D-DDA is currently under extensive research, mainly about its basic theory. G-H Shi [88, 89] proposed the basic formulas of 3D-DDA, in which the sub-matrices of point load, initial stress, elastic deformation and inertia forces were provided. Beyabanaki et al. [90] further developed 3D-DDA with higher-order displacement functions. Jiao et al. [91, 92] presented a new 3D spherical DDA model. Some contact algorithms were developed to detect the contact between polygons. Jiang and Yeung [93, 94] developed a vertex-to-face model, Yeung et al. [95] and Wu [96] presented algorithms for edge-to-edge contacts. Liu et al. [97] and Yeung et al. [98, 99] introduced the ‘common-plane’ technique to the 3D-DDA method from other DEM methods. Keneti and Jafari [100] considered the main plane and main contact points to identify contact points and types. Beyabanaki and Mikola [101] provide a method of using the closest point search algorithm to identify the contact pattern between two blocks to improve efficiency. Wu et al. [102] proposed an effective and robust spatial contact detection algorithm, which uses a new multi-shell covering system and the decomposition of geometric sub-units, thereby greatly reducing the number of contact detection and the number of iterations. The improvement of the contact judgment algorithm is more and more valued by the majority of scholars because it accounts for nearly 80% of the total computational time. But so far, there is no efficient, universal, and suitable contact judgment algorithm for a large number of block analysis calculations in related articles.

Similar to 2D-DDA, three-dimensional programs have also been developed and coupled with other numerical technologies. Grayeli and Hatami [103] coupled the FEM and DDA method using four-noded tetrahedral elements to determine stresses and deformations in practical problems involving fissured elastic media. Wang et al. [104] proposed a coupled DDA–SPH method in three-dimensional case to study the landslide dams. However, it should be noted that although the theory and some development of 3D-DDA have been proposed, there is still no open-source or commercial solver released, so it is very necessary to develop a 3D program and on this basis, in-depth development of three-dimensional applications.

2.7 Concluding remarks

In this chapter, the validations, modifications, extensions and applications of the DDA method were presented and summarized, as shown in Figure 2.9

- For the validations of the DDA method, the sliding, rotation, impact and time

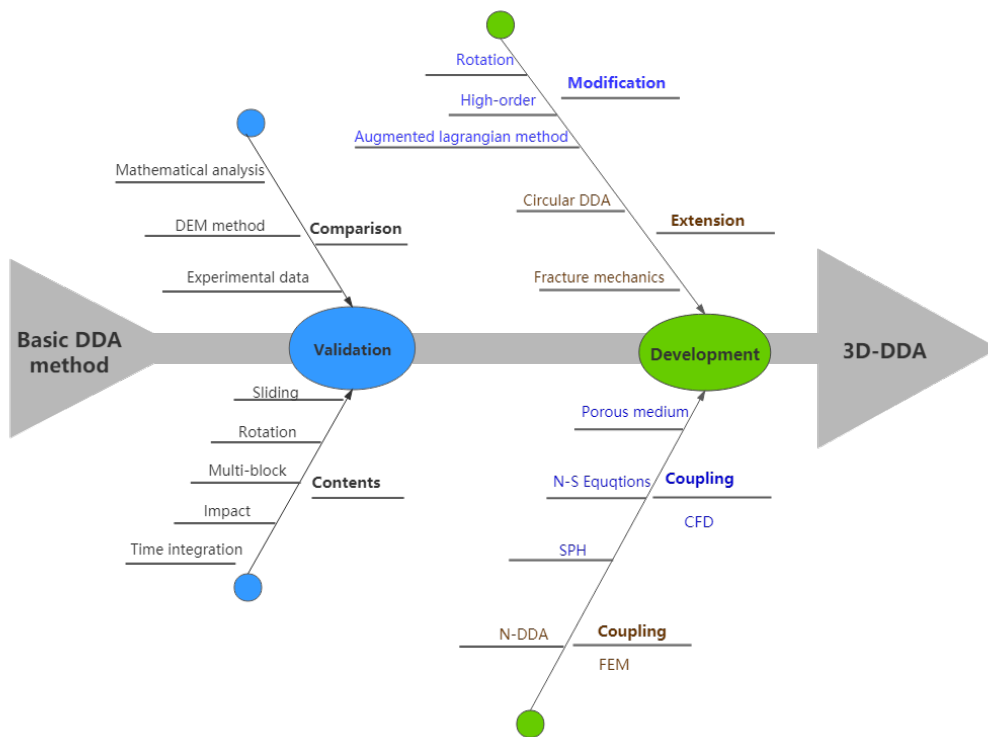


Figure 2.9: DDA state of the art

integration were verified by comparing with the mathematical analysis, other computational techniques and experimental data.

- For the modifications of the DDA method, the rotation errors were modified by post-correction or high-order displacement function, and some new contact mechanics methods were introduced.
- For the extensions of the DDA method, the coupling between the DDA with the FEM, the mathematical manifold and fluid mechanics were presented.
- For the applications, the DDA method was widely used in some high-profile projects as well as rockfall, tunnel, blast and earthquake problems, etc.
- Furthermore, the development of the basic formulas of 3D-DDA was introduced, however, there is no universal contact judgment algorithm for a large number of block analysis calculations proposed and there is still no open-source or commercial solver of 3D-DDA released.

The 2D or 3D DDA method should be developed and coupled with other numerical techniques, which will expand the applicability of the DDA method.

Theory of 2D-DDA and CFD/DDA

Coupling approach

3.1 Introduction

In this chapter, the governing equations of the fluid and solid method are introduced. The following aspects are emphasized:

- The 2D-DDA method is introduced briefly. The conditions of the contact surfaces are enforced through the penalty method in order to avoid the interpenetration between blocks.
- The fluid flow is described by the RANS equations. The Forchheimer equations are presented to calculate the flow in the non-linear porous medium.
- The Volume-Averaged Reynolds-Averaged Navier-Stokes (VARANS) equations are proposed, in which the extended Forchheimer law used to calculate the porous medium flow is added to the inertia terms of RANS equations.
- The coupling between the fluid and the solid is carried out by a transmission strategy of the fluid mesh nodes' pressure towards the solid polygon vertices.

3.2 Governing equations of 2D-DDA

In order to investigate the movement and the solid blocks, the Discontinuous Deformation Analysis (DDA) method is used. The DDA method does not have the meshing procedure of blocks and therefore, no refinement is needed to improve the quality of the calculated solution, which has the advantage of reducing the computation time [105, 106]. In the DDA method, the displacement (u, v) at any point (x, y) of a block i can be represented by six variables: two translations($u_0,$

v_0) of the block gravity center (x_0, y_0) in x and y directions, a rotation γ_0 around (x_0, y_0) , and two normal and a shear strains $(\varepsilon_{xx}, \varepsilon_{yy}, \varepsilon_{xy})$; therefore, the variables vector associated with the block i is given:

$$\mathbf{D}_i = \left(u_0, v_0, \gamma_0, \varepsilon_{xx}, \varepsilon_{yy}, \varepsilon_{xy} \right)^T \quad (3.1)$$

According to the first-order expression of any point (x, y) , the displacement (u, v) for an individual block i can be written as:

$$\mathbf{U}_i = \begin{pmatrix} u \\ v \end{pmatrix} = \mathbf{T}_i \mathbf{D}_i \quad (3.2)$$

where

$$\mathbf{T}_i = \begin{pmatrix} 1 & 0 & -(y - y_0) & (x - x_0) & 0 & (y - y_0)/2 \\ 0 & 1 & (x - x_0) & 0 & (y - y_0) & (x - x_0)/2 \end{pmatrix} \quad (3.3)$$

The strain of the block i can be expressed by the relationship between the strain and displacement:

$$\boldsymbol{\varepsilon}_i = \mathbf{L} \mathbf{U}_i \quad (3.4)$$

where $\mathbf{L} = \begin{pmatrix} \frac{\partial}{\partial x} & 0 \\ 0 & \frac{\partial}{\partial y} \\ \frac{1}{2} \frac{\partial}{\partial y} & \frac{1}{2} \frac{\partial}{\partial x} \end{pmatrix}$ is the differential operator matrix for 2D problem.

Substituting Equation (3.2) into Equation (3.4), we get:

$$\boldsymbol{\varepsilon}_i = \mathbf{L} \mathbf{T}_i \mathbf{D}_i = \mathbf{B} \mathbf{D}_i \quad (3.5)$$

Assuming that the deformation is elastic and linear, the stress tensor is written as follows:

$$\boldsymbol{\sigma}_i = \mathbf{E} \boldsymbol{\varepsilon}_i = \mathbf{E} \mathbf{B} \mathbf{D}_i \quad (3.6)$$

where \mathbf{E} is the elastic matrix of deformation planes and $\mathbf{B} = \begin{bmatrix} 0 & 0 & 0 & 1 & 0 & 0 \\ 0 & 0 & 0 & 0 & 1 & 0 \\ 0 & 0 & 0 & 0 & 0 & 1 \end{bmatrix}$.

The total potential energy Π_p of the block i , defined as the the sum of the elastic strain energy $\Pi_{elastic}$, initial stress potential energy $\Pi_{initialstress}$, body force potential energy $\Pi_{bodyforce}$, and inertial energy $\Pi_{inertia}$, is given by:

$$\begin{aligned}
\Pi_p &= \Pi_{elastic} + \Pi_{initialstress} + \Pi_{bodyforce} + \Pi_{inertia} \\
&= \int_{\Omega_i} \frac{1}{2} \boldsymbol{\varepsilon}_i^T \boldsymbol{\sigma}_i d\Omega_i + \int_{\Omega_i} \boldsymbol{\varepsilon}_i^T \boldsymbol{\sigma}_0 d\Omega_i - \int_{\Omega_i} \mathbf{U}_i^T \mathbf{f}_b d\Omega_i + \int_{\Omega_i} \mathbf{U}_i^T m \ddot{\mathbf{D}}_i d\Omega_i \quad (3.7)
\end{aligned}$$

By using Equation(3.2), it follows:

$$\Pi_p = \int_{\Omega_i} \frac{1}{2} \boldsymbol{\varepsilon}_i^T \mathbf{E} \boldsymbol{\varepsilon}_i d\Omega_i + \int_{\Omega_i} \boldsymbol{\varepsilon}_i^T \boldsymbol{\sigma}_0 d\Omega_i - \mathbf{D}_i^T \mathbf{T}_i^T \left(\int_{\Omega_i} \mathbf{f}_b d\Omega_i - \int_{\Omega_i} \mathbf{T}_i \ddot{\mathbf{D}}_i d\Omega_i \right) \quad (3.8)$$

where \mathbf{f}_b denotes the body forces applied on a block i , and M is the block mass per unit area. $\boldsymbol{\sigma}_0$ is the initial stress of the block.

Substituting Equation (3.5) and (3.6) into Equation (3.8), the total potential of a system of N blocks is expressed as:

$$\Pi_{np} = \sum_{i=1}^N \left(\mathbf{D}_i^T \mathbf{M} \ddot{\mathbf{D}}_i + \frac{1}{2} \mathbf{D}_i^T \mathbf{K} \mathbf{D}_i - \mathbf{D}_i^T \mathbf{f}_e \right) \quad (3.9)$$

where $\mathbf{M} = \int_{\Omega_i} M \mathbf{T}_i^T \mathbf{T}_i d\Omega_i$ is the mass matrix, $\mathbf{K} = \int_{\Omega_i} \mathbf{B}^T \mathbf{E} \mathbf{B} d\Omega_i$ is the stiffness matrix, $\mathbf{f}_e = \int_{\Omega_i} (\mathbf{T}_i^T \mathbf{f}_b - \mathbf{B}^T \boldsymbol{\sigma}_0) d\Omega_i$ is the external forces matrix. According to the minimized potential energy, the block system equations of motion can be represented in the compact form:

$$\frac{\partial \Pi_{np}}{\partial \mathbf{D}_i} = 0 \Rightarrow \mathbf{M} \ddot{\mathbf{D}} + \mathbf{K} \mathbf{D} = \mathbf{F} \quad (3.10)$$

Then, the displacement and the velocity in Equation (3.10) can be approximated by the Newmark- β method:

$$\begin{aligned}
\mathbf{D}_{n+1} &= \mathbf{D}_n + \Delta t \dot{\mathbf{D}}_n + \frac{\Delta t^2}{2} \left[(1 - 2\beta_1) \ddot{\mathbf{D}}_n + 2\beta_1 \ddot{\mathbf{D}}_{n+1} \right] \\
\dot{\mathbf{D}}_{n+1} &= \dot{\mathbf{D}}_n + \Delta t \left[(1 - \beta_2) \ddot{\mathbf{D}}_n + \beta_2 \ddot{\mathbf{D}}_{n+1} \right]
\end{aligned} \quad (3.11)$$

where $\ddot{\mathbf{D}}$ and $\dot{\mathbf{D}}$ are the acceleration and velocity matrices, respectively, and $\beta_1 = 1/2$ and $\beta_2 = 1$ for the implicit scheme ([22]). Substituting Equation (3.11) into Equation (3.10), we obtain:

$$\left(\mathbf{K} + \frac{2\mathbf{M}}{\Delta t^2} \right) \mathbf{D}_{n+1} = \mathbf{F} + \frac{2\mathbf{M}}{\Delta t} \dot{\mathbf{D}}_n \quad (3.12)$$

And then the compact form is given by:

$$\hat{K}D = \hat{F} \quad (3.13)$$

Consequently, we get the global matrix:

$$\begin{pmatrix} \hat{K}_{11} & \hat{K}_{12} & \hat{K}_{13} & \dots & \hat{K}_{1n} \\ \hat{K}_{21} & \hat{K}_{22} & \hat{K}_{23} & \dots & \hat{K}_{2n} \\ \hat{K}_{31} & \hat{K}_{32} & \hat{K}_{33} & \dots & \hat{K}_{3n} \\ \vdots & \vdots & \vdots & \vdots & \vdots \\ \hat{K}_{n1} & \hat{K}_{n2} & \hat{K}_{n3} & \dots & \hat{K}_{nn} \end{pmatrix} \begin{pmatrix} D_1 \\ D_2 \\ D_3 \\ \vdots \\ D_n \end{pmatrix} = \begin{pmatrix} \hat{F}_1 \\ \hat{F}_2 \\ \hat{F}_3 \\ \vdots \\ \hat{F}_n \end{pmatrix} \quad (3.14)$$

where \hat{F}_i and D_i are the sub-matrices of force and displacement, which are 6×1 sub-matrices. The \hat{K}_{ij} is 6×6 sub-matrix. Sub-matrix \hat{K}_{ij} ($i = j$) is determined by the block material properties, whereas \hat{K}_{ij} ($i \neq j$) is related to the contacts between blocks. The stiffness sub-matrix \hat{K}_{ij} can be explained by the example as shown in Figure 3.1. There are three blocks which have two contacts: (Block 1, Block 2) and (Block 1, Block3), as shown in Figure 3.1(a), the stiffness sub-matrices of the three blocks \hat{K}_{ij} ($i, j = 1, 2, 3$) as indicated in Figure 3.1(b), where the gray diagonal partitions are contributed by deformation of block i , while the other parts are derived from contact springs. Because there is no contact between Block 2 and 3, the contact stiffness sub-matrix $\hat{K}_{23} = \hat{K}_{32} = 0$.

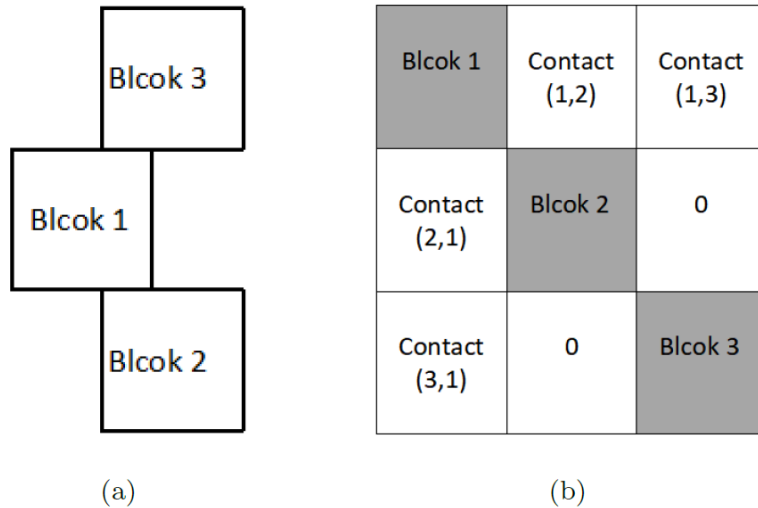


Figure 3.1: The structure of stiffness matrix in the case of three blocks:(a) Location of three blocks; (b) Structure of stiffness matrix

Thereafter, it should be noted that when the contact between the blocks takes place,

the associated potential energy must be added to the global equilibrium equation (Equation (3.7)), and then the associated contact sub-matrices have to be added to the global matrix Equation (3.14). In the present study, the surface contact constraints of blocks are enforced by the penalty method. Taking the contact of two blocks i and j as an example, the point P_1 moves into edge P_2P_3 of block j and stops at point P_1' , the penetration distance between blocks is δ . Using the penalty method is equivalent to placing a spring between the two blocks, as shown in Figure 3.2.

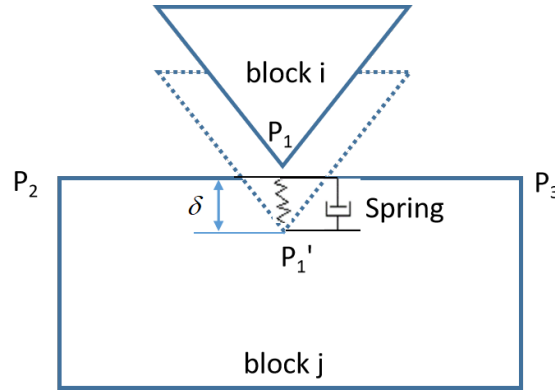


Figure 3.2: Interaction between two contacting blocks

The strain energy of the contact spring reads:

$$\Pi_{contact} = \frac{1}{2}P\delta^2 \quad (3.15)$$

where P is the coefficient of penalty which can vary between $10E$ and $1000E$, where E denotes Young's modulus ([9]). The block kinematics of the DDA method are obtained by the open-close iteration which is adding or removing a stiff spring in each time step at the contact position where tension and interpenetration do not exist.

3.3 Validations of 2D-DDA

3.3.1 Case1: Frictionless impact - Free fall

In order to examine the accuracy of the DDA method, the progress of the free fall and the elastic rebound was simulated. The simulation consisted of $1\ m \times 1\ m$ block falling $5.0\ m$ onto a $1\ m \times 10\ m$ base block with four fixed points, as shown in Figure 3.3(a). We have an initial velocity of $0\ m/s$, and we assume an acceleration

due to the gravity of 10 m/s^2 . The velocity of fall and rebound can be written as:

$$\begin{cases} V_{fall} = V_0 + gt & 0 \leq t \leq 1 \\ V_{rebound} = V_t - gt & 1 < t \leq \frac{V_t}{g} \end{cases} \quad (3.16)$$

where V_{fall} and $V_{rebound}$ are the velocity during the fall and rebound. V_t is the velocity when the block reaches the impact plane.

The velocity of free fall and rebound for four various contact stiffness values was simulated using the DDA method. The theoretical value of free fall and elastic rebound velocity after the frictionless impact was calculated by Equation (3.16), and the numerical results are shown in Figure 3.3(b), where we assume that the contact stiffness is related to the Young modulus of block material [23]. The results (Figure 3.3(b)) show that the greater the contact stiffness is, the less the impact damping will be. It shows that the best agreement between theoretical and numerical results is met when the contact stiffness value is around 10^9 N/m . It is worth noting that for smaller contact stiffness, the penetration overlap is large and then the impact between blocks becomes inelastic.

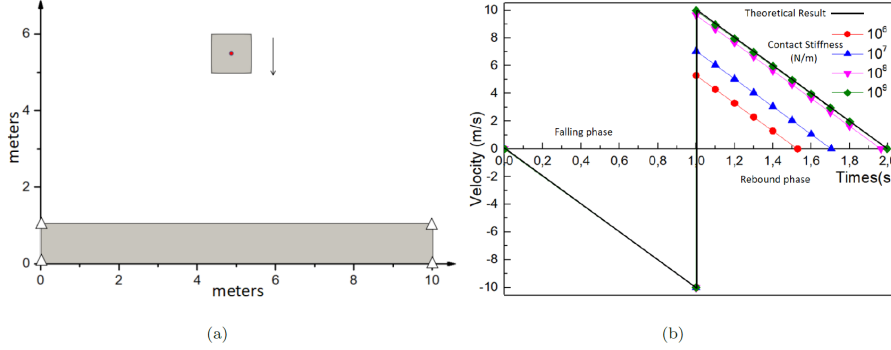


Figure 3.3: Falling block for testing frictionless impact and elastic rebound: (a) Schematic diagram of free fall motion; (b) Comparison between the theoretical value (Equation (3.16)) and DDA results for different contact stiffness

3.3.2 Case 2: Multi-blocks under seismic loading

The second validation is carried out by comparing the DDA numerical results with both the experimental and the numerical results given by Komodromos et al. [36]. Thus, the behavior of seven $48 \text{ mm} \times 48 \text{ mm} \times 29 \text{ mm}$ blocks with a mass of 135.5 g under harmonic excitations (at the base) is simulated by DDA wherein we assume that the contact stiffness is 10^7 N/m and friction angle ϕ is 34° , and the peak ground

accelerations is 2.15 m/s^2 . For four different frequencies, the computed results are compared with the experimental observations. The DDA simulations show similar responses to experimental observations, as shown in Figure 3.4. Furthermore, compared to the DEM results, the DDA results have higher accuracy.

For four different frequencies, the acceleration ($a_{initiate}$) to initiate the rocking or sliding is calculated by the DDA model. The results from the experimental have a great agreement with the numerical simulations, as shown in Figure 3.5. Therefore, the DDA can be used to investigate the displacement of the vertical caisson and the discrete rear structures.

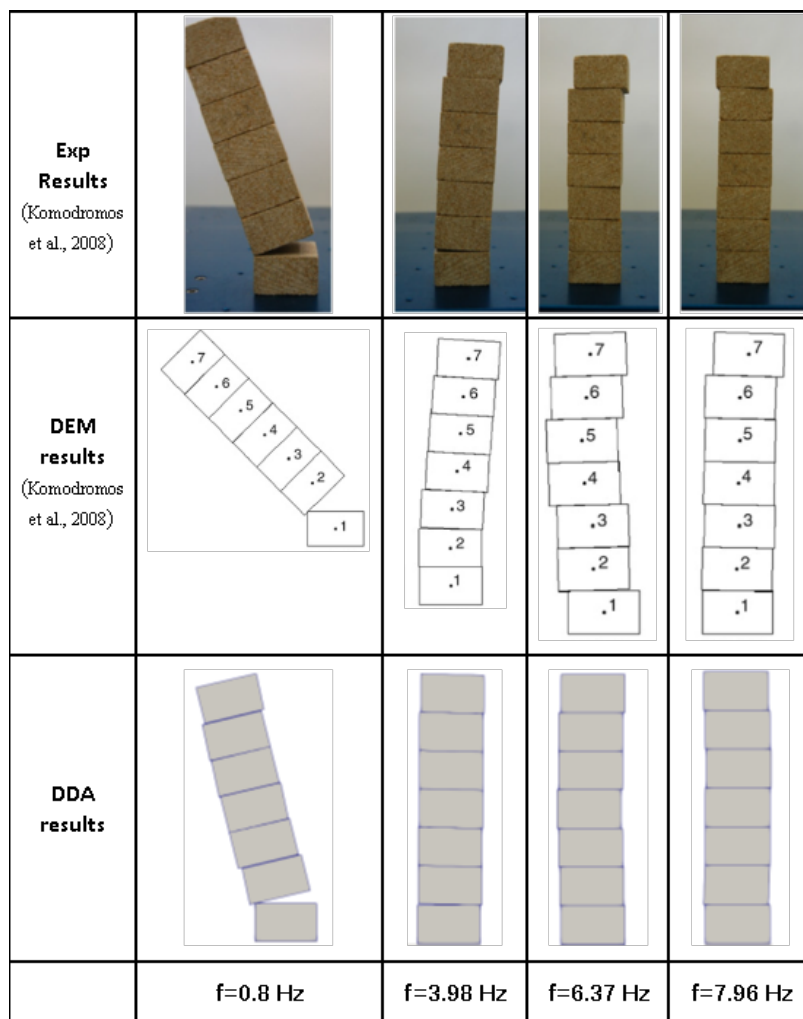


Figure 3.4: Comparison between the experimental results [36] and the numerical results computed by DEM and DDA. The dimension of one block is $48 \text{ mm} \times 48 \text{ mm} \times 29 \text{ mm}$, the mass is 135.5 g , the contact stiffness is 10^7 N/m , the friction angle is $\phi = 34^\circ$, and the peak ground accelerations is 2.15 m/s^2

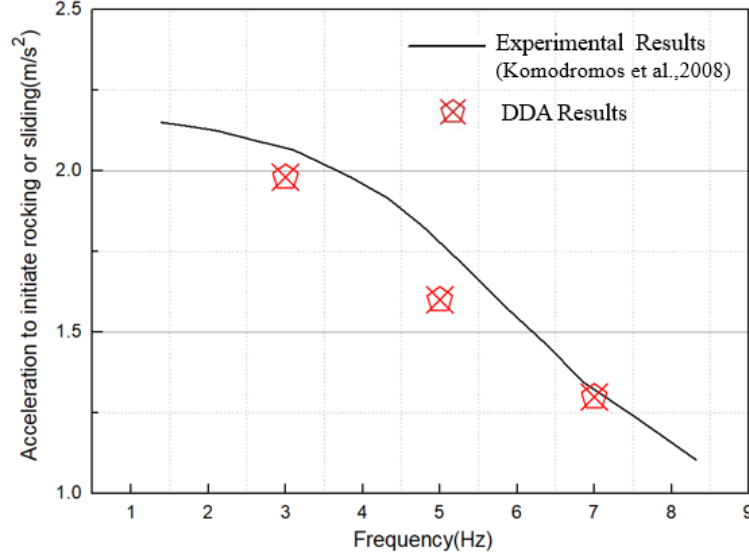


Figure 3.5: Comparison between the experimental values of $a_{initiate}$ [36] and DDA results.

3.4 Governing equations of fluid

3.4.1 RANS equations for turbulent flow

The fluid flow is described by the Reynolds-Averaged Navier–Stokes (RANS) equations. The mass and momentum conservation functions are [107, 108]:

$$\frac{\partial \rho}{\partial t} + \nabla \cdot (\rho \mathbf{U}) = 0 \quad (3.17)$$

$$\frac{\partial(\rho \mathbf{U})}{\partial t} + \nabla \cdot (\rho \mathbf{U} \mathbf{U}) = -\nabla P + \mathbf{g} \cdot \mathbf{X} \nabla \rho + \nabla (\mu_{eff} \nabla \mathbf{U}) + \sigma \kappa \nabla \alpha \quad (3.18)$$

where \mathbf{U} is the velocity vector, \mathbf{X} is the Cartesian position vector, \mathbf{g} denotes the gravitational acceleration vector, and ρ represents the weighted averaged density. The term $\mu_{eff} = \mu + \mu_t$, where μ is the weighted average dynamic viscosity and the μ_t is the dynamic turbulence viscosity calculated by $k - \varepsilon$ model. $\sigma \kappa \nabla \alpha$ signifies the surface tension effects, where σ is the surface tension, α is the fluid volume fraction, and $\kappa = \nabla \frac{\alpha}{|\alpha|}$.

3.4.2 Extended Forchheimer equations for porous medium

Darcy's law has been traditionally used for describing the transport properties of porous media; however, as the flow velocity increases, Darcy's law became in-applicable as the relationship between pressure and velocity becomes non-linear.

A correction term (see the second term in Equation(3.19)), based on a quadratic velocity, was added by Forchheimer [109] to take this non-linearity into account. Furthermore, in the present study, an added mass term C_A [110] was considered. To accelerate the same volume of water in a porous medium, additional momentum is required [111]. The extended Forchheimer equation can be written as:

$$P_{porous} = A\mathbf{U} + B\mathbf{U}|\mathbf{U}| + \frac{\rho}{n}C_A \frac{\partial \mathbf{U}}{\partial t} \quad (3.19)$$

where P_{porous} is the porous medium pressure, and the coefficients A and B are [112, 110]:

$$A = \mu_1 \frac{(1-n)^3}{n^2} \frac{\mu}{D_{50}^2} \quad (3.20)$$

$$B = \mu_2 \left(1 + \frac{7.5}{K_C}\right) \frac{1-n}{n^2} \frac{\rho}{D_{50}} \quad (3.21)$$

where D_{50} is the mean diameter of the porous material. μ_1 and μ_2 are empirical coefficients related to the linear and nonlinear drag force, respectively. $K_C = \frac{T_o U_M}{n D_{50}}$ is the Keulegan-Carpenter number where U_M is the maximum oscillatory velocity. T_o is the period of the oscillation [112].

3.4.3 Volume-averaged RANS equation for incompressible fluid-porous medium coupling

In what follows, we consider an incompressible flow. Thus, in order to correspond to the extended Forchheimer Equation (3.19) with the RANS equations, we introduce the volume-averaged velocity $\langle \mathbf{U} \rangle$ that exists in the interstices of the solid framework of the porous medium, given by:

$$\langle \mathbf{U} \rangle = \frac{1}{V} \int_{V_f} \mathbf{U} dV \quad (3.22)$$

where \mathbf{U} is the hydrodynamic velocity with respect to the fluid, V is the total volume, and V_f is the part of V which is occupied by the fluid. In what follows, we set the porosity $n = \frac{V_f}{V}$. Then, by substituting volume-averaged velocity Equation (3.22) in the RANS Equations (3.17-3.18), we obtain the following VARANS equations for incompressible fluid:

$$\nabla \cdot \langle \mathbf{U} \rangle = 0 \quad (3.23)$$

$$\begin{aligned}
(1 + C_A) \frac{\rho}{n} \frac{\partial}{\partial t} \langle \mathbf{U} \rangle + \frac{\rho}{n^2} \langle \mathbf{U} \rangle \nabla \langle \mathbf{U} \rangle = & -\nabla P + \mathbf{g} X \cdot \nabla \rho + \frac{1}{n} \nabla \left(\mu_{eff} \nabla \langle \mathbf{U} \rangle \right) \\
& + \sigma \kappa \nabla \alpha - A \frac{\langle \mathbf{U} \rangle}{n} - B \left| \frac{\langle \mathbf{U} \rangle}{n} \right| \frac{\langle \mathbf{U} \rangle}{n}
\end{aligned} \tag{3.24}$$

where $C_A = 0.34$ denotes the added mass coefficient, which is kept constant in the present study [110].

3.4.4 VOF method

The computational model is built with a two-phase model (Fluid-air) and the free surface that separates these two phases can cut a cell of the computational mesh into two unequal parts. Each part contains a quantity of each phase. In what follows, the Volume-of-Fluid (VOF) method is used to describe the volume fraction of the fluid inside each computational cell which will be transmitted to VARANS. It is based on the following transport equation [113]:

$$\frac{\partial \alpha}{\partial t} + \frac{1}{n} \nabla \cdot \left(\alpha \langle \mathbf{U} \rangle \right) + \frac{1}{n} \nabla \cdot \left(\alpha (1 - \alpha) \langle \mathbf{U}_c \rangle \right) = 0 \tag{3.25}$$

where α is the fluid phase fraction laying between 0 and 1, where $\alpha=0$ corresponds to full of air and $\alpha=1$ corresponds to full of fluid. However, in order to obtain physical results, there must be some limitations: a clear interface must be maintained, and α must be limited between 0 and 1. Weller et al. [114] added an artificial compression term $\nabla \cdot \alpha(1 - \alpha)$. This method only uses non-zero values at the interface. In addition, $|\langle \mathbf{U}_c \rangle| = [\min(C_\alpha |\langle \mathbf{U} \rangle|), \max(|\langle \mathbf{U} \rangle|)]$, where the factor C_α can be specified. If $|\langle \mathbf{U}_c \rangle|$ is normal to the interface, the fluid will not be compressed, which points to a larger value of α and therefore from the air to the water phase. The boundedness of this equation is achieved by the specially designed solver MULES (multi-dimensional universal limiter for explicit solution).

In the present study, the VARANS models (see Equations (3.23-3.25)) are solved by using the PIMPLE algorithm (pressure implicit with the splitting of operators) [115] to compute the pressure and SIMPLE (semi-implicit method for pressure-linked equations) algorithm to obtain the velocity fields. Its main structure is inherited from the original PISO but allows equations to be relaxed to ensure the convergence of all equations at each time step ([110, 116]).

3.5 Coupling procedure of Fluid-Solid interaction

The coupling between the fluid and the solid models requires a transfer of data from one model to another. In our case, the fluid model uses meshes while the solid model is meshless (see Figure 3.6 (a)) since it is based on the DDA method. Therefore, an adequate data transfer strategy is required in order to faithfully reproduce the studied physical phenomena ([68]). It consists of converting the nodal pressure forces of the fluid (f_i, f_j) into equivalent forces F_i at the vertex points of the solid (see Figure 3.6 (b)-(c) and Equation (3.27)). It is specified that in this fluid-solid coupling, the transfer is retroactive, where the fluid transfers to the solid the pressure force, a force considered external to the solid.

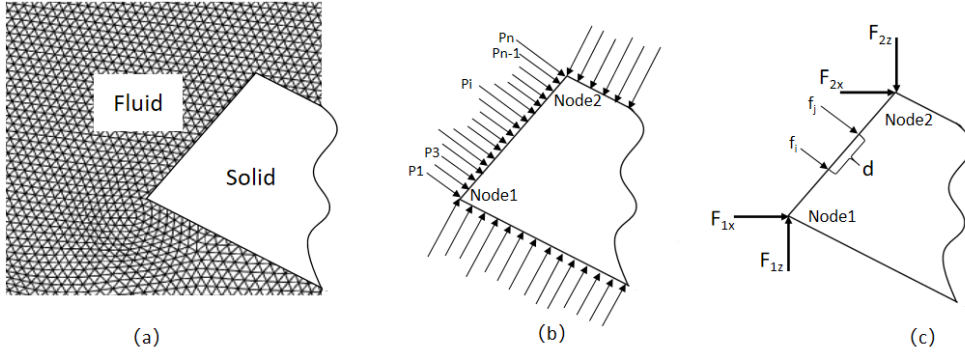


Figure 3.6: Fluid/solid interface: (a) fluid finite element mesh and solid; (b) fluid pressures in the mesh points; (c) conversion of fluid pressures into equivalent vertex forces.

$$f_i = p_i \frac{d}{2}; f_j = p_j \frac{d}{2} \quad (3.26)$$

where p_i and p_j are the fluid pressures at nodes i and j , and d is the distance of the finite element edge from node i to node j . Finally, the global forces (F_1, F_2) acting on the DDA block can be written as:

$$\begin{aligned} F_{1x} &= \sum_{i=1}^n f_i n_x \left(\frac{d_2}{d_1 + d_2} \right), & F_{1y} &= \sum_{i=1}^n f_i n_z \left(\frac{d_2}{d_1 + d_2} \right) \\ F_{2x} &= \sum_{i=1}^n f_i n_x \left(\frac{d_1}{d_1 + d_2} \right), & F_{2y} &= \sum_{i=1}^n f_i n_z \left(\frac{d_1}{d_1 + d_2} \right) \end{aligned} \quad (3.27)$$

where n is the total number of nodes in the edge, d_1 and d_2 are the distances from the given node to vertices 1 and 2, and n_x and n_y represent the directions along x and y respectively.

The hydrodynamic force applied on the solid block i , which can be treated as a point

loading and added to the force sum-matrices of DDA. The potential energy of the fluid loading is:

$$\begin{aligned}\Pi_{fluid} &= - (u, v) \begin{pmatrix} F_x \\ F_y \end{pmatrix} \\ &= -\mathbf{D}_i^T \mathbf{T}_i^T \begin{pmatrix} F_x \\ F_y \end{pmatrix}\end{aligned}\quad (3.28)$$

The potential energy Π_{fluid} is minimized by taking the derivatives:

$$\begin{aligned}f_r &= -\frac{\partial \Pi_{fluid}}{\partial d_{ri}} = \frac{\partial}{\partial d_{ri}} \mathbf{D}_i^T \mathbf{T}_i^T \begin{pmatrix} F_x \\ F_y \end{pmatrix} \\ &= \mathbf{T}_i^T \begin{pmatrix} F_x \\ F_y \end{pmatrix} \quad (r = 1, \dots, 6) \rightarrow \hat{\mathbf{F}}_i\end{aligned}\quad (3.29)$$

which is a 6×1 sub-matrix that is added to $\hat{\mathbf{F}}_i$ in the global Equation (3.14).

3.6 Concluding remarks

In this chapter, the governing equations of fluid based on the Volume-Averaged RANS equation and the solid based on the 2D-DDA method were introduced.

The 2D-DDA method with the penalty was introduced briefly. The kinematic conditions of the contact surfaces were enforced through the penalty method in order to avoid the inter-penetration between blocks. This method enabled us to take into account the shapes of solid structures, as well as the contact between blocks. The validations of the 2D-DDA method were done by comparing the numerical results with the theoretical and the experimental results.

The Volume-Averaged Reynolds-Averaged Navier-Stokes (VARANS) equations were proposed, in which the extended Forchheimer law used to calculate the porous medium flow was added to the inertia terms of RANS equations.

The coupling between the fluid and the solid was carried out by transmitting the pressure of the fluid mesh nodes to the solid polygon vertices. The hydrodynamic force applied on the solid block, which can be treated as a point loading and added to the global equilibrium equation.

Mathematical formulation of the 3D-DDA method

4.1 Introduction

The two-dimensional approach may only provide a rough approximation of actual behavior. In order to solve the environmental problems accurately, a robust three-dimensional approach is required. This chapter presents the mathematical formulations of 3D-DDA and introduces the corresponding program procedure. The following aspects are emphasized:

- The minimum potential energy method is used in the 3D-DDA method;
- The common-plane method is used to detect the contact between blocks;
- The contact is divided in two types, which are vertex-to-face contact and vertex-to-vertex contact, corresponding normal and shear springs as well as frictional forces are added based on the contact type.
- Open-close iteration and soft contact method are used to avoid penetrations between blocks. The SOR method is used to solve linear system equations.

4.2 Displacement function and global equilibrium equations

4.2.1 Displacement function

In this part we will go from standard 2D analysis to 3D Discontinuous Deformation Analysis (3D-DDA), the following two basic assumptions are still valid:

- (1) Each time step satisfies the conditions of very small displacement and deformation;

- (2) The stresses and strains of the blocks are constant.

Let (u, v, w) be the displacements of any point of coordinates (x, y, z) that belongs to block i . These displacements can be expressed as a function of the vector D_i :

$$D_i^T = (u_0, v_0, w_0, \alpha_0, \beta_0, \gamma_0, \varepsilon_x, \varepsilon_y, \varepsilon_z, \gamma_{xy}, \gamma_{yz}, \gamma_{xz}) \quad (4.1)$$

where (u_0, v_0, w_0) is the rigid translation vector at block i centroid (x_0, y_0, z_0) ; $(\alpha_0, \beta_0, \gamma_0)$ is the rotation vector around x, y and z axis of the point (x_0, y_0, z_0) ; and $(\varepsilon_x, \varepsilon_y, \varepsilon_z, \gamma_{xy}, \gamma_{yz}, \gamma_{xz})$ are the normal and shear strains in the block i .

Assuming constant strains and stress within each block, the first-order approximation can be used, the displacements (u, v, w) of the point (x, y, z) of block i , can be written as:

$$\begin{aligned} u &= a_0 + a_1x + a_2y + a_3z \\ v &= b_0 + b_1x + b_2y + b_3z \\ w &= c_0 + c_1x + c_2y + c_3z \end{aligned} \quad (4.2)$$

The displacements of the center of gravity of block i are written in the following form:

$$\begin{aligned} u_0 &= a_0 + a_1x_0 + a_2y_0 + a_3z_0 \\ v_0 &= b_0 + b_1x_0 + b_2y_0 + b_3z_0 \\ w_0 &= c_0 + c_1x_0 + c_2y_0 + c_3z_0 \end{aligned} \quad (4.3)$$

By combining Equations (4.2) and (4.3), we get:

$$\begin{aligned} u &= a_1(x - x_0) + a_2(y - y_0) + a_3(z - z_0) + u_0 \\ v &= b_1(x - x_0) + b_2(y - y_0) + b_3(z - z_0) + v_0 \\ w &= c_1(x - x_0) + c_2(y - y_0) + c_3(z - z_0) + w_0 \end{aligned} \quad (4.4)$$

The normal strains of blocks are:

$$\varepsilon_x = \frac{\partial u}{\partial x} = a_1; \quad \varepsilon_y = \frac{\partial v}{\partial y} = b_2; \quad \varepsilon_z = \frac{\partial w}{\partial z} = c_3 \quad (4.5)$$

The rotation of the point (x, y) can be expressed as:

$$\begin{aligned} \alpha_0 &= \frac{1}{2} \left(\frac{\partial w}{\partial y} - \frac{\partial v}{\partial z} \right) = \frac{1}{2} (c_2 - b_3) \\ \beta_0 &= \frac{1}{2} \left(\frac{\partial u}{\partial z} - \frac{\partial w}{\partial x} \right) = \frac{1}{2} (a_3 - c_1) \\ \gamma_0 &= \frac{1}{2} \left(\frac{\partial v}{\partial x} - \frac{\partial u}{\partial y} \right) = \frac{1}{2} (b_1 - a_2) \end{aligned} \quad (4.6)$$

The shear strains are given by:

$$\begin{aligned}
\gamma_{xy} &= \frac{\partial u}{\partial y} + \frac{\partial v}{\partial x} = a_2 + b_1 \\
\gamma_{yz} &= \frac{\partial v}{\partial z} + \frac{\partial w}{\partial y} = b_3 + c_2 \\
\gamma_{zx} &= \frac{\partial u}{\partial z} + \frac{\partial w}{\partial x} = a_3 + c_1
\end{aligned} \tag{4.7}$$

Therefore, we can get the parameters:

$$\begin{aligned}
a_1 &= \varepsilon_x, & b_2 &= \varepsilon_y, & c_3 &= \varepsilon_z \\
c_2 &= \frac{1}{2}\gamma_{yz} + \alpha_0, & b_3 &= \frac{1}{2}\gamma_{yz} - \alpha_0, & a_3 &= \frac{1}{2}\gamma_{zx} + \beta_0 \\
c_1 &= \frac{1}{2}\gamma_{zx} - \beta_0, & b_1 &= \frac{1}{2}\gamma_{xy} + \gamma_0, & a_2 &= \frac{1}{2}\gamma_{xy} - \gamma_0
\end{aligned} \tag{4.8}$$

For reasons of simplification we denote: $\bar{X} = x - x_0$, $\bar{Y} = y - y_0$, $\bar{Z} = z - z_0$, then Equation (4.2) represents as:

$$\begin{pmatrix} u \\ v \\ w \end{pmatrix} = \begin{pmatrix} 1 & 0 & 0 & 0 & \bar{Z} & -\bar{Y} & \bar{X} & 0 & 0 & \bar{Y}/2 & 0 & \bar{Z}/2 \\ 0 & 1 & 0 & \bar{Z} & 0 & \bar{X} & 0 & \bar{Y} & 0 & \bar{X}/2 & \bar{Z}/2 & 0 \\ 0 & 0 & 1 & \bar{Y} & -\bar{X} & 0 & 0 & 0 & \bar{Z} & 0 & \bar{Y}/2 & \bar{X}/2 \end{pmatrix} \begin{pmatrix} u_0 \\ v_0 \\ w_0 \\ \alpha_0 \\ \beta_0 \\ \gamma_0 \\ \varepsilon_x \\ \varepsilon_y \\ \varepsilon_z \\ \gamma_{xy} \\ \gamma_{yz} \\ \gamma_{zx} \end{pmatrix} \tag{4.9}$$

which can be written in a compact form:

$$\mathbf{U}_i = \begin{pmatrix} u \\ v \\ w \end{pmatrix} = \mathbf{T}_i \mathbf{D}_i \tag{4.10}$$

where T_i is:

$$T_i = \begin{pmatrix} 1 & 0 & 0 & 0 & \bar{Z} & -\bar{Y} & \bar{X} & 0 & 0 & \bar{Y}/2 & 0 & \bar{Z}/2 \\ 0 & 1 & 0 & \bar{Z} & 0 & \bar{X} & 0 & \bar{Y} & 0 & \bar{X}/2 & \bar{Z}/2 & 0 \\ 0 & 0 & 1 & \bar{Y} & -\bar{X} & 0 & 0 & 0 & \bar{Z} & 0 & \bar{Y}/2 & \bar{X}/2 \end{pmatrix} \quad (4.11)$$

4.2.2 Global equilibrium equations

The total potential energy Π_p of the N blocks, defined as the sum of all potential energy, is given by:

$$\Pi_p = \Pi_{elastic} + \Pi_{initialstress} + \Pi_{pointload} + \Pi_{bodyforce} + \Pi_{inertia} + \Pi_{contact} \quad (4.12)$$

where

- Π_p is the total potential energy;
- $\Pi_{elastic}$ is the elastic strain energy;
- $\Pi_{initialstress}$ is the initial stress potential energy;
- $\Pi_{pointload}$ is the point loading energy;
- $\Pi_{bodyforce}$ is the body force potential energy;
- $\Pi_{inertia}$ is the inertial energy;
- $\Pi_{contact}$ is the potential energy contributed due to contacts between blocks.

The total potential Π_p can be written as:

$$\Pi_p = \frac{1}{2} \begin{pmatrix} D_1^T & D_2^T & D_3^T & \cdots & D_n^T \end{pmatrix} \begin{bmatrix} K_{11} & K_{12} & K_{13} & \cdots & K_{1n} \\ K_{21} & K_{22} & K_{23} & \cdots & K_{2n} \\ K_{31} & K_{32} & K_{33} & \cdots & K_{3n} \\ \vdots & \vdots & \vdots & \ddots & \vdots \\ K_{n1} & K_{n2} & K_{n3} & \cdots & K_{nn} \end{bmatrix} \begin{pmatrix} D_1 \\ D_2 \\ D_3 \\ \vdots \\ D_n \end{pmatrix} + \begin{pmatrix} D_1^T & D_2^T & D_3^T & \cdots & D_n^T \end{pmatrix} \left\{ \begin{matrix} F_1 \\ F_2 \\ F_3 \\ \vdots \\ F_n \end{matrix} \right\} \quad (4.13)$$

where the sub-matrices K_{ii} and K_{ij} are 12×12 sub-matrices, and the K_{ii} depends on the material properties of block i , K_{ij} ($i \neq j$) represents the contacts between blocks i and j . F_i and D_i are 12×1 sub-matrices, F_i is the loading sub-matrix which respects twelve unknown variables of block i (see Equation (4.1)).

According to the minimized potential energy, the block system equations of motion can be represented as:

$$\frac{\partial \Pi_p}{\partial \mathbf{d}_{ri}} = 0, \quad r = 1, 2, 3, \dots, 12 \quad (4.14)$$

where \mathbf{d}_{ri} is the displacement variable of block i . Therefore, we can get the global equilibrium equation:

$$\begin{bmatrix} \mathbf{K}_{11} & \mathbf{K}_{12} & \mathbf{K}_{13} & \dots & \mathbf{K}_{1n} \\ \mathbf{K}_{21} & \mathbf{K}_{22} & \mathbf{K}_{23} & \dots & \mathbf{K}_{2n} \\ \mathbf{K}_{31} & \mathbf{K}_{32} & \mathbf{K}_{33} & \dots & \mathbf{K}_{3n} \\ \vdots & \vdots & \vdots & \vdots & \vdots \\ \mathbf{K}_{n1} & \mathbf{K}_{n2} & \mathbf{K}_{n3} & \dots & \mathbf{K}_{nn} \end{bmatrix} \begin{bmatrix} \mathbf{D}_1 \\ \mathbf{D}_2 \\ \mathbf{D}_3 \\ \vdots \\ \mathbf{D}_n \end{bmatrix} = \begin{bmatrix} \mathbf{F}_1 \\ \mathbf{F}_2 \\ \mathbf{F}_3 \\ \vdots \\ \mathbf{F}_n \end{bmatrix} \quad (4.15)$$

4.3 Governing equations of sub-matrices

4.3.1 Sub-matrix of elastic strain

The elastic strain energy of block i is:

$$\Pi_{elastic} = \iiint_{\Omega_i} \frac{1}{2} (\sigma_x \varepsilon_x + \sigma_y \varepsilon_y + \sigma_z \varepsilon_z + \tau_{xy} \gamma_{xy} + \tau_{yz} \gamma_{yz} + \tau_{zx} \gamma_{zx}) dx dy dz \quad (4.16)$$

where the integration is done in the entire volume Ω_i of block i . We assume the blocks are linearly elastic, thus the relationship between stress and strain can be expressed as follows:

$$\begin{pmatrix} \sigma_x \\ \sigma_y \\ \sigma_z \\ \tau_{yz} \\ \tau_{zx} \\ \tau_{xy} \end{pmatrix} = \frac{E}{(1-\nu^2)(1-2\nu)} \begin{pmatrix} 1-\nu & \nu & \nu & 0 & 0 & 0 \\ \nu & 1-\nu & \nu & 0 & 0 & 0 \\ \nu & \nu & 1-\nu & 0 & 0 & 0 \\ 0 & 0 & 0 & \frac{1}{2}-\nu & 0 & 0 \\ 0 & 0 & 0 & 0 & \frac{1}{2}-\nu & 0 \\ 0 & 0 & 0 & 0 & 0 & \frac{1}{2}-\nu \end{pmatrix} \begin{pmatrix} \varepsilon_x \\ \varepsilon_y \\ \varepsilon_z \\ \gamma_{yz} \\ \gamma_{zx} \\ \gamma_{xy} \end{pmatrix} \quad (4.17)$$

where E is the Young's modulus and ν is the Poisson's ratio of block material. It can be written in a compact form:

$$\boldsymbol{\sigma}_i = \mathbf{E} \boldsymbol{\varepsilon}_i \quad (4.18)$$

where \mathbf{E} is the elastic matrix of deformation block:

$$\mathbf{E} = \frac{E}{(1 - \nu^2)(1 - 2\nu)} \begin{pmatrix} 1 - \nu & \nu & \nu & 0 & 0 & 0 \\ \nu & 1 - \nu & \nu & 0 & 0 & 0 \\ \nu & \nu & 1 - \nu & 0 & 0 & 0 \\ 0 & 0 & 0 & \frac{1}{2} - \nu & 0 & 0 \\ 0 & 0 & 0 & 0 & \frac{1}{2} - \nu & 0 \\ 0 & 0 & 0 & 0 & 0 & \frac{1}{2} - \nu \end{pmatrix} \quad (4.19)$$

The strain of the block i can be expressed by the relationship between the strain and displacement:

$$\boldsymbol{\varepsilon}_i = \mathbf{L}\mathbf{U}_i \quad (4.20)$$

where \mathbf{L} is the differential operator matrix for 3D problem. Substituting Equation (4.10) into Equation (4.20), we get:

$$\boldsymbol{\varepsilon}_i = \mathbf{L}\mathbf{T}_i\mathbf{D}_i = \mathbf{B}\mathbf{D}_i \quad (4.21)$$

Assuming that the deformation is elastic and linear, the stress tensor is written as follows:

$$\boldsymbol{\sigma}_i = \mathbf{E}\boldsymbol{\varepsilon}_i = \mathbf{E}\mathbf{B}\mathbf{D}_i \quad (4.22)$$

The block strain energy represents as:

$$\begin{aligned} \Pi_{elastic} &= \frac{1}{2} \iiint_{\Omega_i} (\varepsilon_x \quad \varepsilon_y \quad \varepsilon_z \quad \gamma_{yz} \quad \gamma_{zx} \quad \gamma_{xy}) \begin{pmatrix} \sigma_x \\ \sigma_y \\ \tau_z \\ \tau_{yz} \\ \tau_{zx} \\ \tau_{xy} \end{pmatrix} dx dy dz \\ &= \frac{1}{2} \iiint_{\Omega_i} \mathbf{D}_i^T \mathbf{B}^T \mathbf{E} \mathbf{B} \mathbf{D}_i dx dy dz \end{aligned} \quad (4.23)$$

where the $\mathbf{E}_i = \mathbf{B}^T \mathbf{E} \mathbf{B}$ is a 12×12 matrix:

$$\mathbf{E}_i = \frac{E}{(1-\nu^2)(1-2\nu)} \begin{pmatrix} 0 & 0 & 0 & 0 & 0 & 0 & 0 & 0 & 0 & 0 & 0 & 0 & 0 \\ 0 & 0 & 0 & 0 & 0 & 0 & 0 & 0 & 0 & 0 & 0 & 0 & 0 \\ 0 & 0 & 0 & 0 & 0 & 0 & 0 & 0 & 0 & 0 & 0 & 0 & 0 \\ 0 & 0 & 0 & 0 & 0 & 0 & 0 & 0 & 0 & 0 & 0 & 0 & 0 \\ 0 & 0 & 0 & 0 & 0 & 0 & 0 & 0 & 0 & 0 & 0 & 0 & 0 \\ 0 & 0 & 0 & 0 & 0 & 0 & 0 & 0 & 0 & 0 & 0 & 0 & 0 \\ 0 & 0 & 0 & 0 & 0 & 0 & 1-\nu & \nu & \nu & 0 & 0 & 0 & 0 \\ 0 & 0 & 0 & 0 & 0 & 0 & \nu & 1-\nu & \nu & 0 & 0 & 0 & 0 \\ 0 & 0 & 0 & 0 & 0 & 0 & \nu & \nu & 1-\nu & 0 & 0 & 0 & 0 \\ 0 & 0 & 0 & 0 & 0 & 0 & 0 & 0 & 0 & \frac{1}{2}-\nu & 0 & 0 & 0 \\ 0 & 0 & 0 & 0 & 0 & 0 & 0 & 0 & 0 & 0 & \frac{1}{2}-\nu & 0 & 0 \\ 0 & 0 & 0 & 0 & 0 & 0 & 0 & 0 & 0 & 0 & 0 & \frac{1}{2}-\nu & 0 \end{pmatrix} \quad (4.24)$$

Therefore, the block strain energy can be written as:

$$\begin{aligned} \Pi_{elastic} &= \frac{1}{2} \iiint_{\Omega_i} \mathbf{D}_i^T \mathbf{E}_i \mathbf{D}_i dx dy dz \\ &= \frac{V_i}{2} \mathbf{D}_i^T \mathbf{E}_i \mathbf{D}_i \end{aligned} \quad (4.25)$$

where V_i is the volume of block i . Based on the minimization of the strain energy $\Pi_{elastic}$, we have:

$$\begin{aligned} K_{rs} &= \frac{\partial^2 \Pi_e}{\partial d_{ri} \partial d_{si}} \\ &= \frac{V_i}{2} \frac{\partial^2}{\partial d_{ri} \partial d_{si}} (\mathbf{D}_i^T \mathbf{E}_i \mathbf{D}_i) \\ &= V_i \mathbf{E}_i \quad r, s = 1, 2, 3 \dots, 12 \rightarrow \mathbf{K}_{ii} \end{aligned} \quad (4.26)$$

which is added to the sub-matrix \mathbf{K}_{ii} in the global Equation (4.15).

4.3.2 Sub-matrix of initial stress

The potential energy due to the initial stress is expressed as:

$$\begin{aligned}
 \Pi_{initialstress} &= \iiint_{\Omega_i} (\varepsilon_x \sigma_x^0 + \varepsilon_y \sigma_y^0 + \varepsilon_z \sigma_z^0 + \gamma_{xy} \tau_{xy}^0 + \gamma_{yz} \tau_{yz}^0 + \gamma_{zx} \tau_{zx}^0) dx dy dz \\
 &= V_i (\varepsilon_x \quad \varepsilon_y \quad \varepsilon_z \quad \gamma_{xy} \quad \gamma_{yz} \quad \gamma_{zx}) \begin{pmatrix} \sigma_x^0 \\ \sigma_y^0 \\ \sigma_z^0 \\ \tau_{xy}^0 \\ \tau_{yz}^0 \\ \tau_{zx}^0 \end{pmatrix} \\
 &= V_i \mathbf{D}_i^T \boldsymbol{\sigma}_0
 \end{aligned} \tag{4.27}$$

where the initial stress $\boldsymbol{\sigma}_0 = (0 \quad 0 \quad 0 \quad 0 \quad 0 \quad 0 \quad \sigma_x^0 \quad \sigma_y^0 \quad \sigma_z^0 \quad \tau_{xy}^0 \quad \tau_{yz}^0 \quad \tau_{zx}^0)^T$.

The derivatives f_r are calculated to minimize the potential energy $\Pi_{initialstress}$:

$$f_r = -\frac{\partial \Pi_{initialstress}}{\partial d_{ri}} = V_i \boldsymbol{\sigma}_0 \quad (r = 1, \dots, 12) \rightarrow \mathbf{F}_i \tag{4.28}$$

which is added to the sub-matrix \mathbf{F}_i in the global Equation (4.15).

4.3.3 Sub-matrix of point loading

Assuming that the point loading force acting on the point (x, y, z) of block i is (F_x, F_y, F_z) , the point loading potential energy is expressed as:

$$\begin{aligned}
 \Pi_{pointload} &= -(F_x u + F_y v + F_z w) = -(u, v, w) \begin{pmatrix} F_x \\ F_y \\ F_z \end{pmatrix} \\
 &= -\mathbf{D}_i^T \mathbf{T}_i^T \begin{pmatrix} F_x \\ F_y \\ F_z \end{pmatrix}
 \end{aligned} \tag{4.29}$$

The potential energy $\Pi_{pointload}$ is minimized by taking the derivative:

$$\begin{aligned}
f_r &= -\frac{\partial \Pi_{\text{pointload}}}{\partial d_{ri}} = \frac{\partial}{\partial d_{ri}} \mathbf{D}_i^T \mathbf{T}_i^T \begin{pmatrix} F_x \\ F_y \\ F_z \end{pmatrix} \\
&= \mathbf{T}_i^T \begin{pmatrix} F_x \\ F_y \\ F_z \end{pmatrix} \quad (r = 1, \dots, 12) \rightarrow \mathbf{F}_i
\end{aligned} \tag{4.30}$$

which is a 12×1 sub-matrix that is added to \mathbf{F}_i in the global Equation (4.15).

4.3.4 Sub-matrix of body force

Assuming that the body force (f_x, f_y, f_z) is the constant volume load acting on block i , then the potential energy is:

$$\begin{aligned}
\Pi_{\text{bodyforce}} &= -\iiint_{\Omega_i} (u \quad v \quad w) \begin{pmatrix} f_x \\ f_y \\ f_z \end{pmatrix} dx dy dz \\
&= -\mathbf{D}_i^T \left(\iiint_{\Omega_i} \mathbf{T}_i^T dx dy dz \right) \begin{pmatrix} f_x \\ f_y \\ f_z \end{pmatrix}
\end{aligned} \tag{4.31}$$

The coordinates of centre of gravity of block i are (x_0, y_0, z_0) which can be expressed as:

$$x_0 = \frac{S_x}{V_i}, \quad y_0 = \frac{S_y}{V_i}, \quad z_0 = \frac{S_z}{V_i} \tag{4.32}$$

where $S_x = \iiint_{\Omega_i} x dx dy dz$, $S_y = \iiint_{\Omega_i} y dx dy dz$, $S_z = \iiint_{\Omega_i} z dx dy dz$ and $V_i = \iiint_{\Omega_i} dx dy dz$. V_i is the volume of block i .

Then

$$\iiint_{\Omega_i} \mathbf{T}_i^T dx dy dz = \begin{pmatrix} V_i & 0 & 0 \\ 0 & V_i & 0 \\ 0 & 0 & V_i \\ 0 & -(S_z - z_0 V_i) & (S_y - y_0 V_i) \\ (S_z - z_0 V_i) & 0 & -(S_x - x_0 V_i) \\ -(S_y - y_0 V_i) & (S_x - x_0 V_i) & 0 \\ (S_x - x_0 V_i) & 0 & 0 \\ 0 & (S_y - y_0 V_i) & 0 \\ 0 & 0 & (S_z - z_0 V_i) \\ 0 & (S_z - z_0 V_i) & (S_y - y_0 V_i) / 2 \\ (S_z - z_0 V_i) / 2 & 0 & (S_x - x_0 V_i) / 2 \\ (S_y - y_0 V_i) / 2 & (S_x - x_0 V_i) & 0 \end{pmatrix} = \begin{pmatrix} V_i & 0 & 0 \\ 0 & V_i & 0 \\ 0 & 0 & V_i \\ 0 & 0 & 0 \\ 0 & 0 & 0 \\ 0 & 0 & 0 \\ 0 & 0 & 0 \\ 0 & 0 & 0 \\ 0 & 0 & 0 \\ 0 & 0 & 0 \\ 0 & 0 & 0 \\ 0 & 0 & 0 \end{pmatrix} \quad (4.33)$$

The potential energy is minimized by deriving the $\Pi_{bodyforce}$:

$$f_r = -\frac{\partial \Pi_{bodyforce}}{\partial d_{ri}} = (f_x V_i \quad f_y V_i \quad f_z V_i \quad 0 \quad 0)^T \rightarrow \mathbf{F}_i \quad (4.34)$$

which is a 12×1 sub-matrix that is added to \mathbf{F}_i in the global Equation (4.15).

4.3.5 Sub-matrix of inertia force

Using the $(u(t), v(t), w(t))$ to represent the time-dependent displacement of any point (x, y, z) in block i and M to donate the mass per unit volume. The inertia force of block i is:

$$\begin{pmatrix} f_x \\ f_y \\ f_z \end{pmatrix} = -M \frac{\partial^2}{\partial t^2} \begin{pmatrix} u(t) \\ v(t) \\ w(t) \end{pmatrix} = -M \mathbf{T}_i \frac{\partial^2 \mathbf{D}_i(t)}{\partial t^2} \quad (4.35)$$

The potential energy of the inertia force is written as:

$$\begin{aligned} \Pi_{inertia} &= -\iiint_{\Omega_i} (u \quad v \quad w) \begin{pmatrix} f_x \\ f_y \\ f_z \end{pmatrix} dx dy dz \\ &= \iiint_{\Omega_i} M \mathbf{D}_i^T \mathbf{T}_i^T \mathbf{T}_i \frac{\partial^2 \mathbf{D}_i(t)}{\partial t^2} dx dy dz \end{aligned} \quad (4.36)$$

Assume $\mathbf{D}_i(0) = 0$ is the block displacement at the beginning of the time step, Δt is the time step interval and $\mathbf{D}_i(\Delta) = \mathbf{D}_i$ is the block displacement at the end of the time step. Based on the time integration, we get:

$$\mathbf{D}_i(\Delta) = \mathbf{D}_i(0) + \Delta t \frac{\partial \mathbf{D}_i(0)}{\partial t} + \frac{\Delta t^2}{2} \frac{\partial^2 \mathbf{D}_i(0)}{\partial t^2} = \Delta t \frac{\partial \mathbf{D}_i(0)}{\partial t} + \frac{\Delta t^2}{2} \frac{\partial^2 \mathbf{D}_i(0)}{\partial t^2} \quad (4.37)$$

Assuming the acceleration in each time is constant,

$$\frac{\partial^2 \mathbf{D}_i(t)}{\partial t^2} = \frac{\partial^2 \mathbf{D}(0)}{\partial t^2} = \frac{2}{\Delta t^2} \mathbf{D}_i - \frac{2}{\Delta t} \frac{\partial \mathbf{D}_i(0)}{\partial t} \quad (4.38)$$

where

$$\mathbf{V}_i(0) = \frac{\partial \mathbf{D}_i(0)}{\partial t} \quad (4.39)$$

Therefore, we have the potential energy at the end of time step,

$$\Pi_{inertia} = \mathbf{D}_i^T \iiint_{\Omega_i} \mathbf{T}_i^T \mathbf{T}_i dx dy dz \left(\frac{2M}{\Delta t^2} \mathbf{D}_i - \frac{2M}{\Delta t} \mathbf{V}_i(0) \right) \quad (4.40)$$

To reach equilibrium, the potential energy of inertia force is minimized by taking derivatives with respect to the block displacement variables:

$$f_r = -\frac{\partial \Pi_{inertia}}{\partial d_{ri}} = -\frac{\partial}{\partial d_{ri}} \left(M \mathbf{D}_i^T \iiint_{\Omega_i} \mathbf{T}_i^T \mathbf{T}_i dx dy dz \left(\frac{2}{\Delta t^2} \mathbf{D}_i - \frac{2}{\Delta t} \frac{\partial \mathbf{D}_i(0)}{\partial t} \right) \right) \quad (4.41)$$

$r = 1, 2, \dots, 12$

which can be transformed into two parts:

$$\begin{aligned} \frac{2M}{\Delta t^2} \iiint_{\Omega_i} \mathbf{T}_i^T \mathbf{T}_i dx dy dz &\rightarrow \mathbf{K}_{ii} \\ \frac{2M}{\Delta t} \left(\iiint_{\Omega_i} \mathbf{T}_i^T \mathbf{T}_i dx dy dz \right) \mathbf{V}_i(0) &\rightarrow \mathbf{F}_i \end{aligned} \quad (4.42)$$

which are added to the sub-matrices \mathbf{K}_{ii} and \mathbf{F}_i in the global Equation (4.15).

For the next step, the initial velocity inherits the end velocity of this step, from the Equation (4.38), we get:

$$\mathbf{V}_i(\Delta t) \approx \mathbf{V}_i(0) + \Delta t \frac{\partial^2 \mathbf{D}_i(t)}{\partial t^2} = \frac{2}{\Delta t} \mathbf{D}_i - \mathbf{V}_i(0) \quad (4.43)$$

In what follow, the analytical solution of the matrix integral $\iiint_{\Omega_i} \mathbf{T}_i^T \mathbf{T}_i dx dy dz$ are

calculated:

$$\mathbf{T}^T \mathbf{T} = \begin{bmatrix} 1 & 0 & 0 \\ 0 & 1 & 0 \\ 0 & 0 & 1 \\ 0 & -\bar{z} & \bar{y} \\ \bar{z} & 0 & -\bar{x} \\ -\bar{y} & \bar{x} & 0 \\ \bar{x} & 0 & 0 \\ 0 & \bar{y} & 0 \\ 0 & 0 & \bar{z} \\ \bar{y}/2 & \bar{x}/2 & 0 \\ 0 & \bar{z}/2 & \bar{y}/2 \\ \bar{z}/2 & 0 & \bar{x}/2 \end{bmatrix} \begin{pmatrix} 1 & 0 & 0 & 0 & \bar{z} & -\bar{y} & \bar{x} & 0 & 0 & \bar{y}/2 & 0 & \bar{z}/2 \\ 0 & 1 & 0 & -\bar{z} & 0 & \bar{x} & 0 & \bar{y} & 0 & \bar{x}/2 & \bar{z}/2 & 0 \\ 0 & 0 & 1 & \bar{y} & -\bar{x} & 0 & 0 & 0 & \bar{z} & 0 & \bar{y}/2 & \bar{x}/2 \end{pmatrix} \quad (4.44)$$

where $\bar{x} = x - x_0$, $\bar{y} = y - y_0$, $\bar{z} = z - z_0$, and (x_0, y_0, z_0) is the centroid of the block i . The basic integrals in block i are introduced:

$$V_i = \iiint_{\Omega_i} dx dy dz \quad S_x = \iiint_{\Omega_i} x dx dy dz \quad S_y = \iiint_{\Omega_i} y dx dy dz \quad S_z = \iiint_{\Omega_i} z dx dy dz \quad (4.45)$$

Therefore,

$$x_0 = \frac{S_x}{V_i} \quad y_0 = \frac{S_y}{V_i} \quad z_0 = \frac{S_z}{V_i} \quad (4.46)$$

The matrix elements of the integral are calculated as follows:

$$\begin{aligned} \iint_{\Omega_i} \bar{x} dx dy dz &= \iiint_{\Omega_i} (x - x_0) dx dy dz = S_x - x_0 V_i = 0 \\ \iint_{\Omega_i} \bar{y} dx dy dz &= \iiint_{\Omega_i} (y - y_0) dx dy dz = S_y - y_0 V_i = 0 \\ \iint_{\Omega_i} \bar{z} dx dy dz &= \iiint_{\Omega_i} (z - z_0) dx dy dz = S_z - z_0 V_i = 0 \\ \iint_{\Omega_i} \bar{x}^2 dx dy dz &= \iiint_{\Omega_i} (x - x_0)^2 dx dy dz = S_1 \\ \iint_{\Omega_i} \bar{y}^2 dx dy dz &= \iiint_{\Omega_i} (y - y_0)^2 dx dy dz = S_2 \\ \iint_{\Omega_i} \bar{z}^2 dx dy dz &= \iiint_{\Omega_i} (z - z_0)^2 dx dy dz = S_3 \\ \iint_{\Omega_i} \bar{x} \bar{y} dx dy dz &= \iiint_{\Omega_i} (x - x_0)(y - y_0) dx dy dz = S_4 \\ \iint_{\Omega_i} \bar{y} \bar{z} dx dy dz &= \iiint_{\Omega_i} (y - y_0)(z - z_0) dx dy dz = S_5 \\ \iint_{\Omega_i} \bar{z} \bar{x} dx dy dz &= \iiint_{\Omega_i} (z - z_0)(x - x_0) dx dy dz = S_6 \end{aligned} \quad (4.47)$$

Then, we can obtain the matrix integral $\iiint_{\Omega_i} \mathbf{T}_i^T \mathbf{T}_i dx dy dz$:

$$\iiint_{\Omega_i} \mathbf{T}_i^T \mathbf{T}_i dx dy dz = \begin{bmatrix} \mathbf{T}_{11} & \mathbf{T}_{12} \\ \mathbf{T}_{21} & \mathbf{T}_{22} \end{bmatrix} \quad (4.48)$$

where

$$\mathbf{T}_{11} = \begin{bmatrix} V_i & 0 & 0 & 0 & 0 & 0 \\ 0 & V_i & 0 & 0 & 0 & 0 \\ 0 & 0 & V_i & 0 & 0 & 0 \\ 0 & 0 & 0 & S_2 + S_3 & -S_4 & -S_6 \\ 0 & 0 & 0 & -S_4 & S_1 + S_3 & -S_5 \\ 0 & 0 & 0 & -S_6 & -S_5 & S_1 + S_2 \end{bmatrix}$$

$$\mathbf{T}_{12} = \begin{bmatrix} 0 & 0 & 0 & 0 & 0 & 0 \\ 0 & 0 & 0 & 0 & 0 & 0 \\ 0 & 0 & 0 & 0 & 0 & 0 \\ 0 & -S_5 & S_5 & -S_6/2 & (S_2 - S_3)/2 & S_4/2 \\ S_6 & 0 & -S_6 & S_5/2 & -S_4/2 & (S_3 - S_1)/2 \\ -S_4 & S_4 & 0 & (S_1 - S_2)/2 & S_6/2 & -S_5/2 \end{bmatrix}$$

$$\mathbf{T}_{12} = \mathbf{T}_{21}^T$$

$$\mathbf{T}_{22} = \begin{bmatrix} S_1 & 0 & 0 & S_4/2 & 0 & S_6/2 \\ 0 & S_2 & 0 & S_4/2 & S_5/2 & 0 \\ 0 & 0 & S_3 & 0 & S_5/2 & S_6/2 \\ S_4/2 & S_4/2 & 0 & (S_1 + S_2)/4 & S_6/4 & S_5/4 \\ 0 & S_5/2 & S_5/2 & S_6/4 & (S_2 + S_3)/4 & S_4/4 \\ S_6/2 & 0 & S_6/2 & S_5/4 & S_4/4 & (S_1 + S_3)/4 \end{bmatrix}$$

It should be noted that the elements of matrix integral can be obtained by the three-dimensional simplex integral method [88, 100], for example, $S_{(1-6)}$ can be expressed by the corner coordinates of a polyhedron. For details, please refer to sub-Section 4.5.

4.4 Contact between blocks

The three-dimensional block contact detection and transfer algorithms are one of the central tasks for all discrete element methods [117]. A robust and efficient algorithm for contact detection and updating is the primary direction of the future development of DEM [13]. The three-dimensional block contact detection algorithms must be

used to judge contact types and locations and the appropriate state of each contact, which can be open, sliding or locked [93]. The direct method was used in the origin 2D-DDA method; however, this method is not suitable for 3D-DDA due to the large computational effort; therefore, in this thesis, the Common-Plane Method (CPM) is introduced to apply in the 3D-DDA program.

4.4.1 Common-Plane Method

The three-dimensional contact detection of polyhedral blocks is classified into six basic types [118]: vertex-to-vertex, edge-to-face, face-to-face, vertex-to-vertex, vertex-to-edge, and edge-to-edge, as shown in Figure 4.1.

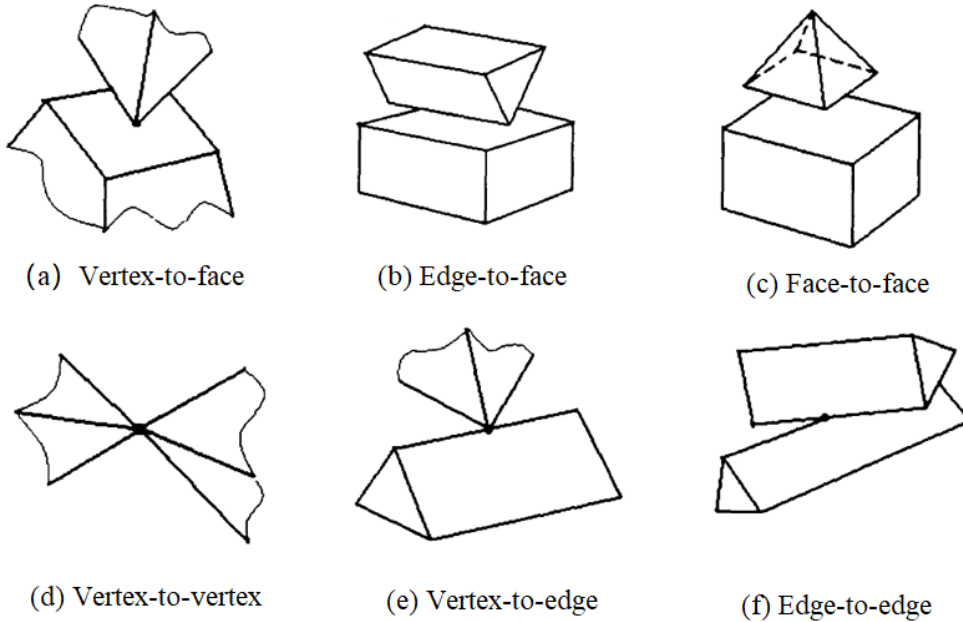


Figure 4.1: Basic contact types between two 3-D blocks

Barbosa et al. [119] introduced a simple algorithm for contact detection between polyhedrons that requires detecting all the vertices, edges and faces of blocks. The total detection number N is shown in Equation (4.49). The algorithm has a high computational complexity of order $O(n^2)$, with n being the number of blocks.

$$N = \prod_{i=1}^n (v_i + e_i + f_i) \quad (4.49)$$

Although we can reduce the detection number according to classify contact types [120], for example, three and more edge-face contacts at some point can be classified as edge-edge contact, the calculation amount is still very large. For DDA anal-

ysis, the direct method is extremely time consuming and not adopted for practical problem.

Cundall [121] introduced the Common-Plane Method (CPM). A Common-Plane (CP) is a plane that, in some sense, bisects the space between the two contacting blocks. If the two blocks are in contact, then both will intersect the CP, and if they are not in contact, then neither intersects the CP. As a result of using CP, the expensive block-to-block contact detection problem reduces to a much faster plane-to-block contact detection problem. Once the CP is established between two blocks, the normal to the CP defines the direction of the contact normal, which in turn defines the direction of the normal contact force between the two blocks. This is especially advantageous for vertex-to-vertex or edge-to-vertex contacts, where the definition of the contact normal is a non-trivial problem. This method has the complexity of order $O(n)$ and is widely used in some 3D DEM codes [122, 123, 124]. In this thesis, we applied the CPM technique to the 3D-DDA program.

4.4.1.1 Algorithm to position the Common-Plane

The CP is defined by two vectors (a) the normal unit vector \mathbf{n} of the common-plane and (b) position vector \mathbf{V}_C where P_C is any point at the common plane [122], as shown in Figure 4.2. Assume the P_A and P_B are one of vertex of two polygons A and B, \mathbf{V}_A and \mathbf{V}_B are the position vector, the distance d_A and d_B can be expressed as:

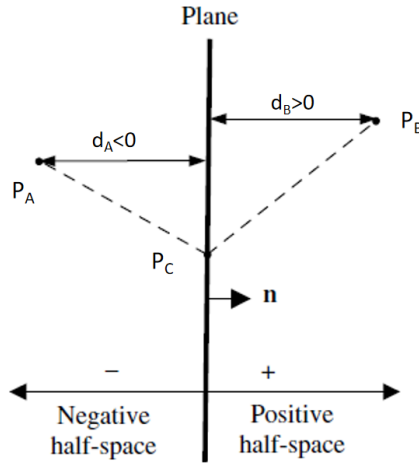


Figure 4.2: Definition of distances and sign convention of a point to a plane.

$$\begin{aligned} d_A &= \max \{ \mathbf{n} \cdot (\mathbf{V}_A - \mathbf{V}_C) \} & d_A < 0 \\ d_B &= \min \{ \mathbf{n} \cdot (\mathbf{V}_B - \mathbf{V}_C) \} & d_B > 0 \end{aligned} \quad (4.50)$$

where \mathbf{V}_A , \mathbf{V}_B and \mathbf{V}_C are the vectors from centroid O to point P_A , P_B and P_C .

The CP between the blocks A and B should meet three conditions [122]:

- Centroids of blocks A and B are located on opposite sides of the CP;
- The gap $d = d_B - d_A$ reaches maximum;
- $d_A = -d_B$.

In order to meet the three conditions, the CP can be positioned by two main procedures:

(1) Specify the reference point P_C and normal unit vector \mathbf{n} .

The initial CP is placed in the middle between the centroids of the two blocks, and the normal vector points from one centroid to the other centroid. Then the gap $d = d_B - d_A$ is calculated. If $d > \text{CRTL}$ (CRTL is a small positive tolerance defined by the user), the blocks will be recognized as non-contact and no CP will be generated (see Figure 4.3(a)). The real contact is the contact with $d < 0$ (see Figure 4.3(c)). The "potential contact" means that blocks A and B may form new contacts when $0 < d < \text{CRTL}$ (see Figure 4.3(b)), where in the common plane should move to:

$$\mathbf{V}_C = \frac{1}{2}(\mathbf{V}_{Amax} + \mathbf{V}_{Bmin}) \quad (4.51)$$

where \mathbf{V}_{Amax} is the vertex on block A nearest to the CP, \mathbf{V}_{Bmin} is the vertex on block B nearest to the CP.

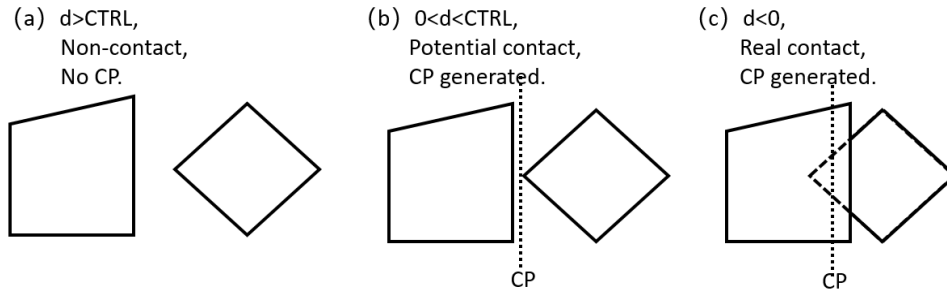


Figure 4.3: Two blocks contacts and the CP: (a) Non-contact, (b) Potential contact, (c) Real contact

(2) Rotate the CP to find the maximum gap.

The second stage is an iterative process, in which the normal vector \mathbf{n} corresponding to the maximum gap is found by rotating CP around the reference point. In three dimensions, two arbitrary orthogonal axes \mathbf{p} and \mathbf{q} are selected in the CP, and the origin is the reference point. Then, CP is disturbed around them in both negative

and positive sense; therefore, four perturbations are made as:

$$\begin{aligned}
 \mathbf{n} &= (\mathbf{n} + K\mathbf{p})/\sqrt{(1 + K^2)} \\
 \mathbf{n} &= (\mathbf{n} - K\mathbf{p})/\sqrt{(1 + K^2)} \\
 \mathbf{n} &= (\mathbf{n} + K\mathbf{q})/\sqrt{(1 + K^2)} \\
 \mathbf{n} &= (\mathbf{n} - K\mathbf{q})/\sqrt{(1 + K^2)}
 \end{aligned} \tag{4.52}$$

where K is the perturbation parameter. If the gap generated by any disturbance is greater than the gap of the current CP, the new CP will replace the current CP. In this case, the nearest vertex and reference point will be updated based on the newly found CP. A flowchart of the algorithm of common plane method has been created as previously described, and is shown in Figure 4.4.

4.4.1.2 Contact types detected by CPM

The type of contact is important because it determines the mechanical response of the contact. Contact types can be detected by CPM according to the number of vertices touching with CP, as shown in Table. 4.1.

Table 4.1: Contact types detected by Common-Plane Method

Number of vertices touching		Contact type	Illustration
Block i	Block j		
0	0	Null	
1	1	Vertex-to-vertex	Figure4.1(d)
1	2	Vertex-to-edge	Figure4.1(e)
1	>2	Vertex-to-face	Figure4.1(a)
2	1	Edge-to-vertex	Figure4.1(e)
2	2	Edge-to-edge	Figure4.1(f)
2	>2	Edge-to-face	Figure4.1(b)
>2	1	Face-to-vertex	Figure4.1(a)
>2	2	Face-to-edge	Figure4.1(b)
>2	>2	Face-to-face	Figure4.1(c)

Traditionally, the contact types of the block can be transformed into vertex-to-face contact [125, 126]. Obviously, contact types vertex-to-face, edge-to-face and face-to-face can be considered simply as a combination of vertex-face contacts. In those cases, the block face which will contact with another block vertex is selected as the entrance face. However, for the contact types vertex-to-vertex, vertex-to-edge and edge-to-edge, there is no entrance face that can be found. Therefore, the contact types can be classified into two categories: (i) the first is the contact that can be

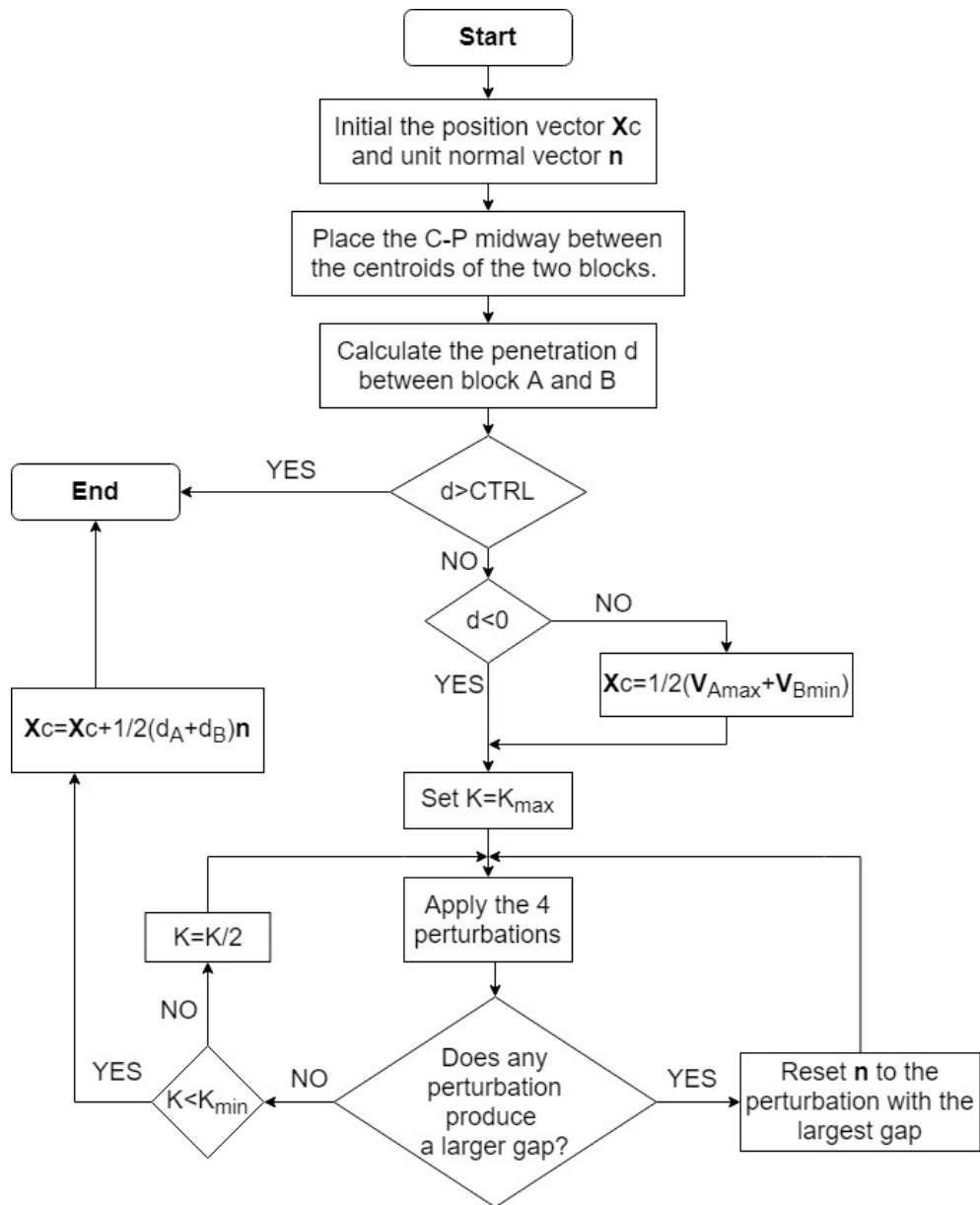


Figure 4.4: Flowchart of the Common-Plane Method

converted to vertex-to-face contact; (ii) the second type is the contact that can be converted to vertex-to-vertex contact. We can add or remove different springs based on the contact type to avoid penetration.

4.4.2 Sub-matrix of normal spring stiffness

(i) Vertex-to-face contact

As shown in Figure 4.5, assume that vertex P_1 of block i penetrates into the face $P_2P_3P_4$ and stops at P_0 in block j . The face $P_2P_3P_4$ can be considered as the entrance face, the position and displacement increment of vertex P_i are (x_i, y_i, z_i) and (u_i, v_i, w_i) , $i = 1, 2, 3, 4$, respectively. If the vertex P_1 passes the entrance face $P_2P_3P_4$, a normal spring stiffness k_n is introduced to push back the vertex to the entrance face along the shortest distance d_n . The potential energy contributed due to the normal contact spring represents as:

$$\Pi_{nc} = \frac{k_n}{2} d_n^2 \quad (4.53)$$

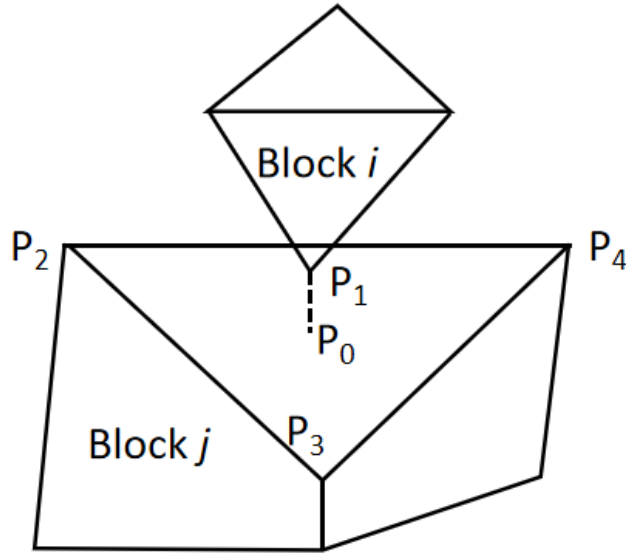


Figure 4.5: Contact between vertex and face, P_1 is the penetrate vertex, and $P_2P_3P_4$ is the entrance face.

On the face $P_2P_3P_4$, vertices P_2, P_3, P_4 are in counter-clockwise sequence. We use P'_i to represent the final position of P_i at the end of the time step. The shortest

distance d_n from P_1' to face $P_2'P_3'P_4'$ denotes:

$$d_n = \frac{[\overrightarrow{P_1'P_2'} \cdot (\overrightarrow{P_2'P_3'} \times \overrightarrow{P_2'P_4'})]}{|\overrightarrow{P_2'P_3'} \times \overrightarrow{P_2'P_4'}|} = \frac{\Delta}{A} \quad (4.54)$$

where

$$\begin{aligned} A &= \left| \overrightarrow{P_2'P_3'} \times \overrightarrow{P_2'P_4'} \right| \\ &= \begin{vmatrix} i & j & k \\ x_3 + u_3 - x_2 - u_2 & y_3 + v_3 - y_2 - v_2 & z_3 + w_3 - z_2 - w_2 \\ x_4 + u_4 - x_2 - u_2 & y_4 + v_4 - y_2 - v_2 & z_4 + w_4 - z_2 - w_2 \end{vmatrix} \\ &\approx \sqrt{\begin{aligned} &[(y_3 - y_2)(z_4 - z_2) - (y_4 - y_2)(z_3 - z_2)]^2 \\ &+ [(z_3 - z_2)(x_4 - x_2) - (x_3 - x_2)(z_4 - z_2)]^2 \\ &+ [(x_3 - x_2)(y_4 - y_2) - (x_4 - x_2)(y_3 - y_2)]^2 \end{aligned}} \end{aligned} \quad (4.55)$$

and,

$$\begin{aligned} \Delta &= \begin{vmatrix} 1 & x_1 + u_1 & y_1 + v_1 & z_1 + w_1 \\ 1 & x_2 + u_2 & y_2 + v_2 & z_2 + w_2 \\ 1 & x_3 + u_3 & y_3 + v_3 & z_3 + w_3 \\ 1 & x_4 + u_4 & y_4 + v_4 & z_4 + w_4 \end{vmatrix} \\ &\approx \begin{vmatrix} 1 & x_1 & y_1 & z_1 \\ 1 & x_2 & y_2 & z_2 \\ 1 & x_3 & y_3 & z_3 \\ 1 & x_4 & y_4 & z_4 \end{vmatrix} + \begin{vmatrix} 1 & u_1 & y_1 & z_1 \\ 1 & u_2 & y_2 & z_2 \\ 1 & u_3 & y_3 & z_3 \\ 1 & u_4 & y_4 & z_4 \end{vmatrix} \\ &+ \begin{vmatrix} 1 & x_1 & v_1 & z_1 \\ 1 & x_2 & v_2 & z_2 \\ 1 & x_3 & v_3 & z_3 \\ 1 & x_4 & v_4 & z_4 \end{vmatrix} + \begin{vmatrix} 1 & x_1 & y_1 & w_1 \\ 1 & x_2 & y_2 & w_2 \\ 1 & x_3 & y_3 & w_3 \\ 1 & x_4 & y_4 & w_4 \end{vmatrix} \end{aligned} \quad (4.56)$$

It should be noted that the high-order terms has been ignored in the Equation (4.56) due to the displacements (u_i, v_i, w_i) , $i = 1, 2, 3, 4$ in each time step are very small [97]. Let,

$$S_0 = \begin{vmatrix} 1 & x_1 & y_1 & z_1 \\ 1 & x_2 & y_2 & z_2 \\ 1 & x_3 & y_3 & z_3 \\ 1 & x_4 & y_4 & z_4 \end{vmatrix} \quad (4.57)$$

Then, Equation (4.56) can be written as:

$$\begin{aligned} \Delta = S_0 + & \begin{pmatrix} a_1 \\ b_1 \\ c_1 \end{pmatrix}^T \begin{pmatrix} u_1 \\ v_1 \\ w_1 \end{pmatrix} + \begin{pmatrix} a_2 \\ b_2 \\ c_2 \end{pmatrix}^T \begin{pmatrix} u_2 \\ v_2 \\ w_2 \end{pmatrix} \\ & + \begin{pmatrix} a_3 \\ b_3 \\ c_3 \end{pmatrix}^T \begin{pmatrix} u_3 \\ v_3 \\ w_3 \end{pmatrix} + \begin{pmatrix} a_4 \\ b_4 \\ c_4 \end{pmatrix}^T \begin{pmatrix} u_4 \\ v_4 \\ w_4 \end{pmatrix} \end{aligned} \quad (4.58)$$

where

$$\begin{aligned} a_1 &= (y_4 - y_2)(z_3 - z_2) - (y_3 - y_2)(z_4 - z_2) \\ a_2 &= (y_3 - y_1)(z_4 - z_1) - (y_4 - y_1)(z_3 - z_1) \\ b_1 &= (x_3 - x_2)(z_4 - z_2) - (x_4 - x_2)(z_3 - z_2) \\ b_2 &= (x_4 - x_1)(z_3 - z_1) - (x_3 - x_1)(z_4 - z_1) \\ c_1 &= (x_4 - x_2)(y_3 - y_2) - (x_3 - x_2)(y_4 - y_2) \\ c_2 &= (x_3 - x_1)(y_4 - y_1) - (x_4 - x_1)(y_3 - y_1) \\ a_3 &= (y_4 - y_1)(z_2 - z_1) - (y_2 - y_1)(z_4 - z_1) \\ a_4 &= (y_2 - y_1)(z_3 - z_1) - (y_3 - y_1)(z_2 - z_1) \\ b_3 &= (x_2 - x_1)(z_4 - z_1) - (x_4 - x_1)(z_2 - z_1) \\ b_4 &= (x_3 - x_1)(z_2 - z_1) - (x_2 - x_1)(z_3 - z_1) \\ c_3 &= (x_4 - x_1)(y_2 - y_1) - (x_2 - x_1)(y_4 - y_1) \\ c_4 &= (x_2 - x_1)(y_3 - y_1) - (x_3 - x_1)(y_2 - y_1) \end{aligned} \quad (4.59)$$

From Equations (4.10) and (4.56), d_n represents as:

$$d_n = \frac{S_0}{A} + \mathbf{D}_i^T \mathbf{E}_i + \mathbf{D}_j^T \mathbf{G}_j \quad (4.60)$$

where

$$\mathbf{E}_i^T = \frac{1}{A} (a_1 \quad b_1 \quad c_1) \mathbf{T}_i(x_1, y_1, z_1) \quad (4.61)$$

$$\begin{aligned} \mathbf{G}_j^T &= \frac{1}{A} (a_2 \quad b_2 \quad c_2) \mathbf{T}_j(x_2, y_2, z_2) \\ &+ \frac{1}{A} (a_3 \quad b_3 \quad c_3) \mathbf{T}_j(x_3, y_3, z_3) \\ &+ \frac{1}{A} (a_4 \quad b_4 \quad c_4) \mathbf{T}_j(x_4, y_4, z_4) \end{aligned} \quad (4.62)$$

Therefore, the potential energy of the normal contact spring (see Equation (4.53))

becomes:

$$\begin{aligned}
\Pi_{nc} &= \frac{k_n}{2} d_n^2 = \frac{k_n}{2} \left(\frac{S_0}{A} + \mathbf{D}_i^T \mathbf{E}_i + \mathbf{D}_j^T \mathbf{G}_j \right)^2 \\
&= \frac{k_n}{2} \left(\frac{S_0}{A} \right)^2 + \frac{k_n}{2} (\mathbf{D}_i^T \mathbf{E}_i \mathbf{E}_i^T \mathbf{D}_i + \mathbf{D}_j^T \mathbf{G}_j \mathbf{G}_j^T \mathbf{D}_j) \\
&\quad + k_n \frac{S_0}{A} (\mathbf{D}_i^T \mathbf{E}_i + \mathbf{D}_j^T \mathbf{G}_j) + k_n \mathbf{D}_i^T \mathbf{E}_i \mathbf{G}_j^T \mathbf{D}_j
\end{aligned} \tag{4.63}$$

Taking the derivative of Π_{nc} , four 12×12 sub-matrices and two 12×1 sub-matrices can be obtained, which are then added to the sub-matrices \mathbf{K}_{ii} , \mathbf{K}_{ij} , \mathbf{K}_{ji} , \mathbf{K}_{jj} , \mathbf{F}_i and \mathbf{F}_j of the global Equation (4.15), respectively.

- The derivative of Π_{nc} :

$$\mathbf{K}_{rs} = \frac{\partial^2 \Pi_{nc}}{\partial d_{ri} \partial d_{si}} = k_n \mathbf{E}_i \mathbf{E}_i^T \rightarrow \mathbf{K}_{ii} \quad r, s = 1, 2, 3 \dots 12 \tag{4.64}$$

is added to sub-matrix \mathbf{K}_{ii} .

- The derivative of Π_{nc} :

$$\mathbf{K}_{rs} = \frac{\partial^2 \Pi_{nc}}{\partial d_{ri} \partial d_{sj}} = k_n \mathbf{E}_i \mathbf{G}_j^T \rightarrow \mathbf{K}_{ij} \quad r, s = 1, 2, 3 \dots 12 \tag{4.65}$$

is added to sub-matrix \mathbf{K}_{ij} .

- The derivative of Π_{nc} :

$$\mathbf{K}_{rs} = \frac{\partial^2 \Pi_{nc}}{\partial d_{rj} \partial d_{si}} = k_n \mathbf{G}_j \mathbf{E}_i^T \rightarrow \mathbf{K}_{ji} \quad r, s = 1, 2, 3 \dots 12 \tag{4.66}$$

is added to sub-matrix \mathbf{K}_{ji} .

- The derivative of Π_{nc} :

$$\mathbf{K}_{rs} = \frac{\partial^2 \Pi_{nc}}{\partial d_{rj} \partial d_{sj}} = k_n \mathbf{G}_j \mathbf{G}_j^T \rightarrow \mathbf{K}_{jj} \quad r, s = 1, 2, 3 \dots 12 \tag{4.67}$$

- The derivative of Π_{nc} :

$$\mathbf{f}_r = -\frac{\partial \Pi_{nc}(0)}{\partial d_{ri}} = -k_n \frac{S_0}{A} \mathbf{E}_i \rightarrow \mathbf{F}_i \quad r = 1, 2, 3 \dots 12 \tag{4.68}$$

is added to sub-matrix \mathbf{F}_i .

- The derivative of Π_{nc} :

$$\mathbf{f}_r = -\frac{\partial \Pi_{nc}(0)}{\partial d_{rj}} = -k_n \frac{S_0}{A} \mathbf{G}_j \rightarrow \mathbf{F}_j \quad r = 1, 2, 3 \dots 12 \tag{4.69}$$

is added to sub-matrix F_j .

(ii) Vertex-to-vertex contact

Since the entrance face can not find in the second contact types, the common plane can be assumed as an entrance plane in the vertex-to-vertex, vertex-to-edge and edge-to-edge contacts. The unit normal vector of the common plane is expressed as (l_x, l_y, l_z) , which points to block i from block j . As shown in Figure 4.6, the P_1 on block i and P_2 on block j are the nearest points to the common plane, which is considered as the contact points. For the vertex-to-vertex contacts, the P_1 and P_2 are apparent. For the vertex-to-edge contact, the P_2 is considered as the projected point of point P_1 on the edge E_2 . For the edge-to-edge contacts, P_1 and P_2 are the intersection of line L with edge E_1 and E_2 , respectively, where the L is an orthogonal line to both edge E_1 and edge E_2 .

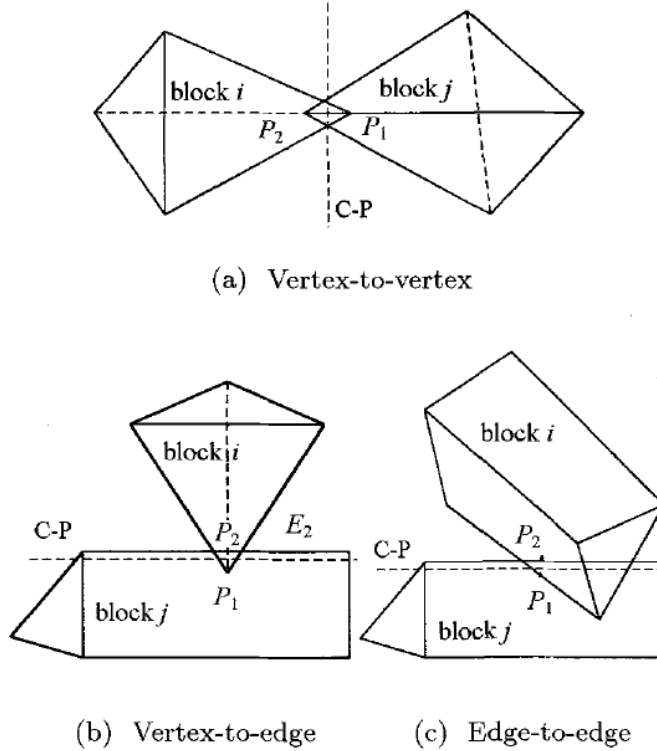


Figure 4.6: Contact types and CP position: (a) Vertex-to-vertex; (b) Vertex-to-edge; (c) Edge-to-edge

$$d_n = (l_x, l_y, l_z) \begin{pmatrix} x_2 + u_2 - (x_1 + u_1) \\ y_2 + v_2 - (y_1 + v_1) \\ z_2 + w_2 - (z_1 + w_1) \end{pmatrix} \quad (4.70)$$

$$d_n = \delta - D_i^T E_i + D_j^T G_j \quad (4.71)$$

where

$$\delta = (l_x, l_y, l_z) \begin{pmatrix} x_2 - x_1 \\ y_2 - y_1 \\ z_2 - z_1 \end{pmatrix} \quad (4.72)$$

$$\mathbf{E}_i^T = (l_x, l_y, l_z) \mathbf{T}_i(x_1, y_1, z_1) \quad (4.73)$$

$$\mathbf{G}_j^T = (l_x, l_y, l_z) \mathbf{T}_j(x_2, y_2, z_2) \quad (4.74)$$

Taking the derivative of Π_{nc} as the Equations (4.64)-(4.69), four 12×12 sub-matrices and two 12×1 sub-matrices can be obtained, which are then added to the sub-matrices \mathbf{K}_{ii} , \mathbf{K}_{ij} , \mathbf{K}_{ji} , \mathbf{K}_{jj} , \mathbf{F}_i and \mathbf{F}_j of the global Equation (4.15), respectively, as shown below:

$$\begin{aligned} k_n \mathbf{E}_i \mathbf{E}_i^T &\rightarrow \mathbf{K}_{ii} \\ -k_n \mathbf{E}_i \mathbf{G}_j^T &\rightarrow \mathbf{K}_{ij} \\ -k_n \mathbf{G}_j \mathbf{E}_i^T &\rightarrow \mathbf{K}_{ji} \\ k_n \mathbf{G}_j \mathbf{G}_j^T &\rightarrow \mathbf{K}_{jj} \\ k_n \delta \mathbf{E}_i &\rightarrow \mathbf{F}_i \\ -k_n \delta \mathbf{G}_j &\rightarrow \mathbf{F}_j \end{aligned} \quad (4.75)$$

4.4.3 Sub-matrix of shear spring stiffness

When the contact vertex and the entrance face are in the "non-sliding" mode, in addition to the normal spring, a shear spring is also used to obtain the "lock" mode. Assuming that P_0 is the projection of P_1 to entrance face $P_2P_3P_4$, which is considered as the contact point, and the vertex P_1 and P_0 move to the new location P'_1 and P'_0 after the loading is applied. The sliding distance d_τ is along the vector \vec{L} that is the projection of $\vec{P'_0P'_1}$ to the entrance face $P_2P_3P_4$.

$$d_\tau = \sqrt{|\vec{P'_0P'_1}|^2 - d_n^2} \quad (4.76)$$

The potential energy contributed due to the shear spring is given by:

$$\begin{aligned} \Pi_\tau &= \frac{k_s}{2} d_\tau^2 = \frac{k_s}{2} \left(|\vec{P'_0P'_1}|^2 - d_n^2 \right) \\ &= \frac{k_s}{2} \begin{pmatrix} x_1 + u_1 - x_0 - u_0 \\ y_1 + v_1 - y_0 - v_0 \\ z_1 + w_1 - z_0 - w_0 \end{pmatrix}^T \begin{pmatrix} x_1 + u_1 - x_0 - u_0 \\ y_1 + v_1 - y_0 - v_0 \\ z_1 + w_1 - z_0 - w_0 \end{pmatrix} - \frac{k_s}{2} d_n^2 \end{aligned} \quad (4.77)$$

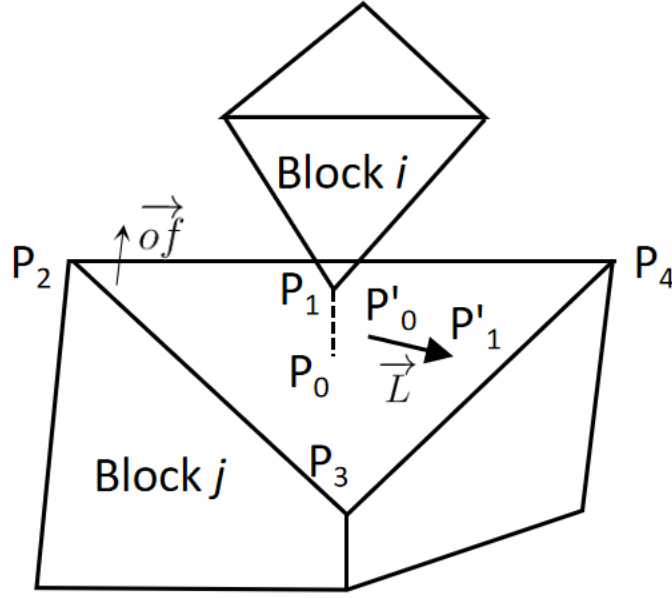


Figure 4.7: Contact vertex and the entrance face, and the position of shear spring

From Equations (4.71) and (4.77), we can get:

$$\Pi_\tau = \frac{k_s}{2} \left(\left[\begin{array}{ccc} x_1 - x_0 & y_1 - y_0 & z_1 - z_0 \end{array} \right] + \mathbf{D}_i^T \mathbf{T}_i^T - \mathbf{D}_j^T \mathbf{T}_j^T \right) \left(\left[\begin{array}{c} x_1 - x_0 \\ y_1 - y_0 \\ z_1 - z_0 \end{array} \right] + \mathbf{T}_i \mathbf{D}_i - \mathbf{T}_j \mathbf{D}_j \right) - \frac{k_s}{2} \left(\frac{S_0}{A} + \mathbf{D}_i^T \mathbf{E}_i + \mathbf{D}_j^T \mathbf{G}_j \right)^2 \quad (4.78)$$

Taking the derivative of Π_τ , four 12×12 sub-matrices and two 12×1 sub-matrices can be obtained, which are then added to the sub-matrices \mathbf{K}_{ii} , \mathbf{K}_{ij} , \mathbf{K}_{ji} , \mathbf{K}_{jj} , \mathbf{F}_i and \mathbf{F}_j of the global Equation (4.15), respectively.

- The derivative of Π_τ :

$$\begin{aligned} \mathbf{k}_{rs} &= \frac{\partial^2 \Pi_\tau}{\partial d_{ri} \partial d_{si}} \\ &= k_s \mathbf{T}_i^T \mathbf{T}_i - k_s \mathbf{E}_i^T \mathbf{E}_i \rightarrow \mathbf{K}_{ii} \end{aligned} \quad (4.79)$$

which is a 12×12 sub-matrix and added to \mathbf{K}_{ii} of the global Equation (4.15).

- The derivative of Π_τ :

$$\begin{aligned} \mathbf{k}_{rs} &= \frac{\partial^2 \Pi_\tau}{\partial d_{ri} \partial d_{sj}} \\ &= -k_s \mathbf{T}_i^T \mathbf{T}_j - k_s \mathbf{E}_i^T \mathbf{G}_j \rightarrow \mathbf{K}_{ij} \end{aligned} \quad (4.80)$$

which is a 12×12 sub-matrix and added to \mathbf{K}_{ij} of the global Equation (4.15).

- The derivative of Π_τ :

$$\begin{aligned} \mathbf{k}_{rs} &= \frac{\partial^2 \Pi_\tau}{\partial d_{rj} \partial d_{si}} \\ &= -k_s \mathbf{T}_j^T \mathbf{T}_i - k_s \mathbf{G}_j^T \mathbf{E}_i \rightarrow \mathbf{K}_{ji} \end{aligned} \quad (4.81)$$

which is a 12×12 sub-matrix and added to \mathbf{K}_{ji} of the global Equation (4.15).

- The derivative of Π_τ :

$$\begin{aligned} \mathbf{k}_{rs} &= \frac{\partial^2 \Pi_\tau}{\partial d_{rj} \partial d_{sj}} \\ &= k_s \mathbf{T}_j^T \mathbf{T}_j - k_s \mathbf{G}_j^T \mathbf{G}_j \rightarrow \mathbf{K}_{jj} \end{aligned} \quad (4.82)$$

which is a 12×12 sub-matrix and added to \mathbf{K}_{jj} of the global Equation (4.15).

- The derivative of the potential energy Π_τ of the force at P_0 on block i is:

$$\begin{aligned} \mathbf{f}_r &= -\frac{\partial \Pi_\tau(0)}{\partial d_{ri}} \\ &= -k_s \mathbf{T}_i^T \begin{pmatrix} x_1 - x_0 \\ y_1 - y_0 \\ z_1 - z_0 \end{pmatrix} + \frac{k_s S_0}{A} \mathbf{E}_i^T \rightarrow \mathbf{F}_i \end{aligned} \quad (4.83)$$

which is a 12×1 sub-matrix and added to \mathbf{F}_i of the global Equation (4.15).

- The derivative of the potential energy Π_τ of the force at P_0 on block j is:

$$\begin{aligned} \mathbf{f}_r &= \frac{\partial \Pi_\tau(0)}{\partial d_{rj}} \\ &= -k_s \mathbf{T}_j^T \begin{pmatrix} x_1 - x_0 \\ y_1 - y_0 \\ z_1 - z_0 \end{pmatrix} + \frac{k_s S_0}{A} \mathbf{G}_j^T \rightarrow \mathbf{F}_j \end{aligned} \quad (4.84)$$

which is a 12×1 sub-matrix and added to \mathbf{F}_j of the global Equation (4.15).

For the second contact types (see Figure 4.6), the contact points are P_1 of block i and P_2 of block j . The potential energy of the shear spring is:

$$\begin{aligned} \Pi_\tau &= \frac{k_s}{2} d_\tau^2 = \frac{k_s}{2} \left(\left| \overrightarrow{P_2'P_1'} \right|^2 - d_n^2 \right) \\ &= \frac{k_s}{2} \begin{pmatrix} x_1 + u_1 - x_2 - u_2 \\ y_1 + v_1 - y_2 - v_2 \\ z_1 + w_1 - z_2 - w_2 \end{pmatrix}^T \begin{pmatrix} x_1 + u_1 - x_2 - u_2 \\ y_1 + v_1 - y_2 - v_2 \\ z_1 + w_1 - z_2 - w_2 \end{pmatrix} - \frac{k_s}{2} d_n^2 \end{aligned} \quad (4.85)$$

Taking the derivative of Π_τ as the Equations (4.79)-(4.84), four 12×12 sub-matrices and two 12×1 sub-matrices can be obtained, which are then added to the sub-matrices \mathbf{K}_{ii} , \mathbf{K}_{ij} , \mathbf{K}_{ji} , \mathbf{K}_{jj} , \mathbf{F}_i and \mathbf{F}_j of the global Equation (4.15), respectively, as shown below:

$$\begin{aligned}
& k_s \mathbf{T}_i^T \mathbf{T}_i - k_s \mathbf{E}_i^T \mathbf{E}_i \rightarrow \mathbf{K}_{ii} \\
& -k_s \mathbf{T}_i^T \mathbf{T}_j + k_s \mathbf{E}_i^T \mathbf{G}_j \rightarrow \mathbf{K}_{ij} \\
& -k_s \mathbf{T}_j^T \mathbf{T}_i + k_s \mathbf{G}_j^T \mathbf{E}_i \rightarrow \mathbf{K}_{ji} \\
& k_s \mathbf{T}_j^T \mathbf{T}_j - k_s \mathbf{G}_j^T \mathbf{G}_j \rightarrow \mathbf{K}_{jj} \\
& -k_s \mathbf{T}_i^T \begin{pmatrix} x_1 - x_2 \\ y_1 - y_2 \\ z_1 - z_2 \end{pmatrix} - k_s \delta \mathbf{E}_i^T \rightarrow \mathbf{F}_i \\
& k_s \mathbf{T}_j^T \begin{pmatrix} x_1 - x_2 \\ y_1 - y_2 \\ z_1 - z_2 \end{pmatrix} + k_s \delta \mathbf{G}_j^T \rightarrow \mathbf{F}_j
\end{aligned} \tag{4.86}$$

where δ , \mathbf{E}_i and \mathbf{G}_j are same as shown in Equations (4.72)-(4.74).

4.4.4 Sub-matrix of friction spring stiffness

The frictional forces should be considered when the contact is at the sliding state [127]. For the sliding state, the normal spring and the friction spring need to be added. Based on Coulomb's law, the friction force is:

$$F_f = k_n |d_n| \tan(\phi) + C_f \tag{4.87}$$

where k_n is the normal spring stiffness, d_n is the normal penetration distance, $\tan(\phi)$ is the friction coefficient in which ϕ is the friction angle, and C_f is the cohesion.

The frictional force direction \vec{L} is the projection of $\overrightarrow{P'_0 P'_1}$ on face $P_2 P_3 P_4$ (see Figure 4.7).

$$\overrightarrow{P'_0 P'_1} = (x_1 + u'_1 - x_0 - u'_0) \vec{i} + (y_1 + v'_1 - y_0 - v'_0) \vec{j} + (z_1 + w'_1 - z_0 - w'_0) \vec{k} \tag{4.88}$$

The unit normal vector $\vec{o\hat{f}}$ of face $P_2P_3P_4$ can be obtained by:

$$\begin{aligned} \vec{o\hat{f}} = \frac{1}{A} \left\{ [(y_3 - y_2)(z_4 - z_2) - (y_4 - y_2)(z_3 - z_2)] \vec{i} \right. \\ + [(z_3 - z_2)(x_4 - x_2) - (x_3 - x_2)(z_4 - z_2)] \vec{j} \\ \left. + [(x_3 - x_2)(y_4 - y_2) - (x_4 - x_2)(y_3 - y_2)] \vec{k} \right\} \end{aligned} \quad (4.89)$$

where the A can be calculated by Equation (4.55). Then the \vec{L} and its value represent as:

$$\vec{L} = \overrightarrow{P'_0P'_1} + |d_n| \vec{o\hat{f}} = a\vec{i} + b\vec{j} + c\vec{k} \quad (4.90)$$

$$|\vec{L}| = \sqrt{|\overrightarrow{P'_0P'_1}|^2 - |d_n|^2} = d_\tau \quad (4.91)$$

where the d_n and d_τ are determined from the previous iteration, and

$$\begin{aligned} a &= (x_1 + u'_1 - x_0 - u'_0) - a_1 \frac{|dn|}{A} \\ b &= (y_1 + v'_1 - y_0 - v'_0) - b_1 \frac{|dn|}{A} \\ c &= (z_1 + w'_1 - z_0 - w'_0) - c_1 \frac{|dn|}{A} \end{aligned} \quad (4.92)$$

where a_1, b_1, c_1 are the same as Equation (4.59).

The potential energy Π_{fi} contributed by frictional force F_f at P_1 of block i is:

$$\begin{aligned} \Pi_{fi} &= \frac{F_f}{|\vec{L}|} (u_1 \quad v_1 \quad w_1) \begin{pmatrix} a \\ b \\ c \end{pmatrix} \\ &= \frac{F_f}{d_\tau} \mathbf{D}_i^T \mathbf{T}_i^T \begin{pmatrix} a \\ b \\ c \end{pmatrix} \\ &= F_f \mathbf{D}_i^T \mathbf{E}_i \end{aligned} \quad (4.93)$$

where

$$\mathbf{E}_i = \frac{1}{d_\tau} \mathbf{T}_i^T \begin{pmatrix} a \\ b \\ c \end{pmatrix} \quad (4.94)$$

Based on the minimization of potential energy, the derivative of Π_{fi} at zero displacement position can be calculated and added to \mathbf{F}_i in the global Equation (4.15).

$$\mathbf{f}_r = -\frac{\partial \Pi_{fi}(0)}{\partial d_{ri}} = -F_f \mathbf{E}_i \rightarrow \mathbf{F}_i \quad (4.95)$$

where $r=1,2,3,\dots,12$.

The potential energy Π_{fj} contributed by frictional force F_f at P_1 of block i is:

$$\begin{aligned}\Pi_{fj} &= -\frac{F_f}{|\vec{L}|} (u_1 \quad v_1 \quad w_1) \begin{pmatrix} a \\ b \\ c \end{pmatrix} \\ &= -\frac{F_f}{d\tau} \mathbf{D}_j^T \mathbf{T}_j^T \begin{pmatrix} a \\ b \\ c \end{pmatrix} \\ &= -F_f \mathbf{D}_j^T \mathbf{G}_j\end{aligned}\tag{4.96}$$

The derivative of Π_{fj} at zero displacement position can be calculated added to \mathbf{F}_j in the global Equation (4.15).

$$\mathbf{f}_r = -\frac{\partial \Pi_{fj}(0)}{\partial d_{rj}} = F_f \mathbf{G}_j \rightarrow \mathbf{F}_j\tag{4.97}$$

where $r=1,2,3,\dots,12$, and

$$\mathbf{G}_j = \frac{1}{d_\tau} \mathbf{T}_j^T \begin{pmatrix} a \\ b \\ c \end{pmatrix}\tag{4.98}$$

4.4.5 Open-close iterations

Each contact has three possible states: open, sliding and lock. These states can be determined by relationships between normal component F_n and shear component F_s based on the Mohr-Coulomb law.

(1) Open state

Condition: when the normal component F_n of contact force is tensile:

$$F_n = -k_n d_n \leq 0\tag{4.99}$$

where $d_n < 0$ means penetration occurs.

Operation: no normal and shear spring should be added.

(2) Sliding state

Condition: when the normal component F_n is compressive, and the shear compo-

ment F_s along the entrance face is sufficiently large:

$$\begin{aligned} F_n &> 0; \\ F_s &\geq F_n \tan\phi + C_f \end{aligned} \quad (4.100)$$

Operation: apply a normal spring and a pair of friction force.

(3) Lock state

Condition: when the normal component F_n is compressive, and the shear component F_s smaller than the friction force calculated by the Coulomb law.

$$\begin{aligned} F_n &> 0; \\ F_s &\leq F_n \tan\phi + C_f \end{aligned} \quad (4.101)$$

Operation: apply a normal and shear spring at the contact point.

In each time step, the global equilibrium equation should be solved iteratively to determine the lock position. In each time step, the global equilibrium equation should be solved iteratively to determine the lock position, and the stiff spring and friction force should be applied or removed according to the contact state change condition (see Table. 4.2), which is the called open-close iteration process [128], as shown in Figure 4.8.

Table 4.2: Criteria for contact mode change

Mode change	Condition	Operation
Open→open	$d_n > 0$	No change
Open→sliding	$d_n < 0;$ $d_\tau > \frac{k_n}{k_s} d_n \tan\phi + \frac{C_f}{k_s}$	Apply a normal spring and a pair of friction force
Open→lock	$d_n < 0;$ $d_\tau < \frac{k_n}{k_s} d_n \tan\phi + \frac{C_f}{k_s}$	Apply a normal and shear spring
Sliding→open	$d_n > 0$	Remove a normal spring and a pair of friction force
Sliding→sliding	$d_n < 0;$ $d_\tau \geq \text{TOL}$	No change
Sliding→lock	$d_n < 0;$ $d_\tau \leq \text{TOL}$	Remove the pair of friction forces and apply a shear spring
Lock→open	$d_n > 0$	Remove the normal and shear springs
Lock→sliding	$d_n < 0;$ $d_\tau > \frac{k_n}{k_s} d_n \tan\phi + \frac{C_f}{k_s}$	Remove the shear spring and apply a pair of friction forces
Lock→lock	$d_n < 0;$ $d_\tau < \frac{k_n}{k_s} d_n \tan\phi + \frac{C_f}{k_s}$	No change

where d_n and d_τ are the normal and shear displacements, calculated by the last iteration. $TOL=0.1 \text{ mm}$ is a given limit value.

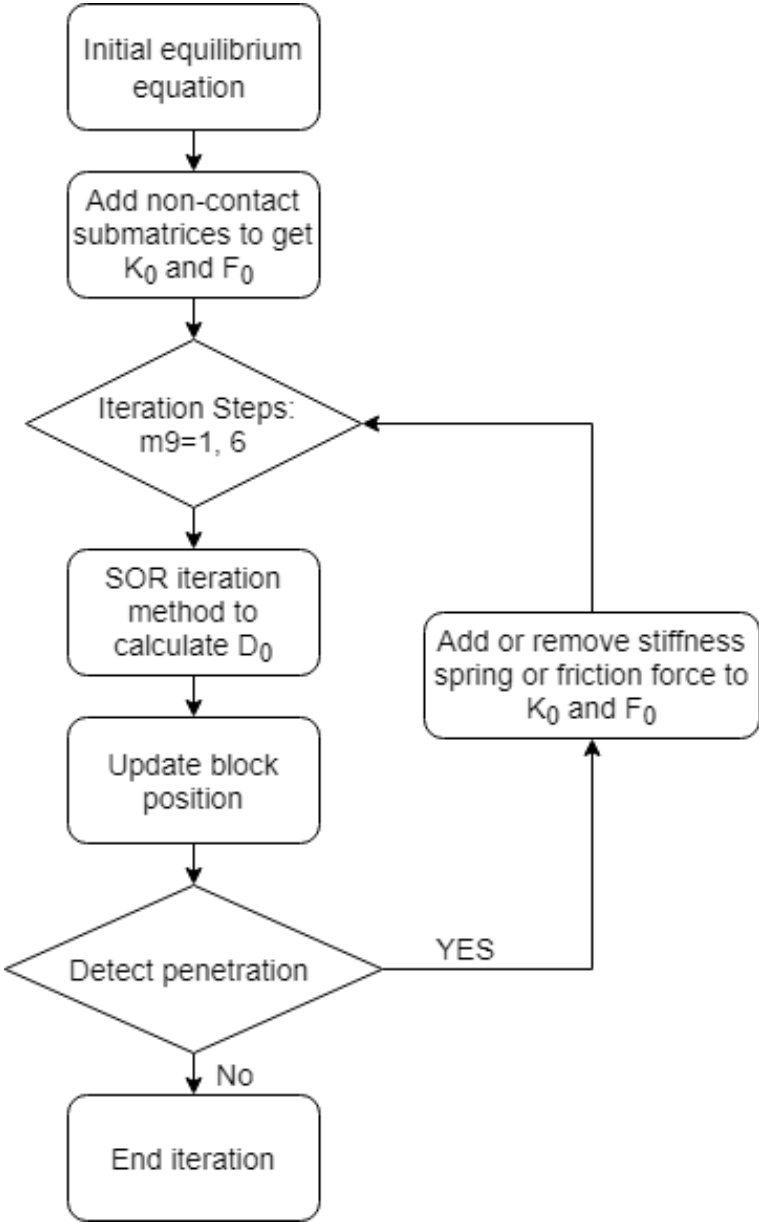


Figure 4.8: Flowchart of open-close iteration

4.5 Simplex integration for 3D-DDA

2D and 3D simplex integration methods were proposed by G-H Shi [88, 100], used to calculate the volume and centroid of 2D polygon and 3D polyhedron blocks [129]. This method is easy to program and saves calculation consumption.

Assume the vertex list of the i -th plane loop is arranged anticlockwise, as shown in Figure 4.9. The index and coordinate of a 3D block are:

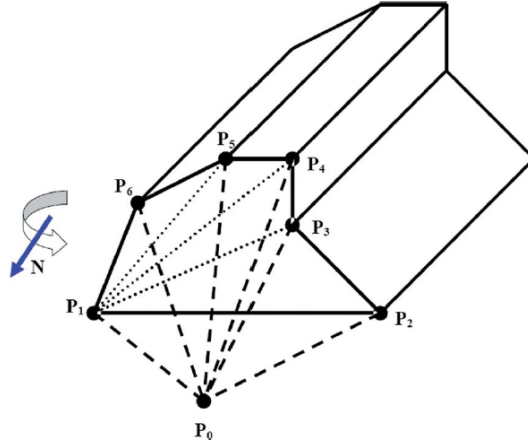


Figure 4.9: Creating oriented simplexes on a face [100].

$$P_1^{[i]} P_2^{[i]} P_3^{[i]} \dots P_{n(i)}^{[i]} \quad (4.102)$$

where $i = 1, 2, 3 \dots, s$ represent all surface polygons of the block in turn, and the s is the total number of polygons of the block.

$$P_j^{[i]} = \left(x_j^{[i]}, y_j^{[i]}, z_j^{[i]} \right) \quad (4.103)$$

where $j = 1, 2, 3 \dots, n(i) - 1$ represent the vertex of the face i . Set $P_0 = (0, 0, 0)$, the volume V (positive or negative) of the 3D block is:

$$\begin{aligned} V &= \sum_{i=1}^s \sum_{k=2}^{n(i)-1} \int_{p_0 p_1^{[i]} p_k^{[i]} p_{k+1}^{[i]}} 1D(x, y, z) \\ &= \frac{1}{6} \sum_{i=1}^s \sum_{k=2}^{n(i)-1} \begin{vmatrix} x_1^{[i]} & y_1^{[i]} & z_1^{[i]} \\ x_k^{[i]} & y_k^{[i]} & z_k^{[i]} \\ x_{k+1}^{[i]} & y_{k+1}^{[i]} & z_{k+1}^{[i]} \end{vmatrix} \end{aligned} \quad (4.104)$$

Through simplex integral calculation, the integrals of $1, x, y, z, x^2, y^2, z^2, xy, yz,$

xz are represented by the coordinates of the vertices of the 3D polyhedrons.

$$|V| = \iiint_{\Omega} dx dy dz = \text{sign}(V) \int_{\Omega} 1 D(x, y, z) \quad (4.105)$$

$$\begin{aligned} S_x &= \iiint_{\Omega} x dx dy dz = \text{sign}(V) \sum_{i=1}^s \sum_{k=2}^{n(i)-1} \int_{p_0 p_1^{[1/1]} p_k^{[i]} p_{k+1}^{[1]}} x D(x, y, z) \\ &= \frac{1}{24} \text{sign}(V) \sum_{i=1}^s \sum_{k=2}^{n(i)-1} \begin{vmatrix} x_1^{[i]} & y_1^{[i]} & z_1^{[i]} \\ x_k^{[i]} & y_k^{[i]} & z_k^{[i]} \\ x_{k+1}^{[i]} & y_{k+1}^{[i]} & z_{k+1}^{[i]} \end{vmatrix} (x_1 + x_k + x_{k+1}) \end{aligned} \quad (4.106)$$

$$S_y = \iiint_{\Omega} y dx dy dz = \frac{1}{24} \text{sign}(V) \sum_{i=1}^s \sum_{k=2}^{n(i)-1} \begin{vmatrix} x_1^{[i]} & y_1^{[i]} & z_1^{[i]} \\ x_k^{[i]} & y_k^{[i]} & z_k^{[i]} \\ x_{k+1}^{[i]} & y_{k+1}^{[i]} & z_{k+1}^{[i]} \end{vmatrix} (y_1 + y_k + y_{k+1}) \quad (4.107)$$

$$S_z = \iiint_{\Omega} z dx dy dz = \frac{1}{24} \text{sign}(V) \sum_{i=1}^s \sum_{k=2}^{n(i)-1} \begin{vmatrix} x_1^{[i]} & y_1^{[i]} & z_1^{[i]} \\ x_k^{[i]} & y_k^{[i]} & z_k^{[i]} \\ x_{k+1}^{[i]} & y_{k+1}^{[i]} & z_{k+1}^{[i]} \end{vmatrix} (z_1 + z_k + z_{k+1}) \quad (4.108)$$

$$\begin{aligned} S_{x^2} &= \iiint_{\Omega} x^2 dx dy dz = \text{sign}(V) \sum_{i=1}^s \sum_{k=2}^{n(i)-1} \int_{p_0 p_1^{[i]} p_k^{[i]} p_{k+1}^{[i]}} x^2 D(x, y, z) \\ &= \frac{1}{60} \text{sign}(V) \sum_{i=1}^s \sum_{k=2}^{n(i)-1} \begin{vmatrix} x_1^{[i]} & y_1^{[i]} & z_1^{[i]} \\ x_k^{[i]} & y_k^{[i]} & z_k^{[i]} \\ x_{k+1}^{[i]} & y_{k+1}^{[i]} & z_{k+1}^{[i]} \end{vmatrix} \\ &\quad \times (x_1^2 + x_k^2 + x_{k+1}^2 + x_1 x_k + x_1 x_{k+1} + x_k x_{k+1}) \end{aligned} \quad (4.109)$$

$$\begin{aligned} S_{y^2} &= \iiint_{\Omega} y^2 dx dy dz = \frac{1}{60} \text{sign}(V) \sum_{i=1}^s \sum_{k=2}^{n(i)-1} \begin{vmatrix} x_1^{[i]} & y_1^{[i]} & z_1^{[i]} \\ x_k^{[i]} & y_k^{[i]} & z_k^{[i]} \\ x_{k+1}^{[i]} & y_{k+1}^{[i]} & z_{k+1}^{[i]} \end{vmatrix} \\ &\quad \times (y_1^2 + y_k^2 + y_{k+1}^2 + y_1 y_k + y_1 y_{k+1} + y_k y_{k+1}) \end{aligned} \quad (4.110)$$

$$\begin{aligned} S_{z^2} &= \iiint_{\Omega} z^2 dx dy dz = \frac{1}{60} \text{sign}(V) \sum_{i=1}^s \sum_{k=2}^{n(i)-1} \begin{vmatrix} x_1^{[i]} & y_1^{[i]} & z_1^{[i]} \\ x_k^{[i]} & y_k^{[i]} & z_k^{[i]} \\ x_{k+1}^{[i]} & y_{k+1}^{[i]} & z_{k+1}^{[i]} \end{vmatrix} \\ &\quad \times (z_1^2 + z_k^2 + z_{k+1}^2 + z_1 z_k + z_1 z_{k+1} + z_k z_{k+1}) \end{aligned} \quad (4.111)$$

$$\begin{aligned}
S_{xy} &= \iiint_{\Omega} xy dx dy dz = \text{sign}(V) \sum_{i=1}^s \sum_{k=2}^{n(i)-1} \int_{p_0 p_1^{(i)} p_{k+1}^{[i]}} xy D(x, y, z) \\
&= \frac{1}{120} \text{sign}(V) \sum_{i=1}^s \sum_{k=2}^{n(i)-1} \begin{vmatrix} x_1^{[i]} & y_1^{[i]} & z_1^{[i]} \\ x_k^{[i]} & y_k^{[i]} & z_k^{[i]} \\ x_{k+1}^{[i]} & y_{k+1}^{[i]} & z_{k+1}^{[i]} \end{vmatrix} (2x_1 y_1 + x_1 y_k + x_1 y_{k+1} \\
&\quad + x_k y_1 + 2x_k y_k + x_k y_{k+1} + x_{k+1} y_1 + x_{k+1} y_k + 2x_{k+1} y_{k+1})
\end{aligned} \tag{4.112}$$

$$\begin{aligned}
S_{xz} &= \iiint_{\Omega} xz dx dy dz = \frac{1}{120} \text{sign}(V) \sum_{i=1}^s \sum_{k=2}^{n(i)-1} \begin{vmatrix} x_1^{[i]} & y_1^{[i]} & z_1^{[i]} \\ x_k^{[i]} & y_k^{[i]} & z_k^{[i]} \\ x_{k+1}^{[i]} & y_{k+1}^{[i]} & z_{k+1}^{[i]} \end{vmatrix} (2x_1 z_1 + x_1 z_k + x_1 z_{k+1} \\
&\quad + x_k z_1 + 2x_k z_k + x_k z_{k+1} + x_{k+1} z_1 + x_{k+1} z_k + 2x_{k+1} z_{k+1})
\end{aligned} \tag{4.113}$$

$$\begin{aligned}
S_{yz} &= \iiint_{\Omega} yz dx dy dz = \frac{1}{120} \text{sign}(V) \sum_{i=1}^s \sum_{k=2}^{n(i)-1} \begin{vmatrix} x_1^{[i]} & y_1^{[i]} & z_1^{[i]} \\ x_k^{[i]} & y_k^{[i]} & z_k^{[i]} \\ x_{k+1}^{[i]} & y_{k+1}^{[i]} & z_{k+1}^{[i]} \end{vmatrix} (2y_1 z_1 + y_1 z_k + y_1 z_{k+1} \\
&\quad + y_k z_1 + 2y_k z_k + y_k z_{k+1} + y_{k+1} z_1 + y_{k+1} z_k + 2y_{k+1} z_{k+1})
\end{aligned} \tag{4.114}$$

where $\text{sign}(V)$ is the symbolic function of the volume of the domain Ω , which represents the direction of the domain.

The centroid of the block can be calculated by:

$$x_0 = \frac{S_x}{V} \quad y_0 = \frac{S_y}{V} \quad z_0 = \frac{S_z}{V} \tag{4.115}$$

4.6 SOR iteration method

In the 3D-DDA, the Successive Over-Relaxation (SOR) method is used for solving the linear system of equations, resulting in faster convergence [130]. According to the global Equation (4.15), a square system of $12 \times n$ linear equations with unknown D is shown in Equation (4.116).

$$KD = F \tag{4.116}$$

Then K can be decomposed into a diagonal component χ , and strictly lower and upper triangular components \check{L} and \hat{R} :

$$K = \chi + \check{L} + \hat{R} \tag{4.117}$$

A relaxation factor ω is used for the linear equations, the Equation (4.116) can be written as:

$$(\boldsymbol{\chi} + \omega \check{\mathbf{L}})\mathbf{D} = \omega \mathbf{F} - [\omega \hat{\mathbf{R}} + (\omega - 1)\boldsymbol{\chi}] \quad (4.118)$$

where the constant $0 < \omega < 2$, which can guarantee the SOR solution convergence. The SOR method is an iterative technique that solves the left hand side of this expression for \mathbf{D} , using the previous value for \mathbf{D} on the right hand side. Analytically, this may be written as:

$$\mathbf{D}^{(k+1)} = (\boldsymbol{\chi} + \omega \check{\mathbf{L}})^{-1} \left(\omega \mathbf{F} - [\omega \hat{\mathbf{R}} + (\omega - 1)\boldsymbol{\chi}] \mathbf{D}^{(k)} \right) \quad (4.119)$$

where $\mathbf{D}^{(k)}$ is the k -th iteration of the \mathbf{D} . The $\mathbf{D}^{(k+1)}$ can be calculated sequentially by the forward substitution, which can be written as:

$$D_i^{(k+1)} = (1-\omega)D_i^{(k)} + \frac{\omega}{K_{ii}} \left(F_i - \sum_{j<i} K_{ij}D_j^{(k+1)} - \sum_{j>i} K_{ij}D_j^{(k)} \right), \quad i = 1, 2, \dots, n \quad (4.120)$$

4.7 Procedure for 3D-DDA program

A flowchart of procedures of the 3D-DDA code, including the sub-matrices, contact mechanics and open-close iterations, has been created as previously described, and is shown in Figure 4.10. Some details of those steps are introduced:

- (1) Input geometric data includes the coordinates of the vertexes and the order of the generated surface, the *obj* file format is used in this program. Furthermore, the loading, fixing and measuring points are input in this part. Input physical data includes the material parameters (unit mass, volume force, Young's modulus, and Poisson's ratio, etc) and computational parameters (time steps, contact stiffness and maximum allowed displacement, etc).
- (2) Detect the contact types is done by the CPM. The open-close iterations method is used to apply or remove normal, shear, or frictional springs based on the contact types.
- (3) Check the convergence should meet two conditions: No penetrations and no tension forces. If the conditions have not been met through the six-step open-close iteration or the displacement exceeds the defined limit, the time intervals need to be shortened.

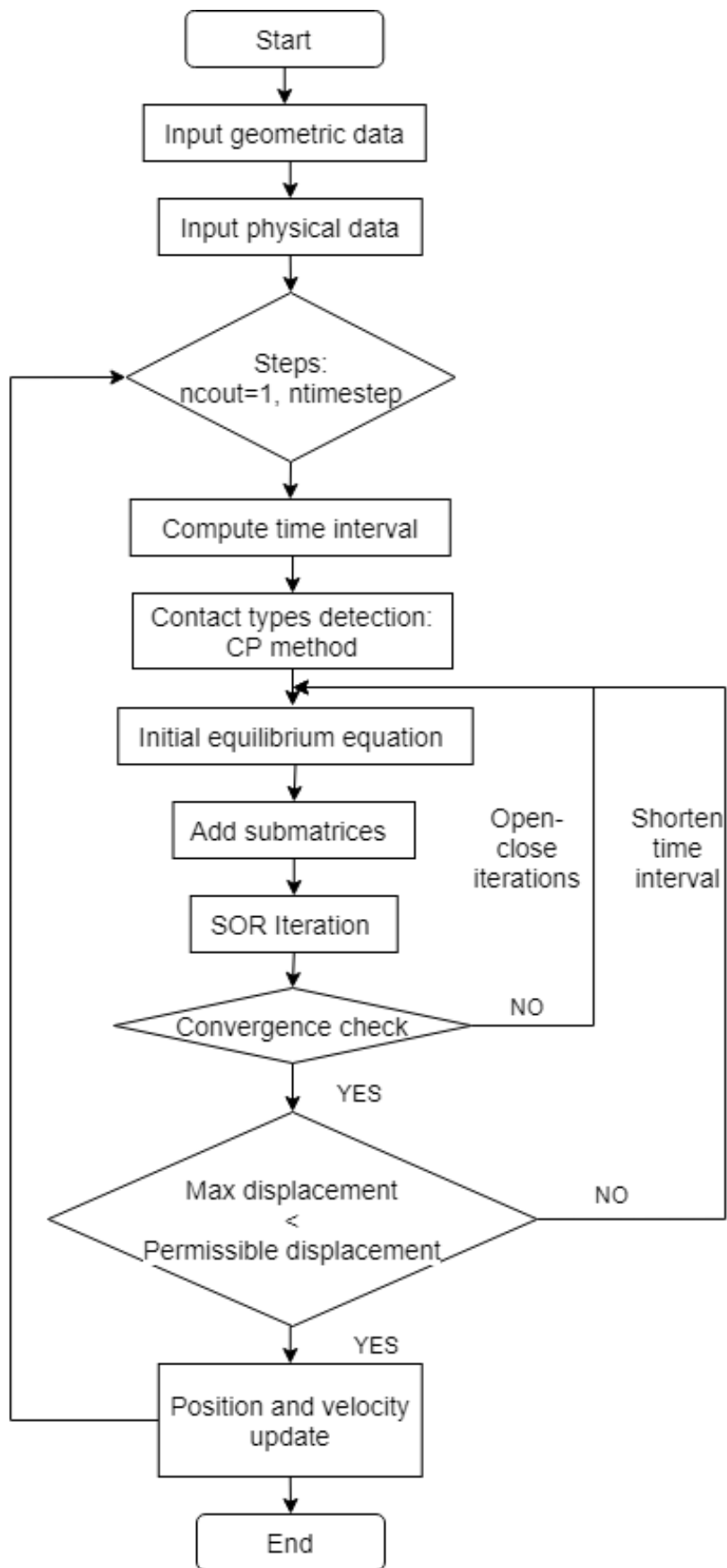


Figure 4.10: Flow chart of 3D-DDA procedure.

4.8 Concluding remarks

The mathematical formation of the 3D-DDA method was presented in this section, some new numerical technologies were used in programming:

- The CPM was used to detect the contact types, the calculation speed was greatly improved and the calculation consumption was saved by comparing the original direct method.
- The soft contact approach instead of the hard penalty method was used in this thesis to consider the normal and shear contact stiffness.
- The contact was divided in two types, which are vertex-to-face contact and vertex-to-vertex contact, corresponding normal and shear springs as well as frictional forces were added based on the contact type.
- During each time step, the global equilibrium equations were solved iteratively by the SOR method to determine the lock position.

With these improvements, this 3D-DDA code will be able to simulate more conditions for discontinuous mediums. And the simulation results can be greatly improved for better predictions of their physics.

2D-DDA results application to ballast flight in high speed railways

5.1 Introduction

In this chapter, a numerical model based on the 2D-DDA method is proposed to study the ballast flight caused by dropping snow / ice blocks in high-speed railways. The following aspects are emphasized:

- The validation of the proposed model is done by comparing the numerical results with the experimental results.
- The numerical results show that the velocity, shape and incident angle of snow / ice block play an important role in the ballast flight. The number and the maximum displacement of ballast particles increase as the train speed increases.
- The incident angle of ice block greatly affects the movement direction of ballast particles.
- The shape of the ice block affects the amount and extent of ballast flight.

5.2 Background

The phenomenon of ballast flight is one of the major problems in high speed ballasted track, which has resulted in major maintenance costs and safety concerns. Flying ballast particles may hit the rail, the train body or the passengers through stations. Furthermore, small particles of ballast may come to rest between the rail-head and the wheels of rail vehicles, which cause substantial local bending damage to the rail [131, 132]. The aerodynamic effect is commonly regarded as the main cause of ballast flight [133, 134]. However, as counted by Saat et al. [135], about 50% of ballast flight incidents occur in snow condition. This is because high-speed

trains run through snow zone and blow up the snow which sticks to the under-floor equipment and freezes rapidly into ice, then, the frozen snow and ice drops at high speeds from trains due to temperature changes, train vibration and heat from the brakes, causing the ballast to fly up [136, 137], as shown in Figure 5.1. The effects of ballast flight caused by dropping snow / ice may lead to serious catastrophic consequences due to the high initial velocity, large mass, and chain reaction of the falling snow / ice. snow / ice dropping and influencing factors of

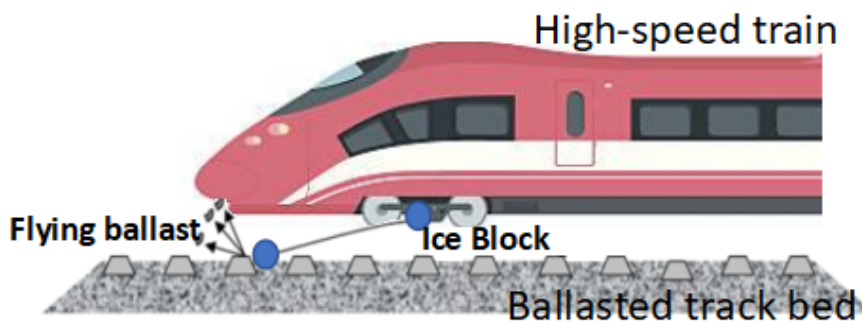


Figure 5.1: Schematic illustration of the mechanism and process of ballast flight caused by dropping ice block.

ballast flight have been studied in many recent studies. Lopenen et al. [136] studied the amount of the excitation required to drop snow from the train underframe. They used a simplified equilibrium equation based on the adhesive forces to indicate that the snow dropping requires an acceleration amplitude of approximately 20-2000 g depending on the characteristics of the snow mass. Kawashima *et al* et al. [137] carried out an experimental study using air cannon tests to investigate the ballast-flight phenomenon caused by the dropping of accreted ice, and gave a relationship between the number of flying ballast stones and the mass, shape, speed, and angle of the ice. Furthermore, computational fluid dynamics (CFD) methods have been applied to the study of the flow between the train underbody and the track bed around the bogie area and its impact on the ballast flight [138, 139, 140]. Xie *et al* [141] used a 3-D numerical model based on the coupling between Navier-Stokes equations based model and a discrete phase model to investigate the flow field in the presence of snow accumulation in the train underframe. The numerical result showed that the snow particles accumulated and moved on the train bogies by the high-speed air. However, to the best of our knowledge, there are no computational techniques focused on the dynamic impact behavior between the ice block and the ballasted track bed which is the key reason resulting in the ballast flight during winter. In this study, the discontinuous deformation analysis (DDA) method is used

to determine the displacement of irregular ballast particles and the collision between ice block and ballast particles. DDA is a kind of discrete element method (DEM), developed by G.-H Shi in 1989 for application of rock fracture mechanics and geotechnical or structural problems [9, 142]. Ishikawa et al. first used DDA for simulating deformation behavior of ballast [21], which showed good performance in the study of coarse granular materials.

The main purpose of this chapter is to determine the influence factors of ballast flight and to analyze the dynamic behavior of ballast particles during their collision with a snow / ice block. In the DDA method, the kinematic conditions of the contact surfaces are enforced through the penalty method in order to avoid the interpenetration between blocks. The performance of the ballast flight is evaluated by considering the velocity, the shape and the incident angle of snow / ice blocks. The numerical results show that these factors influence significantly the ballast particles dynamics and also their flight as well as the collision between ballast particles.

5.3 Validation: Dynamic behavior of ballast after collision.

In this first test, the dynamic behavior of ballasted track bed at the time of collision with an ice block was verified according to the air cannon experimental results by KawashimaI et al. [137]. The behavior of a $600 \text{ mm} \times 105 \text{ mm}$ ice block with a velocity of 80 km/h was simulated, and the computed results were compared with the experimental observations. The DDA simulations exhibited phenomenon of ballast flight similar to the ones observed experimentally, as shown in Figure 5.2. The number of ballast particles thrown 330 mm (distance from the ballast to the train underframe) or higher N_{330} for two different mass was calculated by the current DDA model. Due to the shape of the ice block in the air cannon test is cylindrical, its mass can be calculated by:

$$M_{ice} = \rho\pi\left(\frac{d}{2}\right)^2H \quad (5.1)$$

where $\rho = 0.9340 \times 10^{-6} \text{ kg/mm}^3$ is the density of ice [143], and $d = 105 \text{ mm}$ is the diameter of the cylinder. The mass of the ice block depends on the height of the ice cylinder H . The results from both experimental and numerical simulations showed that the number of the flying ballast particles increases as the velocity and the mass of ice block increase, as shown in Figure 5.3. The numerical results agree well with the experimental results.

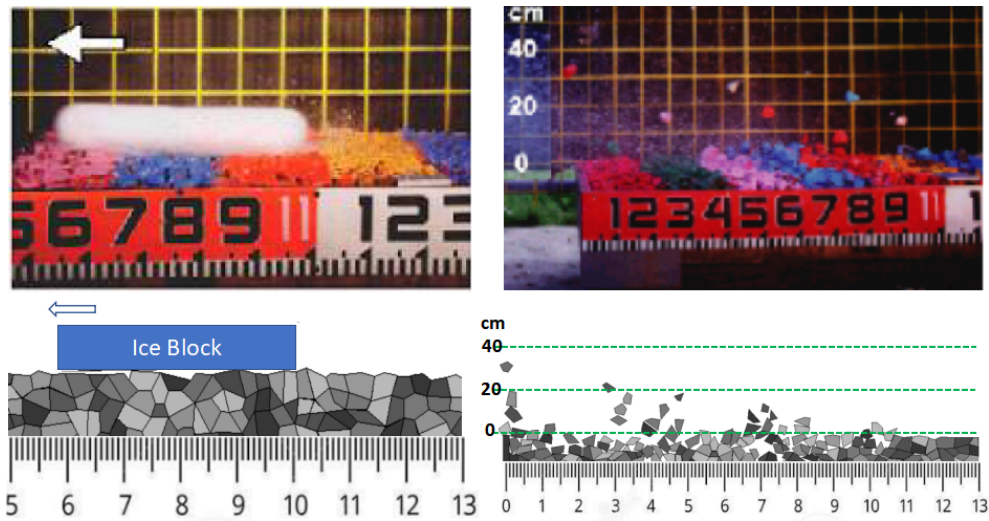


Figure 5.2: Comparison between the numerical and experimental responses [137] of the blocks for the DDA method.

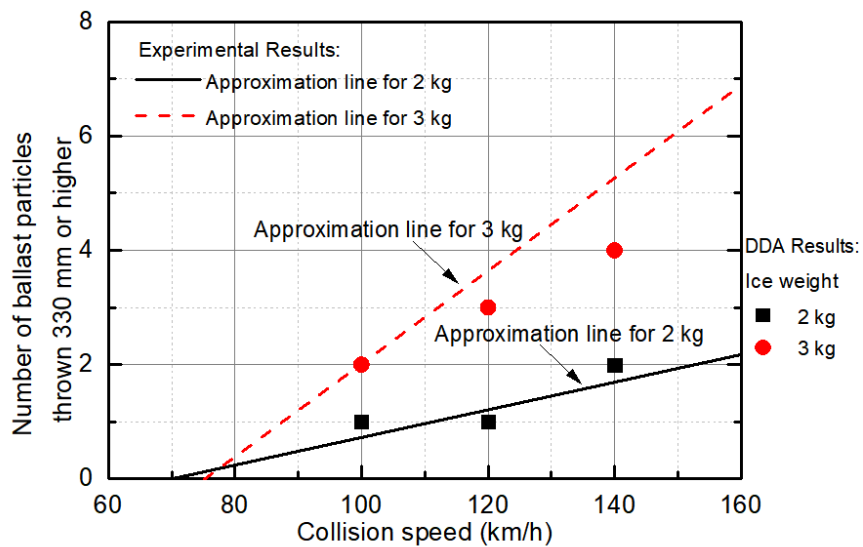


Figure 5.3: Comparison between the numerical and experimental values of N_{33} [137] for the DDA.

5.4 Simulation results

5.4.1 Velocity of ice block

5.4.1.1 Cross section

The ballast shoulder has a width of 500 *mm* and a height of 100 *mm*, whereas the ballast bed has a thickness of 350 *mm* (see Figure 5.4). Based on the European standard: *aggregates for railway ballast (13450, 2002)* [144], the gradation of ballast particles is from 31.5 *mm* to 63 *mm*, where the ballast particles have an irregular shape and are completely compacted. The ice block is assumed to be a circular shape with a diameter of 100 *mm*, which falls from a height of 600 *mm* on the ballast bed, where the falling distance is approximately equal to the height of the rail plus half of the height of the bogie. Adding the unit mass, elastic modulus, Poisson ratio, friction angle, etc. to the stiffness matrix in accordance to the physical characteristics of the ballast and the ice [143, 145], as shown in Table 5.1.

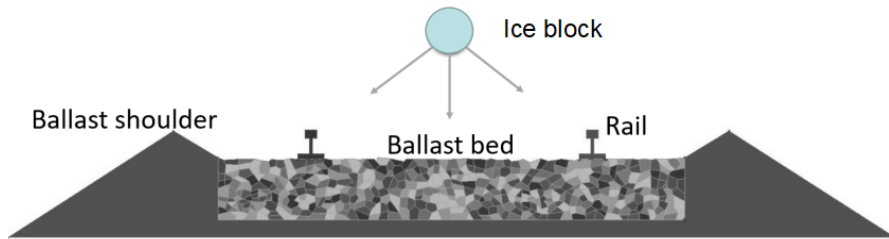


Figure 5.4: Track bed model

Table 5.1: The material parameters of ice and ballast

–	Unit mass	Elastic modulus	Poisson ratio	Friction angle
Ice	934 kg/m^3	10 GPa	0.06	–
Ballast	2600 kg/m^3	50 GPa	0.20	45°

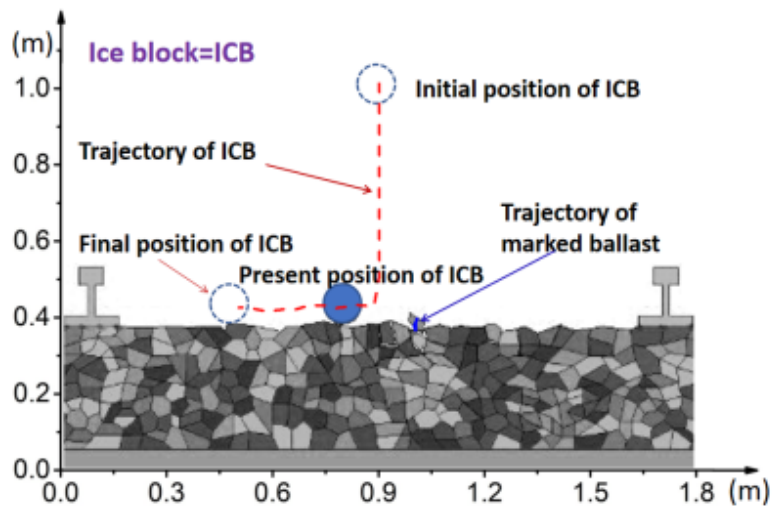
The initial vertical velocity is related to the falling location. In addition to the bogie position, ice and snow may also pack and fall off in the coupler pocket, on the top of the train, at the train connection, or even on the overhead contact system (OCS). The standard height of contact wire is 5.1 *m* from the top of the rail [146], and the vertical velocity of falling ice from OCS is about 10 *m/s*. Therefore, in the present numerical investigations, we used 0 *m/s*, 5 *m/s* and 10 *m/s* as initial vertical velocities. Overall, the simulation results presented below show that ballast flight

responses to increased velocity varied significantly. There are three key phenomena, are shown in Figure 5.5: (1) the movement trajectory of the ice block; (2) the evolution of the marked ballast displacement; and (3) the responses of the ballast bed. The phenomenon shows that the ice block after the collision first rebounded and then rolled. The displacement of ice block increases with the initial vertical velocity. When the vertical velocity exceeds 5 m/s , the ice block hits the rail, or even bounce and a secondary strike on the track bed happens when the velocity is more than 10 m/s . For the ballast after the collision, the higher the initial vertical velocity, the higher rebound of marked ballast is ejected, the severity of ballast bed responses is generated, and the greater the number of ballast particles is ejected. From Figure 5.6, we can get the same results, the number of flying ballasts and flying height of the ballast increase with the initial vertical velocity.

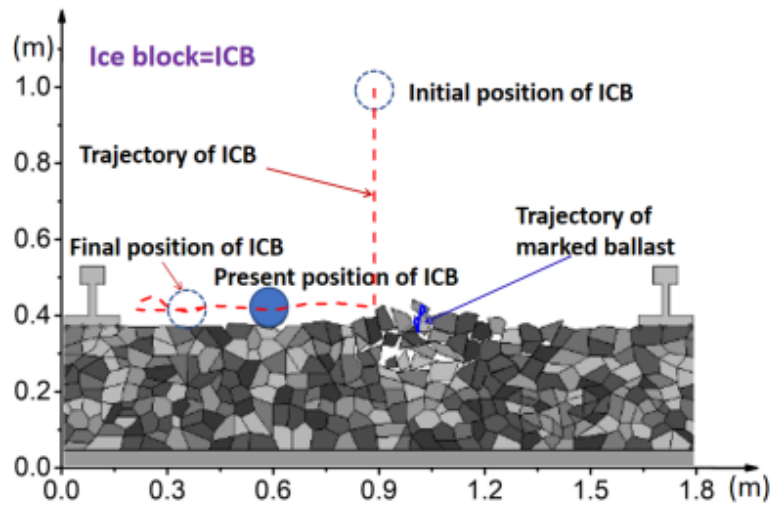
Figure 5.7 shows the displacement of the ice block and a marked ballast. In general, a larger initial velocity induces greater displacement. However, unlike in the case of small and moderate initial vertical velocities (0 m/s and 5 m/s), during the collision process at initial vertical velocity of 10 m/s , there is a collision between ice block and rail, which may reduce significantly the displacement of ice block after the impact (see Figure 5.7(a)). It follows that the ballast trajectories and displacement show that its movement may be divided into three phases. Taking the initial vertical velocity of 5 m/s as an example (see Figure 5.7(b)), the first phase sited between $t= 0\text{ s}$ and $t= 0.11\text{ s}$ corresponds to a stable state of the ballast which remains motionless before its impact by the ice blocks. The second phase sited between $t= 0.11\text{ s}$ and $t= 0.34\text{ s}$ corresponds to the impact and flying processes in which the ballast undergoes a rebound following a parabolic curve. The third phase sited after $t= 0.34\text{ s}$ corresponds to the marked ballast fly-back. It should be mentioned that the severity and the duration of every phase strongly depend on the initial vertical velocity. The increased initial vertical velocity induces greater displacement of the ballast, and longer flight duration, which results in a more serious consequence.

5.4.1.2 Longitudinal section

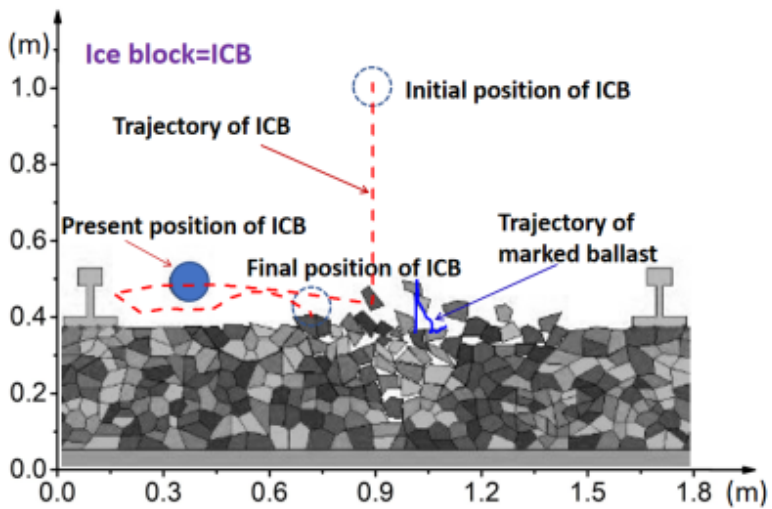
The longitudinal section is more realistic since it considers the real velocity of the ice block dropping from high-speed trains. The high-speed railway is commonly defined by the maximum running speed exceeds 200 km/h . However, the running speed of high-speed railways in China, Japan and France exceeds 300 km/h and even the maximum test speed of the eastern line in France is 574.8 km/h [132]. In addition, many ultra-high-speed railways are under development and under construction. In order to analyze the initial dropping velocity of the ice block, the



(a)



(b)



(c)

Figure 5.5: Computed ballast flight depending on the initial vertical velocity: (a) $V_y = 0 \text{ m/s}$ (free fall); (b) $V_y = 5 \text{ m/s}$; (c) $V_y = 10 \text{ m/s}$

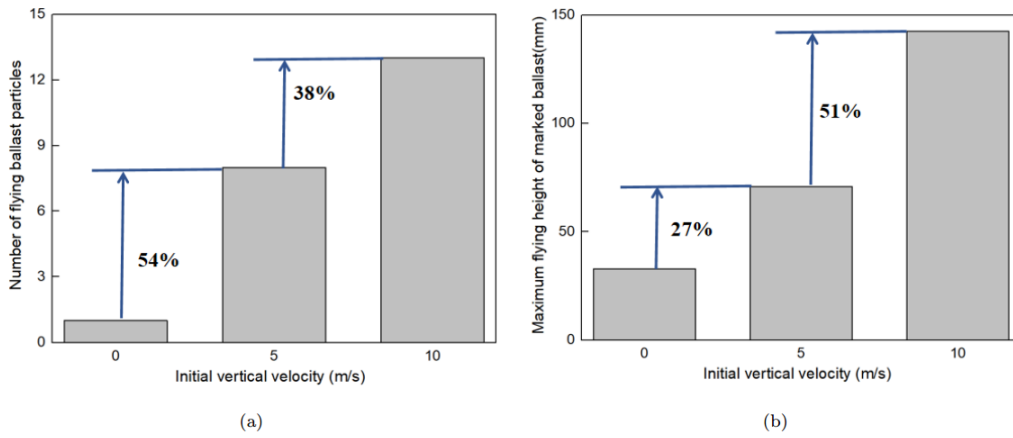


Figure 5.6: Relationship between (a) number of flying ballast particles and initial vertical velocity of ice block, (b) maximum flying height and initial vertical velocity of ice block

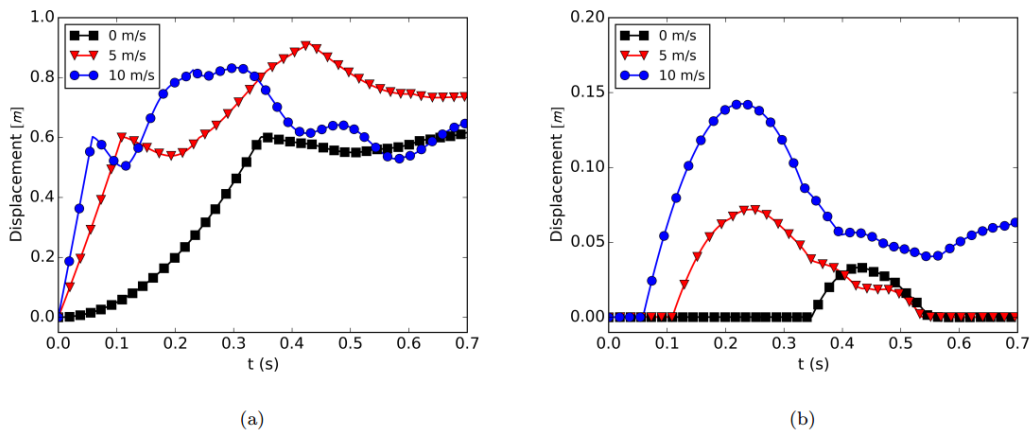


Figure 5.7: The displacement of (a) ice block and (b) marked ballast for different initial vertical velocity in cross section

initial collision position was set on the surface of the ballast bed. An initial vertical velocity of 3.5 m/s which corresponded to the falling height of 600 mm , the initial longitudinal velocity equal to the train running speed, and four initial longitudinal velocities from 100 km/h to 400 km/h with an interval of 100 km/h were used. The trajectory of the ice block and marked ballast, as well as the phenomenon of ballast bed after the collision, is represented in Figure 5.8. It is clear that the track bed was damaged after the collision, the ballast particles were hit and displaced, and the surface of the track bed showed different degrees of depression. The severity of the damage of the track bed had a positive relationship with the initial longitudinal velocity. For the trajectory of the ice block, the ice block quickly flew upward and forward after the collision. For the trajectory of marked ballast, we know that the ballast flew to the front direction. The height and distance of the ballast flight increased with the initial longitudinal velocity. When the dropping longitudinal velocity is more than 300 km/h , the marked ballast may collide with the train underframe since the maximum height of the marked ballast after the collision is more than 330 mm (distance from the ballast bed to train underframe)[137]. If the ice and ballast particles reach the train underframe, they may accelerate significantly due to the collision with the train or may strike off more ice /snow blocks, causing more serious consequences. Indeed, the effects of ballast projection may vary from depending on where the particle lands. By considering the ballast particles flying height H , the impact risk is classified into three categories:

- If $H \leq 184 \text{ mm}$ (height of UIC-60 rail), flying ballast particles have the possibility to hit the rail;
- If $184 \text{ mm} < H \leq 330 \text{ mm}$, flying ballast particles have the possibility to hit the wheels of the train ;
- If $H > 330 \text{ mm}$, flying ballast particles will certainly hit the bottom of the train, and probably the rail and the wheels of the train.

The displacement of the marked ballast and the ice block was calculated, as shown in Figure 5.9. Results show that the displacement of marked ballast is linear with the increasing initial longitudinal velocity at $t = 0.5 \text{ s}$. The displacement of marked ballast of 400 km/h is about four times of that 100 km/h . Significantly, the initial longitudinal velocity of the ice block directly affects the displacement of ice block and ballast particles. From Figure 5.10, the numerical results show that the number of flying ballast particles and the vertical displacement of marked ballast increases from 100 km/h to 400 km/h . When the longitudinal velocity of ice block is in

the range of 200 *km/h* to 300 *km/h*, the results exhibit a peak of 33 % and 47 % of the total number of flying ballast and a maximum flying height of marked ballast. Above 300 *km/h*, this process evolution increases gradually until a plateau is reached. This non-uniform evolution may be related to the gradation of ballast composed of different particle sizes. As the longitudinal velocity increases, most of the small size and a part of the middle size of ballast particles in the impacted area fly above the bed surface.

According to the above simulation results, the initial longitudinal velocity of the snow / ice block which is directly dependent on the running speed of the train, has a great impact on the ballast flight. Reducing the speed of trains is the simplest and most effective mitigation strategy. However, this method may defeat the main purpose of high-speed lines. The national center of operation of SNCF in France proposed a time schedule which divided train speed into three kinds: acceptable, tolerable and unacceptable. The weather forecast, mechanical simulation, and safety approach were taken into consideration.

5.4.2 Incident angle of ice block

Regarding the angle of incidence of the ice block, in the longitudinal section, this angle can correspond to the different attachment positions of the ice, as shown in Figure 5.11. The incident angle is not an independent variable, while it is related to the train speed and the distance of drop as well as the ice dropping position; therefore, four angles (0° , 30° , 60° , and 90°) were investigated in the simulation. The incident angles were controlled by the velocity of the longitudinal and vertical directions. The total velocity was set to 20 *m/s*.

Figure 5.12 shows the trajectory of the ice block and the marked ballast as well as the response of the track bed after the collision at different ejection angles. Based on these simulation results, it can be seen that the incident angle is also one of the main factors affecting ballast flight. When the incident angle is 0° , the effect is insignificant, and just two ballast particles are moved above the surface. The maximum vertical displacement of the marked ballast is only 1.1 *cm*. Among the four angles, the ejection angle of 90° has the widest and the deepest impact, where the displacement direction of the marked ballast is essentially vertical. When the angle is 30° or 60° , there is a larger longitudinal and vertical displacement. Comparing the reflection angles of the ice block in the four cases, the larger the angle of incidence, the larger angle of reflection, and the greater probability that the ice block collides with the bottom of the train. Figure 5.13 shows the displacement

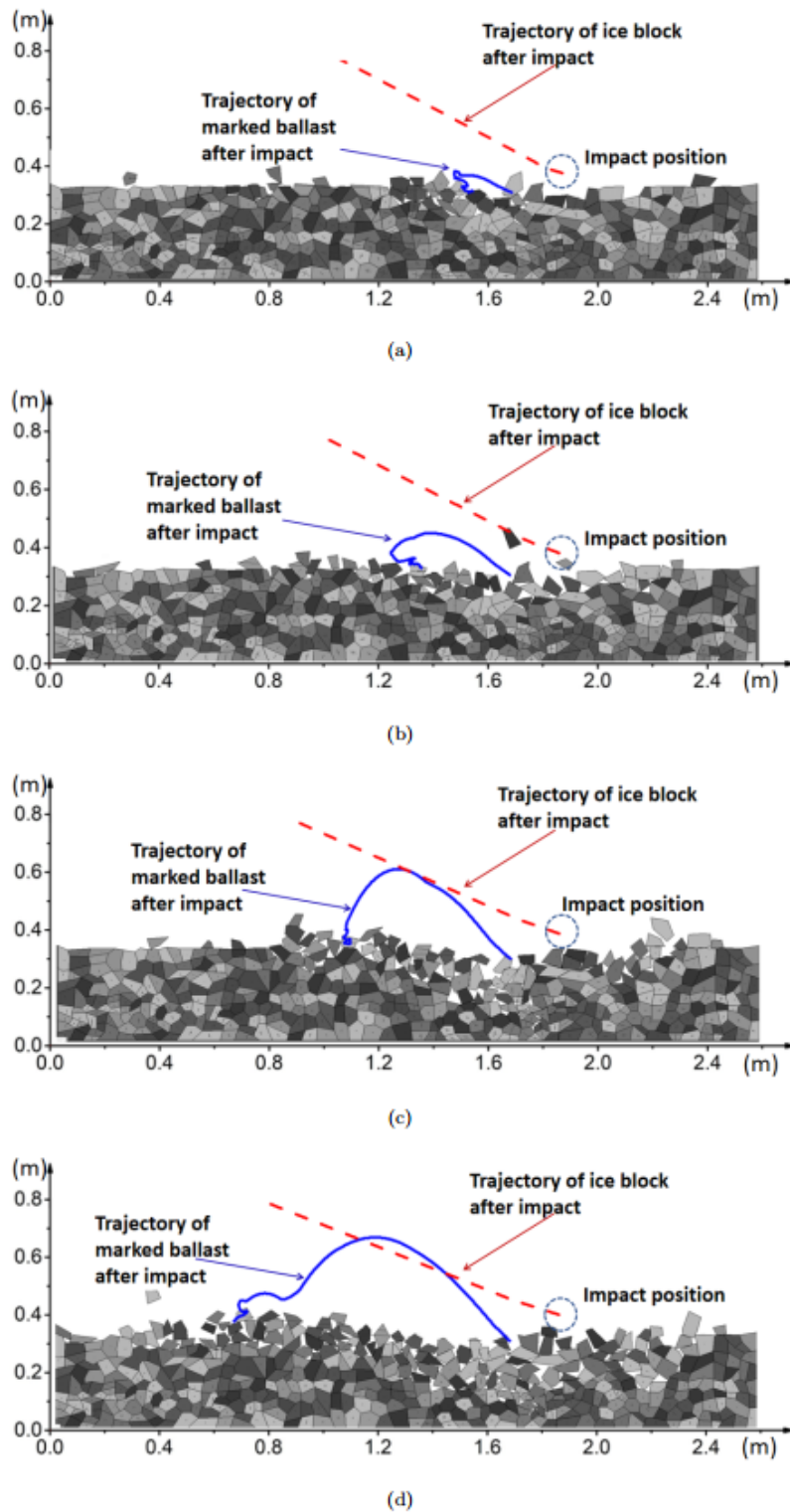


Figure 5.8: Relationship between ballast flight and longitudinal velocity: (a) $V_x = 100 \text{ km/h}$; (b) $V_x = 200 \text{ km/h}$; (c) $V_x = 300 \text{ km/h}$; (d) $V_x = 400 \text{ km/h}$

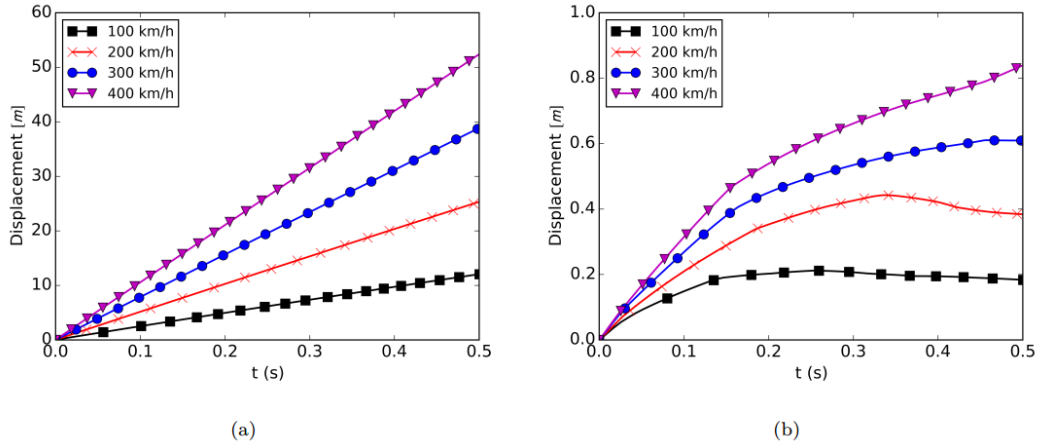


Figure 5.9: The displacement of (a) ice block and (b) marked ballast for different velocities in longitudinal section

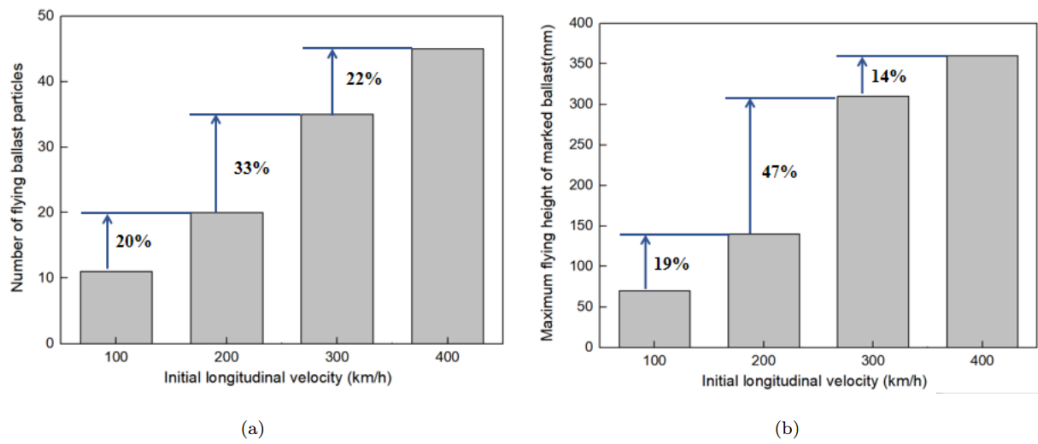


Figure 5.10: Relationship between (a) number of flying ballast particles and initial longitudinal velocity of ice block; (b) maximum flying height and initial longitudinal velocity of ice block

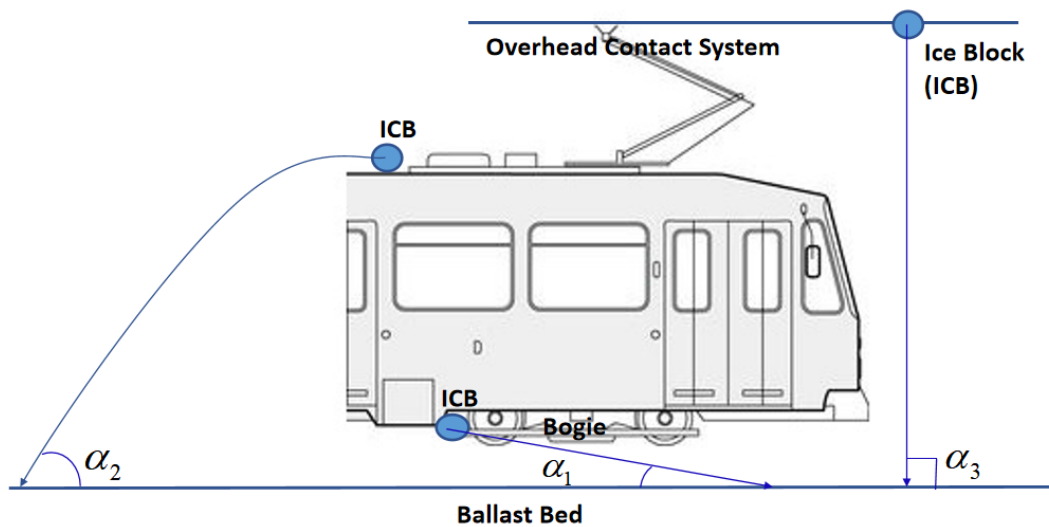


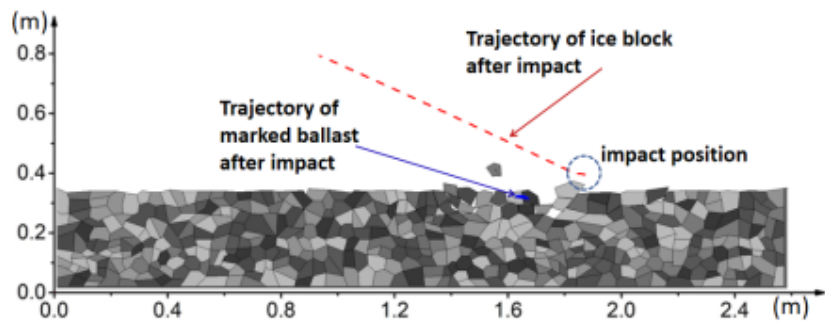
Figure 5.11: Three ice dropping types and incident angles

of the ice block and the marked ballast. The ice block with the incident angle of 0° has the largest displacement of the four angles since the velocity in the longitudinal direction is larger than the others. However, for the displacement of the marked ballast, the displacement of the ballast with an incident angle of 0° is the smallest. The displacement at incident angle of 30° and 60° is larger than the other two. Furthermore, the marked ballast of 90° has a large second rebound process (see Figure 5.12(d) and 5.13(b)).

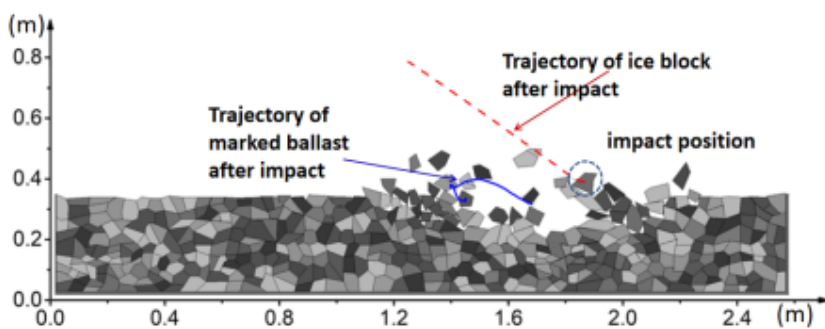
5.4.3 Shape of ice block

In the third simulation, circular, triangular and square ice blocks with a diameter/-side length of 100 mm were placed 600 mm above the ballast bed surface at the center of the track. With the initial vertical velocity of 10 m/s , the impact results are shown in Figure 5.14.

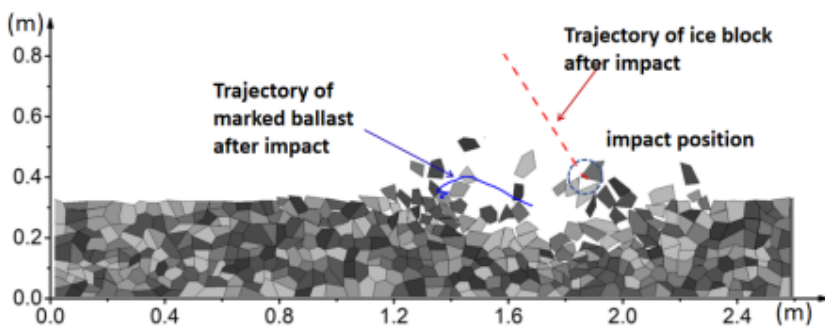
Three shapes of ice block trajectories are significantly different. The triangular ice intrudes the ballast bed directly after colliding, while the square ice bounces off. The trajectory of the circular bounced and hit the trackbed twice. Furthermore, according to the response of the ballast bed after collision, the triangular ice ejected the greatest number of particles and caused the greatest height of ejection, on account of its contact area with the track bed being the smallest, resulting in maximum pressure. The square ice has the widest and the deepest impact among the three, due to its larger contact area and greater mass. The results of the displacement of the ice block and the marked ballast are shown in Figure 5.15. After the collision, the triangular ice has the smallest displacement and the square ice has the largest



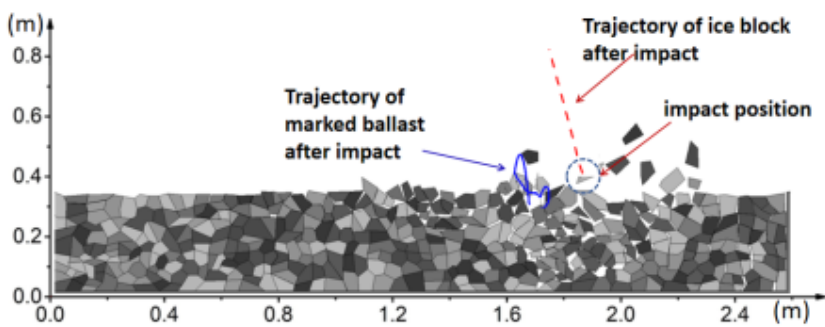
(a)



(b)



(c)



(d)

Figure 5.12: Ballast flight at different incident ejection angles: (a) $\alpha = 0^\circ$; (b) $\alpha = 30^\circ$; (c) $\alpha = 60^\circ$; (d) $\alpha = 90^\circ$

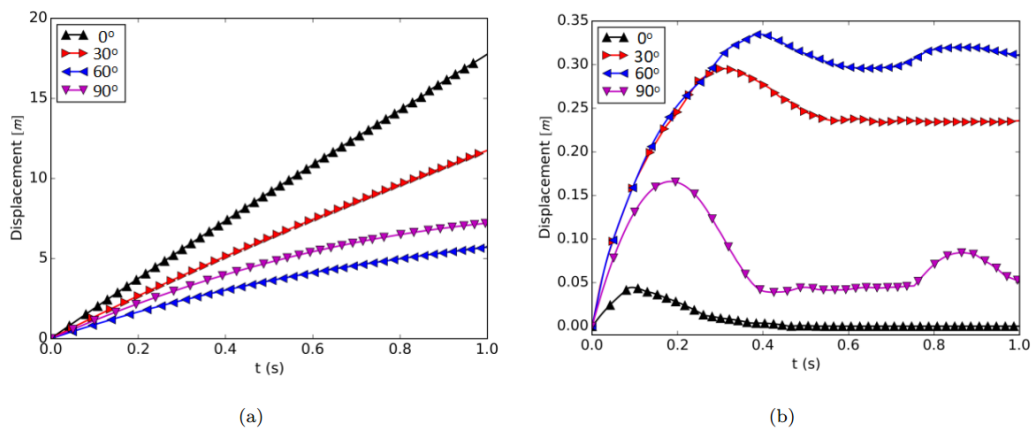
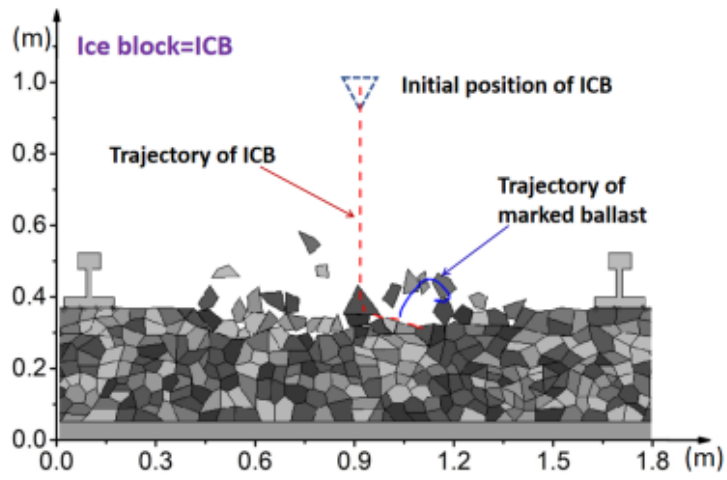


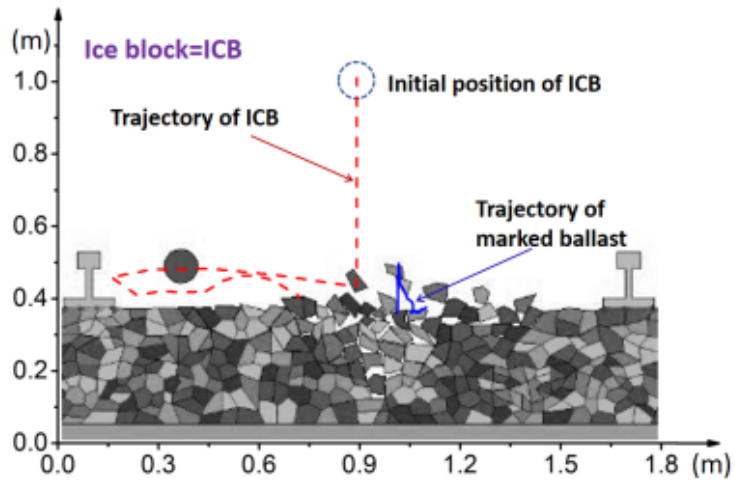
Figure 5.13: The displacement of (a) ice block and (b) marked ballast for different angles in longitudinal section

rebound. The triangular ice causes the maximum displacement of ballast particles, followed by the circular ice and then the square ice.

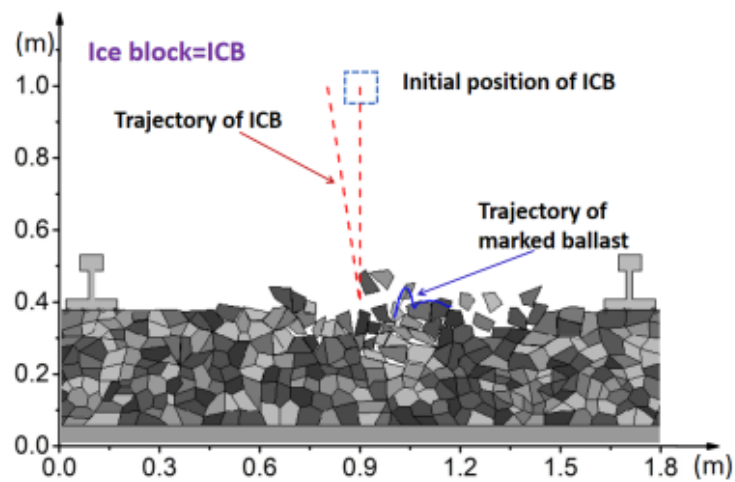
An investigation by the Japan Railway Technical Research Institute showed that the density of the packing snow and ice at the bottom of a train is from 150 to 900 kg/m^3 and the maximum weight of snow / ice that may drop is about 15 kg . Furthermore, the shape of the snow / ice block which drops from the train is various and irregular [147]. Therefore, the ballast flight caused by different shapes of snow / ice block is very complex and serious.



(a)



(b)



(c)

Figure 5.14: Relationship between ballast flight and ice block shape: (a) Triangle; (b) Circle; (c) Square

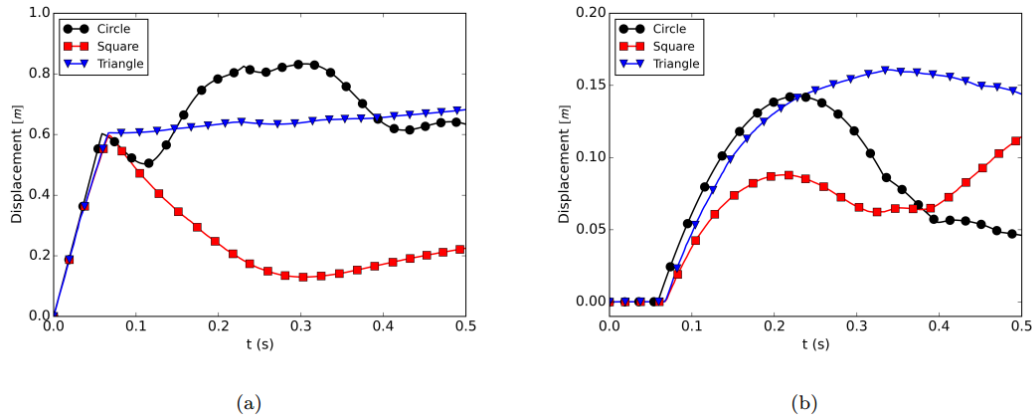


Figure 5.15: The displacement of (a) ice block and (b) marked ballast of different shapes

5.5 Concluding remarks

A numerical model based on the 2D-DDA method, was proposed to study the dynamic behavior of ballast stones and their collision with a snow / ice block. This study took into account the shapes of the ice blocks and the contacts between ballast particles, where we assumed that contact constraints were imposed through the penalty method. The ballast flight induced by the dropping snow / ice with some variations in intensity depends on the velocity, the incident angle, and shapes of the ice blocks. The main findings derived from the numerical simulation may be summarized as follows:

- The velocity of the snow / ice block, which directly depends on the running speed of the train and the position of the ice attached, has a great impact on the ballast flight.
- In the longitudinal-section, the number of flying ballast particles and their displacement increase from 100 km/h to 400 km/h . When the longitudinal velocity of the ice block is in the range of 200 km/h to 300 km/h , the results exhibit a peak of 33 % and 47 % of the total number of flying ballast and maximum of flying height of marked ballast.
- The angle of impact greatly influences the direction of the movement of the ballast particles. The angle of incoming snow / ice blocks, which indeed are the impacting projectiles, is closely related to the location of a detaching projectile. Hence, it is worthwhile that, in order to significantly reduce the ballast flight caused by the melting of snow / ice blocks, some measures should be taken to

prevent snow accumulating in the train and snow settlement.

– The shape of the snow / ice block affects the extent of ballast flight. The triangular ice block intrudes the ballast bed directly after collision, while the square ice bounces off. The triangular ice ejects the greatest number of particles and causes the greatest height of ejection. The square ice has the widest and the deepest impact among the three.

Also, it is worth noting that very little research has been done on ice block and ballast particle breakage from the point of view of aerodynamic interactions and numerical modeling . The breakage process is very important as it may indicate the violence of the impact after the flying ballast collision step. Thus, the analysis of the breakage process by the DDA method is still an open problem which should be undertaken in future studies.

Fluid-Solid coupling application to stability of breakwater

6.1 Introduction

In this chapter, a coupled Fluid-Porous-Solid model is used to study the stability of breakwater. The following aspects and results are emphasized:

- The porous non-linear equations are added to the inertia terms of RANS fluid equations;
- The solid model is based on the Discontinuous Deformation Analysis method;
- The coupling between the fluid and the solid is carried out by transmitting the pressure of the fluid mesh nodes to the solid polygon vertices;
- The breakwater stability depends on the thickness and slopes of the porous layer;
- The breakwater stability depends on the shape of armour units.

6.2 Background

Breakwaters are used for the protection of harbors and beaches against wave action. Their failure may be caused by the motion of the caissons and the global instability of the rubble mound [148, 149]. For the motion of caissons, the most common forms are sliding, subsidence, and overturning [150], which may induce the movement of armour units to increase the failure of the breakwater.

Elsewhere, breakwater failures have been investigated by several empirical studies [151, 152] and by some numerical and experimental methods [153, 154]. For the computational techniques, the computational fluid dynamics (CFD) method is the most common tool used to describe the wave impacts. Kocaman et al. [155]

discussed the impact of dam-break induced shock waves on a vertical wall by a CFD RANS-VOF solution. The simulation results show that the impact of dam-break flood waves on the vertical wall causes wave reflection against the wall and the occurrence of a negative wave. The impacts of waves on the vertical wall were also investigated by Liu et al. [156] using a two-phase compressible CFD solver. Recently, many researchers made a series of attempts to couple the fluid and solid models. Discrete Element Method (DEM) is usually used to calculate the movement of armour units. A wave-structure interaction method was proposed by Latham et al. [157]. In this method, the forces and the volume fraction from the CFD model are mapped onto the DEM structure. Ren et al. [158] used a coupled SPH-DEM method to investigate the stability of armour units in rubble-mound breakwaters. An interfacial force-balance condition achieved the coupling between the fluid particle (SPH) and the solid spheres (DEM).

Due to the complexity of the breakwater structure, the porous medium should also be considered. Traditionally, Darcy's law and Forchheimer law were used to investigate linear and non-linear structures for porous armour layer [109]. Hsu et al. [159] proposed a mathematical model based on the Volume-Averaged Reynolds-Averaged Navier-Stokes (RANS) equations that coupled the fluid and the porous medium to describe surface wave motions in the vicinity of a coastal structure. In this model, the Forchheimer law was added by the volume-averaged process. Additionally, this fluid and porous medium coupled model is also developed in OpenFoam [110, 160, 161, 113], an extended Forchheimer law which adds a mass term that accelerates a certain amount of water considered.

In this chapter, we present a triple-coupled Fluid-Porous-Solid model. The fluid model is described by the Volume-Averaged Reynolds-Averaged Navier-Stokes equations in which the extended Forchheimer law used to calculate the porous medium flow is added to the inertia terms [159]. The solid model, which is based on the 2D-DDA, is used to compute the movement of the caisson and armour units [9]. This method enables to take into account the shapes of armour units, as well as the contact between blocks. The coupling between the fluid and the solid is carried out by a transmission strategy of the fluid mesh nodes' pressure towards the solid polygon vertices, while the coupling between the fluid and the porous medium consists of the equations of the porous model in terms of the inertia of the fluid model.

6.3 Numerical model and validation

The numerical simulations were performed to analyze the flow evolution and to characterize the forces on the breakwater subjected to violent wave impacts. The breakwater is composed of a vertical caisson with shoreward armour units and a porous seaward armour layer (see Figure 6.1). The hydrodynamic impact is generated by the solitary wave, with a wave height ($h_w = 6\text{ m}$) and a water depth $d_w = 10\text{ m}$. The caisson position $x/h_c = 15.96$ (where $h_c = 13\text{ m}$ is the height of the caisson)[162, 163]. It is worth noting that the armour layer protects the structure from the attacks of incident waves by dissipating their energy. These armour layers are often built of large armour units and can be considered as a porous medium. Indeed, many recent scientific studies have considered the porosity parameter to represent different types of armour units in the CFD simulations. Van Gent [112] proposed a value laying between 0.25 to 0.4 for cube-shaped units and suggested a porosity value of 0.49 for tetrapod-shaped units. An armour layer thickness of 2 m and a porosity value of 0.49 are used in the following simulations. The location of the gauges is also identified in Figure 6.1, numbered from 1 to 5, to monitor the surface and the velocity of waves.

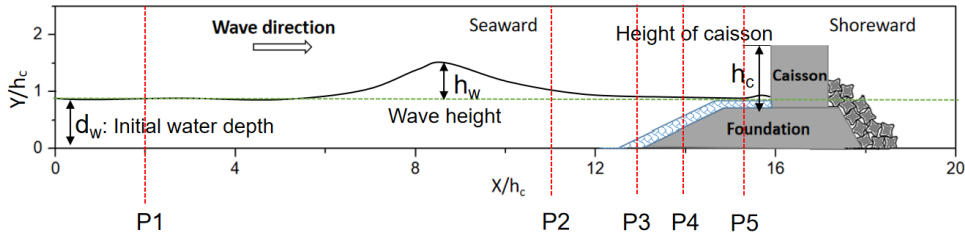


Figure 6.1: Schematic illustration of the computational domain. Wave type: solitary wave; wave height $h_w = 6\text{ m}$; water depth $d_w = 10\text{ m}$; armour layer thickness $T_a = 2\text{ m}$; breakwater caisson height $h_c = 13\text{ m}$; caisson position: $x/h_c = 15.96$. The precise location of gauges P1-P5 is $2h_c$, $11h_c$, $13h_c$, $14h_c$ and $15.5h_c$ (m), respectively.

6.3.1 Boundary conditions

- In the input computational domain, the free surface elevation η is given by:

$$\eta = h_w \operatorname{sech}^2 \left[\sqrt{\frac{3h_w}{4d_w^3}} X + \psi \right] \quad (6.1)$$

where $X = (x - ct)$, h_w is the wave height, d_w is the water depth, ψ is the wave phase shift, and the wave celerity c is $\sqrt{g(h_w + d_w)}$. The horizontal and vertical

velocity components U_h and U_v verify [164]:

$$U_h = \frac{\eta\sqrt{gd_w}}{d_w} \left[1 - \frac{\eta}{4d_w} + \frac{d_w^2}{3\eta} \left(1 - \frac{3y^2}{2d_w^2} \right) \frac{d^2\eta}{dX^2} \right] \quad (6.2)$$

and

$$U_v = \frac{-y\sqrt{gd_w}}{d_w} \left[\left(1 - \frac{\eta}{2d_w} \right) \frac{d\eta}{dX} + \frac{1}{3}d_w^2 \left(1 - \frac{y^2}{2d_w^2} \right) \frac{d^3\eta}{dX^3} \right] \quad (6.3)$$

where x and y are the horizontal and the vertical space variables. Here, we assume that the boundary is at $x=0$, and the free surface will start from the highest point of the solitary wave.

- At the top boundary, we assume $p = p_{atmospheric}$; at the bottom boundary, we set a slip condition, where the roughness can be assumed to be negligible.

6.3.2 Mesh and time step convergence

The validation of the fluid model is carried out by comparing the calculated horizontal velocity and water height with the theoretical free surface elevation η at transect P1 (see Figure6.1) deduced from Equation (6.1). Three types of meshes are used for mesh convergence validation, which contains 24510, 48000 and 94080 tetrahedral mesh elements, respectively. A refinement ratio $\sqrt{2}$ is used for the mesh validation [105]. The grid spacing of the coarser meshes ($\Delta x_c, \Delta y_c$) to grid spacing of the finer meshes ($\Delta x_f, \Delta y_f$) is given as:

$$r_g = \frac{\Delta x_c}{\Delta x_f} = \frac{\Delta y_c}{\Delta y_f} = \sqrt{2} \quad (6.4)$$

Figure 6.2(1) shows that the fine and medium meshes have similar results and give better than coarse mesh. Considering both the accuracy and the simulation time, the medium mesh is used for the following studies. Three time steps are designed. Figure 6.2 (2) shows that the results of the three time step cases are all reasonable. The accuracy of the case ($\Delta t=0.1$ s) is clear enough; therefore, we use time steps of 0.1 s in this work. The refinement of the space or time steps can improve the quality of the results; however, this is not enough. It is therefore necessary to use digital diagrams or models, such as Serre [165, 166] or Extended Boussinesq-like models [167], which have good dispersive capacities for accurate prediction of wave activity.

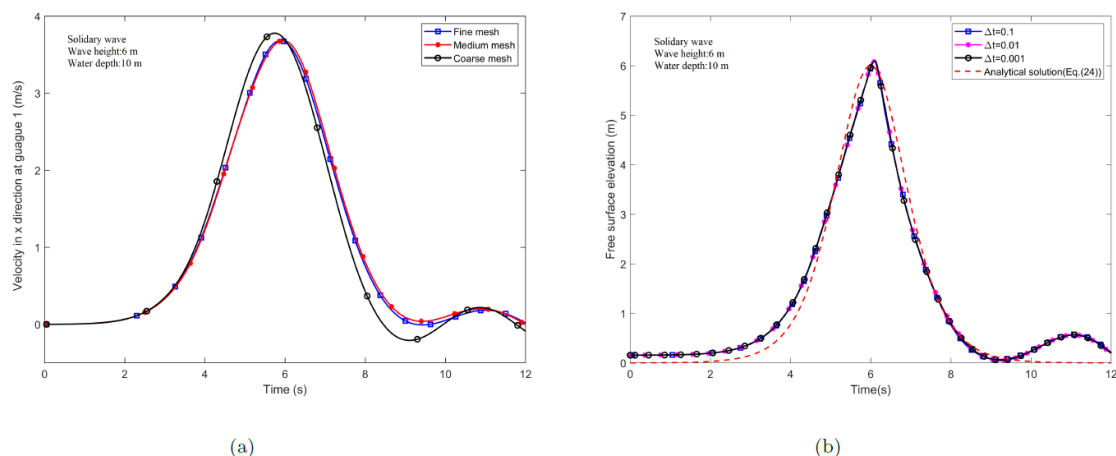


Figure 6.2: (a) Horizontal velocity and free surface elevation of mesh, and (b) time step convergence at gauge P1 (see Figure 6.1 for the wave parameters and gauges location).

6.4 Simulation results

6.4.1 Flow patterns around the breakwater

The simulation of the flow patterns around the breakwater was done by considering the fluid-porous coupling. The wave evolution around the breakwater presented in Figure 6.3 shows that as the wave approaches the vertical caisson grows considerably in amplitude until the breaking process occurs (Figure 6.3(b)). This then leads to an up-moving jet due to the wave-squeezing processes (Figure 6.3(c)).

The distribution of the wave pressure in front of the vertical caisson is shown in Figure 6.4. The normal pressure due to solitary waves is mainly located between 20 s and 25 s. The results show that the fluid pressure is relatively high in the lower half of the caisson, which can induce a risk of sliding of the structure or even give rise to a liftforce which could accentuate the overturning process since the maximum pressure is located at the caisson's toe (see point A, Figure 6.4).

At the vicinity of the breakwater, the height of the waves (expressed as $H=\eta + d_w$) increases considerably as they approach the breakwater until the breaking process occurs, as shown in Figure 6.5. The wave-breaking process happens after the impact between the wave and the caisson [167]. Three main reasons cause this wave-breaking process: (1) non-linear terms and secondary waves, (2) reflection on the porous medium and the caisson, (3) wave-wave interactions.

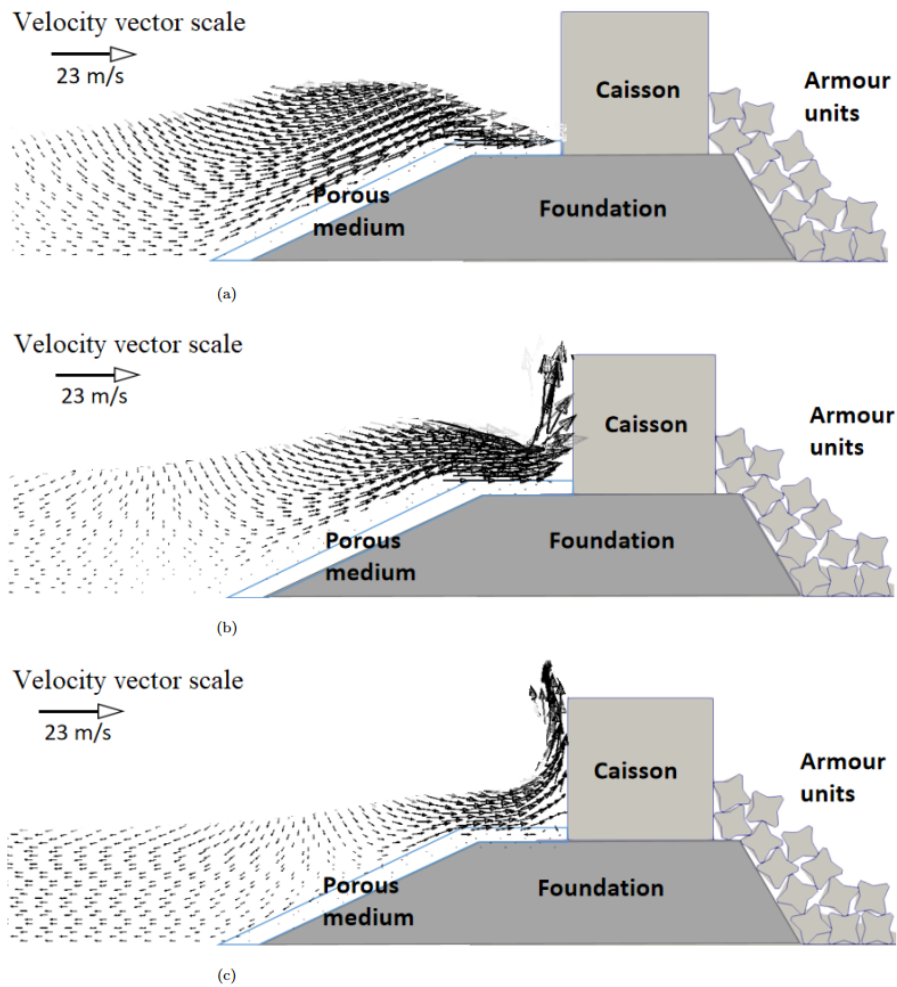


Figure 6.3: Pattern changes: (a) $t = 19.5$ s; (b) $t = 20.5$ s; (c) $t = 21.5$ s. The impacting wave is a solitary wave with a wave height 6 m and a water height 10 m. The caisson height is 13 m. The thickness of the porous medium (porosity = 0.49) is 2 m. The slope is 1:2.

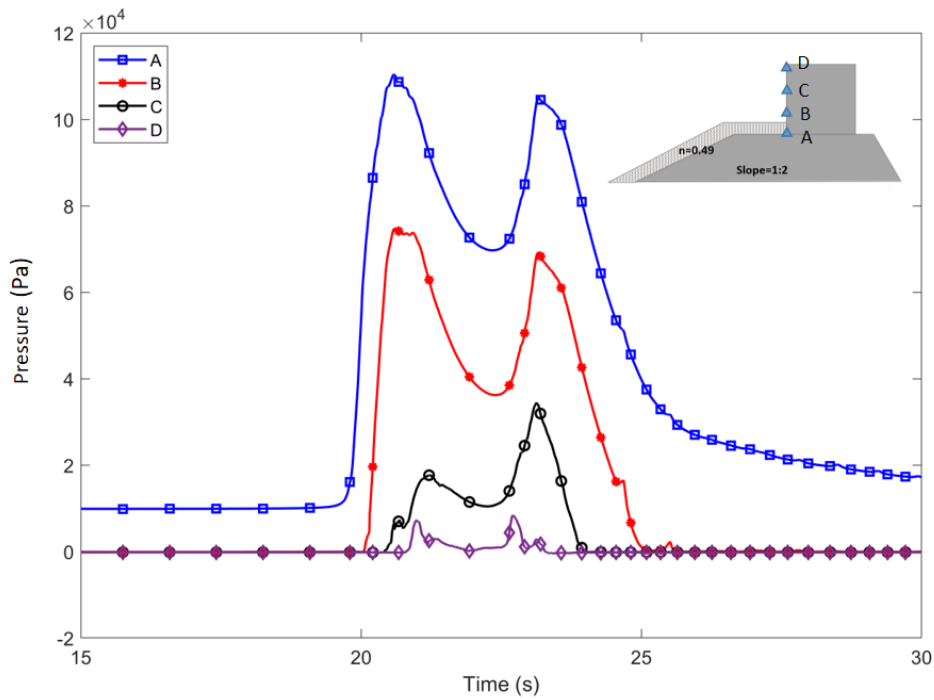


Figure 6.4: Pressure distribution along the vertical caisson. The impacting wave is a solitary wave with a wave height 6 m and a water height 10 m. Point A is located at the bottom of the caisson. Points B-D are $\frac{1}{3}h_c$, $\frac{2}{3}h_c$, and h_c away from point A.

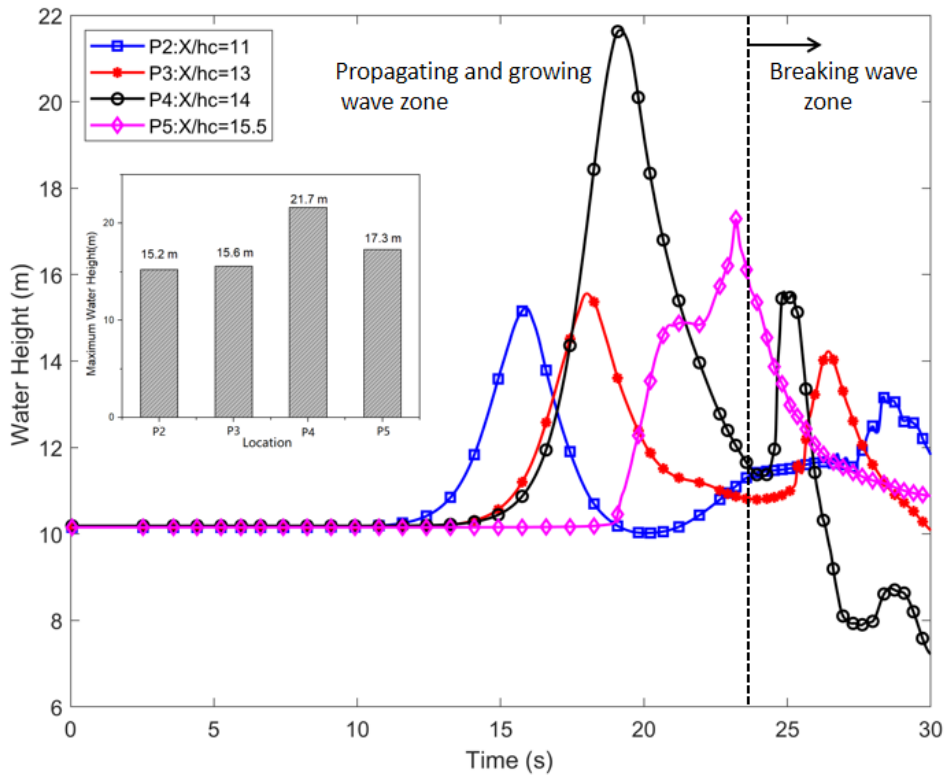


Figure 6.5: Water height evaluation at the vicinity of breakwater (The precise location of gauges P2-P5 see Figure 6.1)

6.4.2 Solution behavior with the breakwater seaward slopes

The wave motion and the flow pattern on the breakwater seaward slope are simulated by the Fluid-Porous model, in which four slopes are considered. The slopes are assumed to be 1:S, where S is the ratio of the slope bottom length to the slope height, which equals 1, 2, 3, and 4. The simulation results are shown in Figure 6.6.

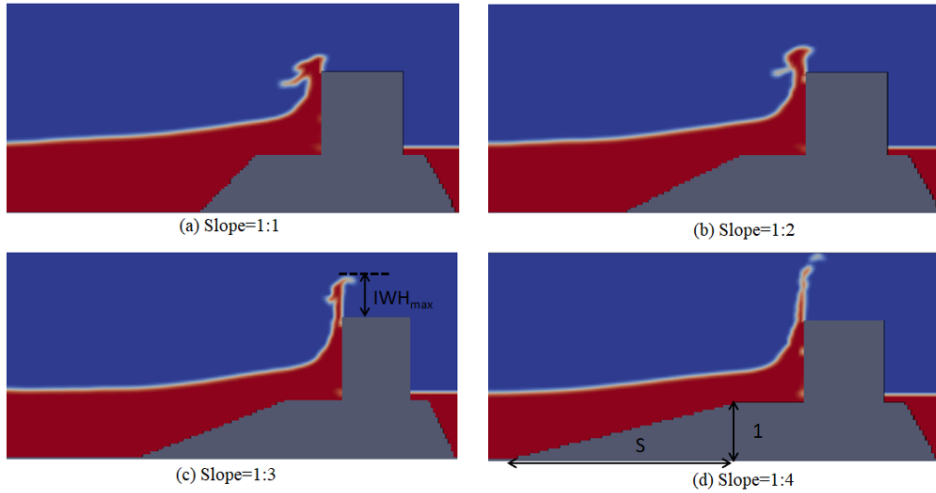


Figure 6.6: Surface wave deviation with various seaward slopes (1:S). For the wave parameters, see Figure 6.1. The IWH_{max} of the four slopes are: (a) 1.86 m, (b) 3.71 m, (c) 5.57 m and (d) 9.28 m, respectively.

We then define the maximum impacting wave height (IWH_{max}) as the peak of the incoming wave height after it impacts the caisson, as shown in Figure 6.6. Due to the squeezing process of the breakwater, we observe that a larger S induces a bigger (IWH_{max}) but less water is ejected. Hence, the Impacting Wave Height (IWH_{max}) can be fitted through the following formula:

$$IWH_{max} = \alpha_1 + \alpha_2 e^{\alpha_3 S} \quad (6.5)$$

where $\alpha_1=0.41$, $\alpha_2=1.45$ and $\alpha_3=0.5$. Fitting results are shown in Figure 6.7.

The seaward porous medium affects the wave. The turbulent kinetic energy K for various thickness of the porous layer is shown in Figure 6.8. The large porous layer has less turbulent kinetic energy due to a large dissipation. Several turbulences can be found on the upper side of the caisson on the shoreward side, in the middle of the caisson on the seaward side, as well as at the top and bottom of the porous medium. The flow in the porous medium initially coincides with the direction of the wave and then opposes it [168]. The porous medium significantly reduces the effects of the breaking waves.

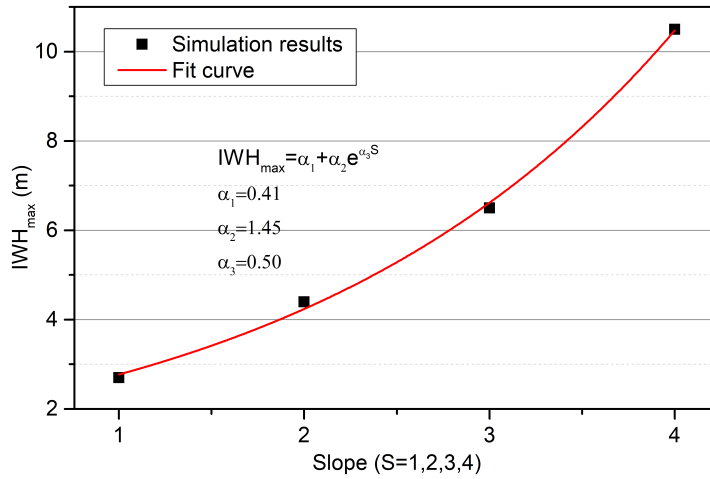


Figure 6.7: Variation of IWH_{max} (see Figure 6.6) for various seaward slopes.

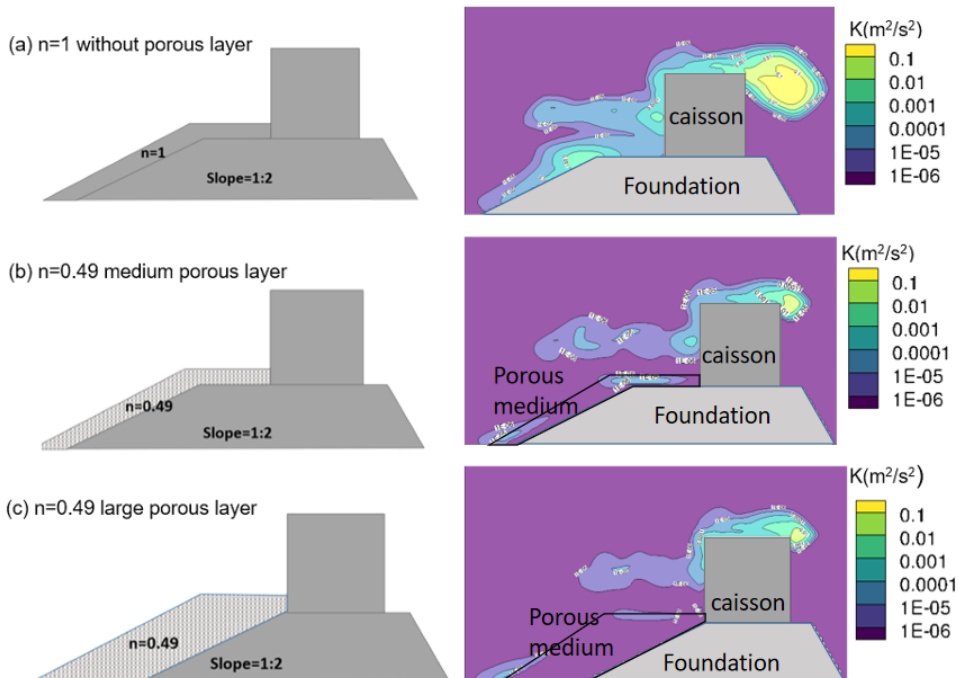


Figure 6.8: Turbulent kinetic energy K for various porous layer thickness in $t=24.0$ s. (see Figure 6.1 for the wave parameters).

6.4.3 Solution behavior with the shape of shoreward armour units

In order to analyze the stability of the shoreward armour units and the influence of their shape, three typically shaped armour [68, 169] (see Figure 6.9) are modeled and placed on the shoreward side of the breakwater. The armour units are optimally arranged to ensure the initial position stability. Six units, numbered from 1 to 6, are shown in Figure 6.10. The breakwater is then subjected to a violent solitary wave impact whose input external force is calculated by Equation (3.27) (see the flow in Figures 6.3 and 6.4). The material parameters used for the Solid-DDA model are shown in Table 6.1.

Table 6.1: Material parameters used for simulations

Young's modulus E	Poisson's ratio ρ	unit weight m	Penalty spring constant P	Coefficient of friction μ
50 GPa	0.30	2400 kg/m ³	2×10^8 N/m	0.6

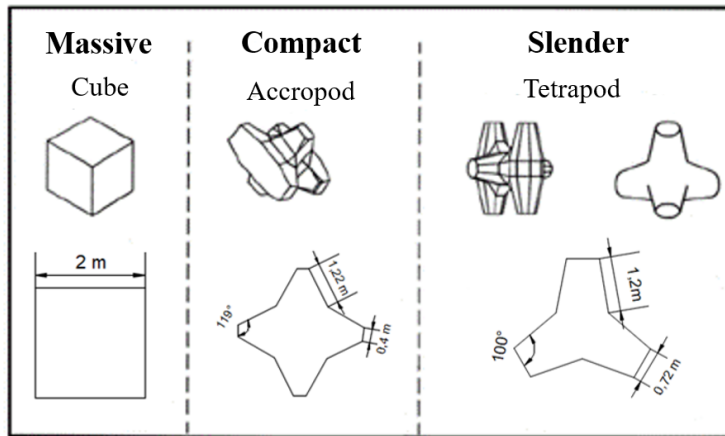


Figure 6.9: Shapes of armour units used in the simulation.

Figure 6.10 shows the initial and the final position of the three various shapes of armour units. The displacement of the caisson hindered by armour units is almost zero and stable while varying degrees of sliding and rotating happen on the armour units. The cubic units are more unstable than the other two; in fact, cubic unit No.2 experienced a significant fall. We found that units No.2 and No.3 have larger vertical displacement while units No.3 and No.6 have large horizontal displacement. Therefore, a falling process always happens on the rear side of the caisson and a sliding process happens on the toe of the breakwater structure. As for the displacement, the accropod and the tetrapod units followed the cubic units in that there is no significant

drop; however, the rotation of the units can be seen. Because the two shaped units are under force, the armour units move to rearrange and the structure becomes more stable, with the tetrapod units.

The standard deviation (SD) of the displacement or the rotation of the armour units is used to describe the stability of the breakwater, which is calculated by:

$$SD = \sqrt{\frac{\sum_{i=1}^N (\phi_i - \bar{\phi})^2}{N}} \quad (6.6)$$

where ϕ_i denotes the displacement or rotation value of units i at the final position, $\bar{\phi}$ is the average displacement or rotation value, and $N = 6$. The standard deviations of the horizontal displacement, the vertical displacement, and the rotation are shown in Figure 6.11. For the displacement of the armour units, we have obtained $SD_{cubic} > SD_{accropod} > SD_{tetrapod}$. For the rotation, however, the accropod units are greater than the cubic and tetrapod units. Furthermore, the cubic units have larger displacements, most of which are in the form of sliding along the slope.

In order to understand the motion of armour units, the trajectory of the six marked armour units is investigated, as shown in Figure 6.12. The tetrapod-shaped units and accropode-shaped units reached a steady-state after two hydrodynamic impacts, while the cubic units continue to move during the five impacts. In general, the displacement of tetrapod-shaped units significantly smaller than the other two shaped units. It is because cubic armour units blocks bring resistance to breakwater by the mass whereas tetrapod and accropode units bring resistance through the mass and block interlock forces. Therefore, the cubic and tetrapod units by sliding and rotation, respectively, to reach a stable state. Besides, the jump in the horizontal displacement for the accropode units can be explained by accropode armour units' rearrangement. The design of the tetrapods is stable even in the most extreme weather and marine conditions, and when arranged together in lines or heaps, they create an interlocking.

Based on the simulation results, the tetrapod units are the most stable, followed by the accropods, and then by the cubic armour units. The reason is that cubic armour units bring resistance to the breakwater through mass whereas tetrapod and accropod blocks bring resistance through mass and interlock forces among units.

6.4.4 Solution behavior with breakwater shoreward slopes

In order to analyze the influence of the slope of breakwater, three different slopes ($\sqrt{3}$:1, 1:1 and 1:2) were investigated. In these three cases, the rubble mound structures

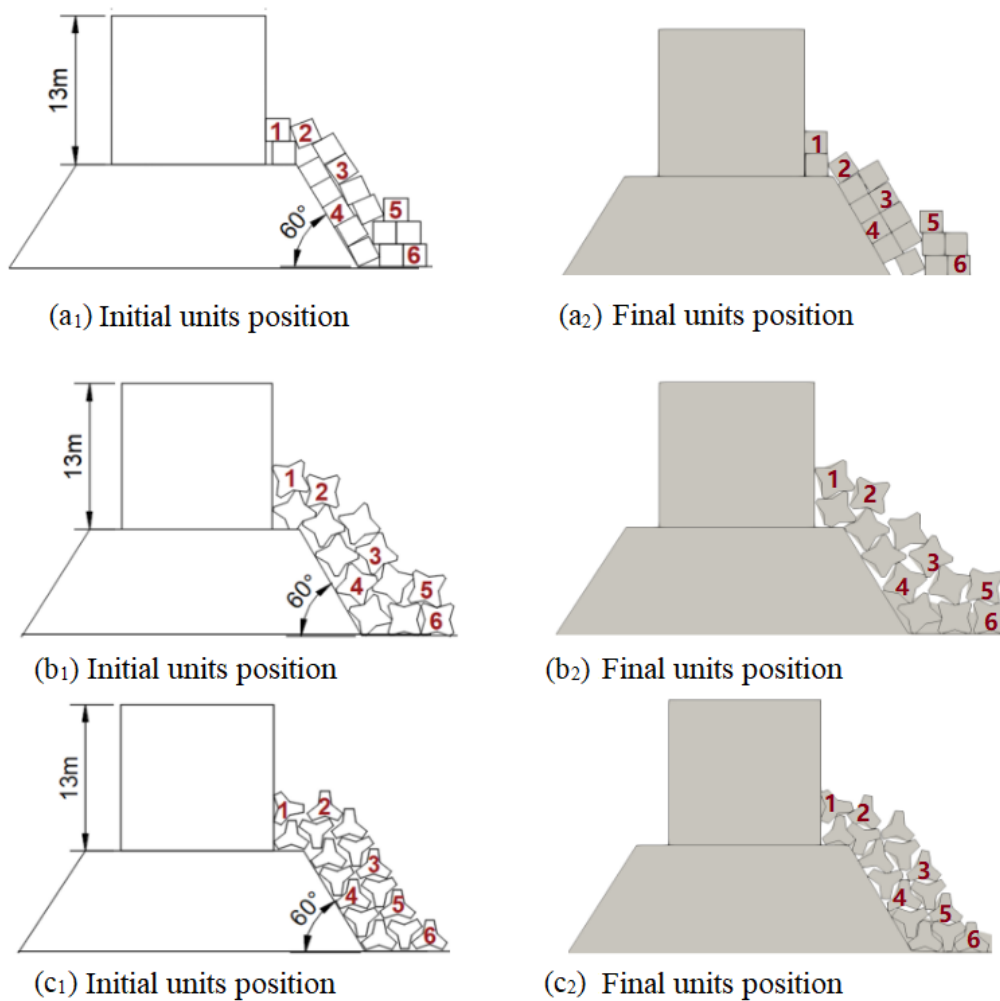


Figure 6.10: Simulated movement for various shapes of armour units: (a) Cube, (b) Accropod, (c) Tetrapod. The breakwater was subjected to solitary wave impacts whose input external force is calculated by Equation (3.27). (See Figure 6.1 for the wave parameters).

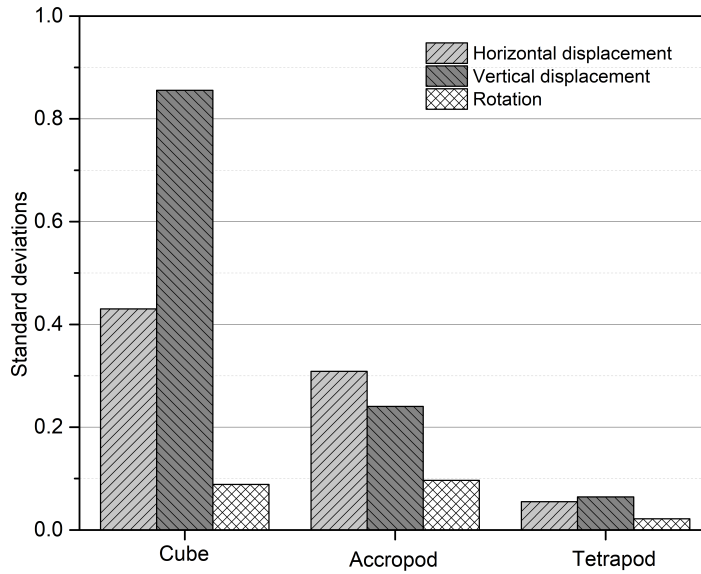
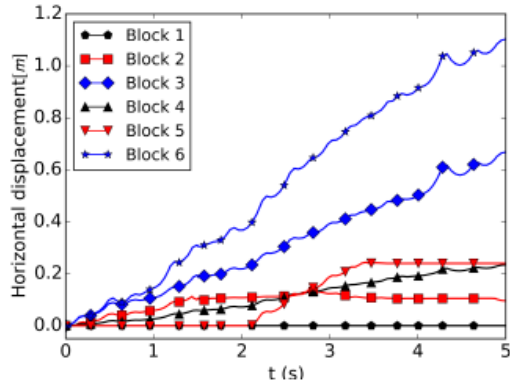


Figure 6.11: Variation of standard deviations for three shapes of armour units.

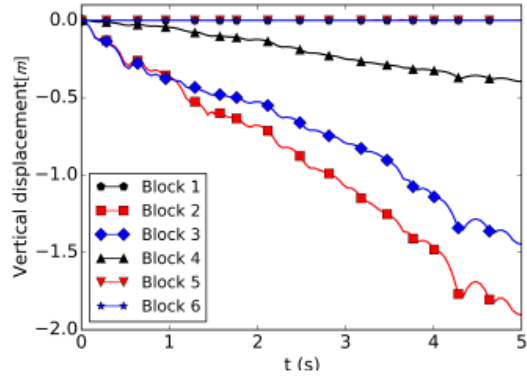
of breakwater are composed of cubic blocks with the side length of 2.0 m. Six blocks, numbered from 1 to 6, are shown in Figure 6.13. The breakwater is then subjected to a violent solitary wave impact whose input external force is calculated by Equation (3.27) ((see the flow in Figures 6.3 and 6.4). The material parameters used for the Solid-DDA model are shown in Table 6.1.

Figure 6.13 shows the original model and final simulation results for three slopes. The displacement of the slope of $\sqrt{3} : 1$ is significantly larger than those of the two other slopes. The slopes of 1:1 and 1:2 have roughly the same displacement from time $t = 0$ s to $t = 1.5$ s. The displacement for the slope 1:2 becomes steady after $t = 1.5$ s. The final caisson displacement for the three slopes is: $D_{\sqrt{3}:1} = 0.501$ m, $D_{1:1} = 0.380$ m, $D_{1:2} = 0.238$ m, respectively. The flatter is the slope, the smaller the displacement of the blocks is, the steadier the breakwater is. The reason is that the rubble mound blocks in the flatter slope have large lateral resistance to the caisson. The standard deviations of horizontal displacement, vertical displacement and rotation are shown in Figure 6.14. For the displacement of rubble mound blocks, we all have $s_{\sqrt{3}:1} > s_{1:1} > s_{1:2}$, while there is no significant discrepancy during the three slopes in term of rotation. The flatter slope was lower standard deviation which indicates that the displacement of blocks tends to be close to the mean. Therefore, the breakwater is more stable when the slope is flatter.

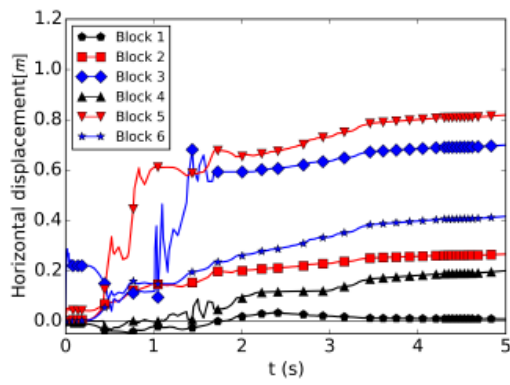
Figure 6.15 shows the horizontal and vertical displacements of the six cubic blocks. The displacement of rear blocks can be divided into two phases: the phase of sliding and the phase of the stable. Slopes 1: 2 and 1: 1 took about 1.2 s and 3 s respectively



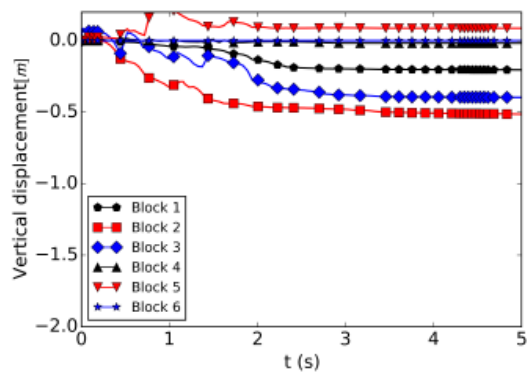
(a) Horizontal displacement for the cubic blocks



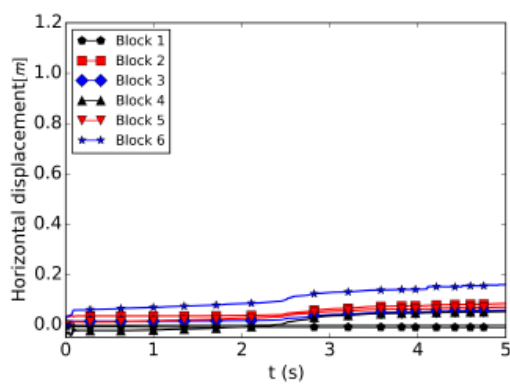
(b) Vertical displacement for the cubic blocks



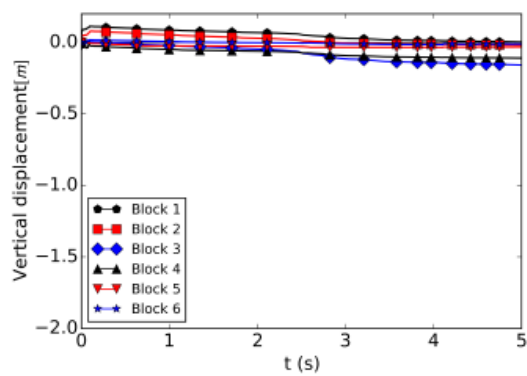
(c) Horizontal displacement for the accropode blocks



(d) Vertical displacement for the accropode blocks



(e) Horizontal displacement for the tetrapod blocks



(f) Vertical displacement for the tetrapod blocks

Figure 6.12: Standard deviations for three slopes

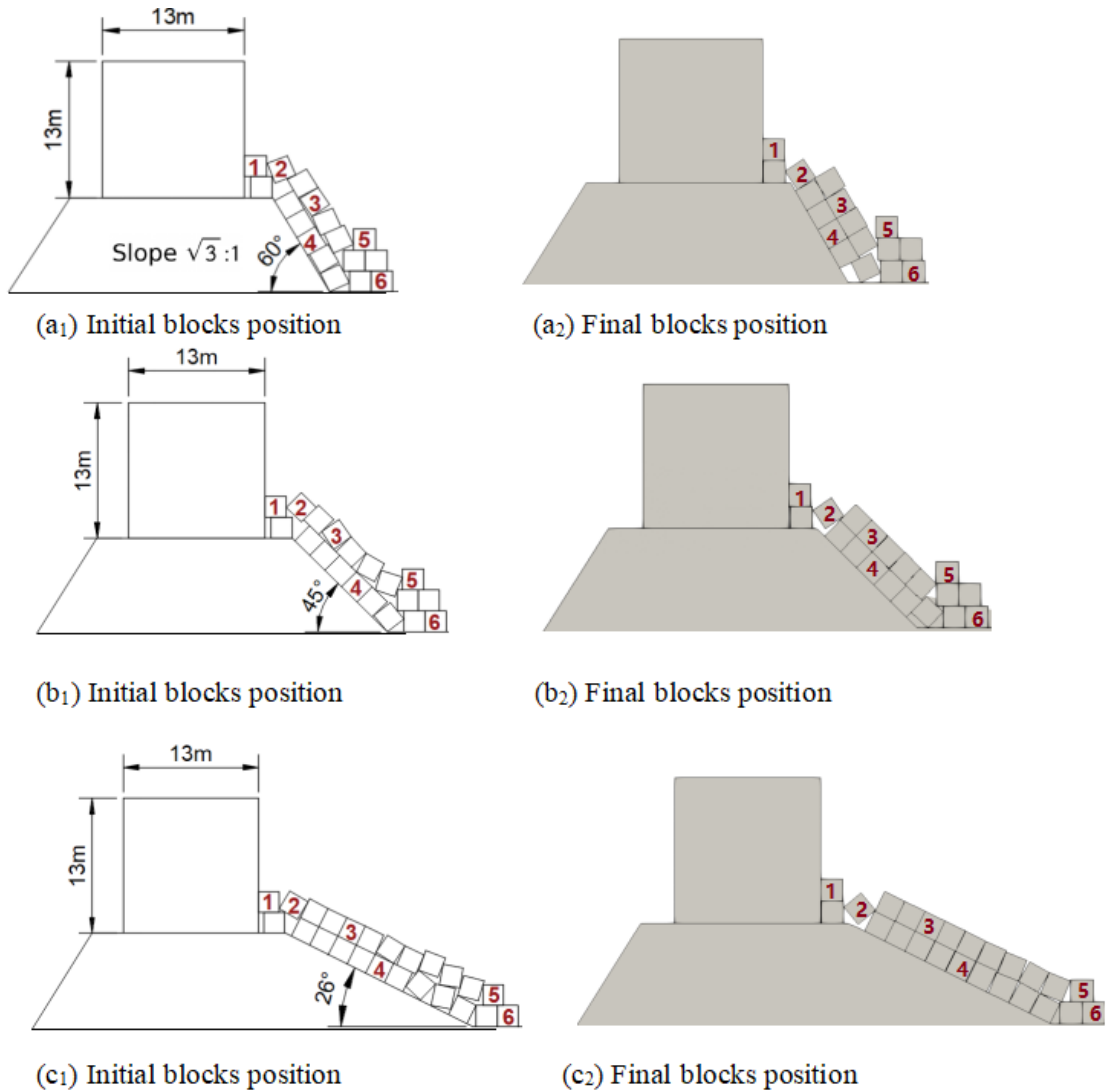


Figure 6.13: Slope of breakwater: (a) slope= $\sqrt{3}:1$; (b) slope=1:1; (c) slope=1:2. The shape of armour unit is cube. The breakwater was subjected to solitary wave impacts whose input external force is calculated by Equation (3.27). (See Figure 6.1 for the wave parameters).

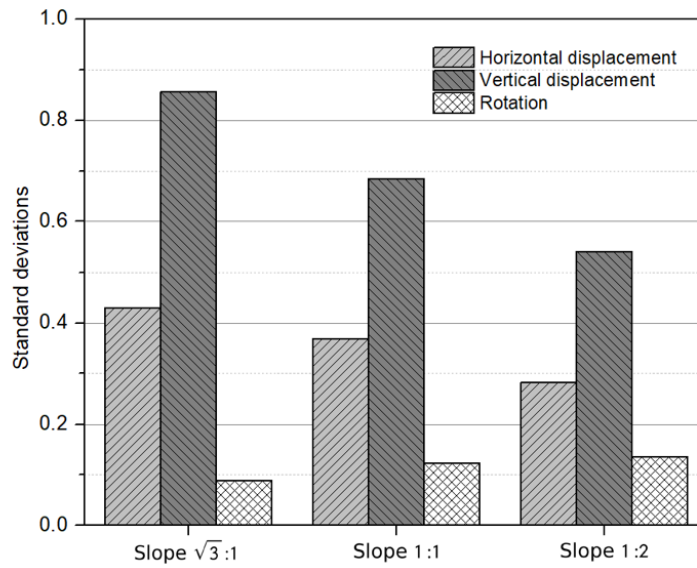


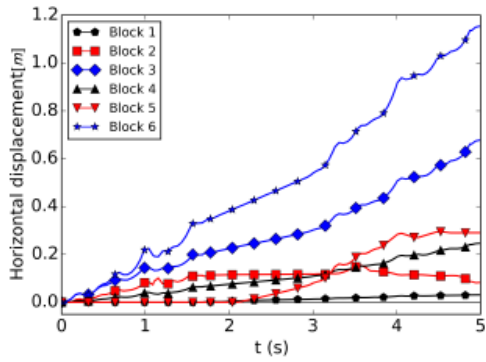
Figure 6.14: Standard deviations for three slopes

to reach steady-state, while the blocks in slope $\sqrt{3}:1$ are still unstable. It is clear that the steeper the slope is, the longer it takes for the blocks to reach a steady state. Besides, Block 2 and block 3 have larger vertical displacement than others. Block 3 and 6 have large horizontal displacement.

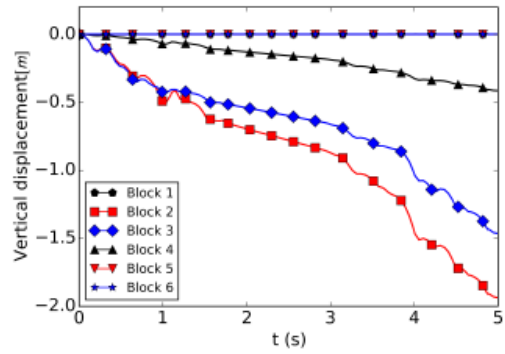
6.4.5 Effect of cohesion

In this simulation, a cohesion $C_f=2\text{ MPa}$ and a tensile strength $\sigma_t = 0.7\text{ MPa}$ are imposed, which may actually represent concrete placed on the surfaces and contact points [68]. These values are obtained by adopting the extended Mohr-Coulomb failure criterion based on the tension cut-off. It consists of reducing the tensile strength of the material by imposing a value of σ_t while ensuring the following condition: $\sigma_t \leq C \cotan\phi$. Thus, by fixing $\sigma_t = 0.7\text{ MPa}$, we decrease the value of C to C_f , which corresponds to the movement of one block of the caisson. C_f is considered optimal.

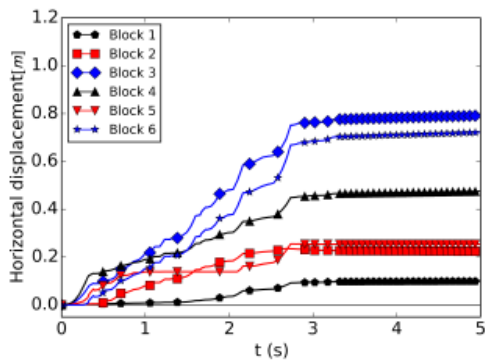
Figure 6.16 shows that the displacement of armour units without cohesion is bigger than the units with cohesion. All the units behind the caisson have been moved but the units No.2 and 5 have moved significantly. Therefore, we have chosen to present only the movements of units No.2 and No.5 as shown in Figure 6.17. For unit No.2, when cohesion forces work, the steady-state can be reached in about 22.0 s and the maximum displacement is 1.2 m which is far less than 1.90 m without cohesion. For unit No.5, it reaches steady-state at 22.0 s (with cohesion) and 24.0 s (without cohesion). In total, the displacement of the two units was lower by 36.8% and 23.8%



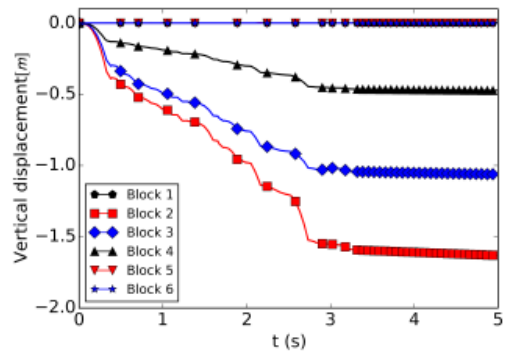
(a) Horizontal displacement for the slope $\sqrt{3}:1$



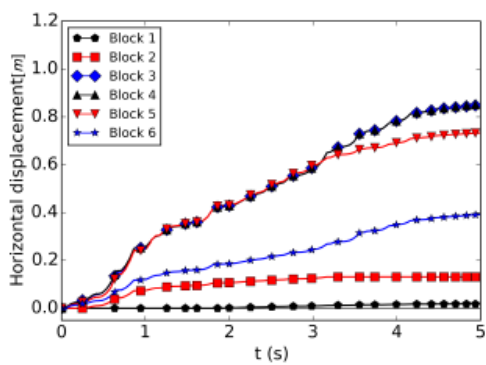
(b) Vertical displacement for the slope $\sqrt{3}:1$



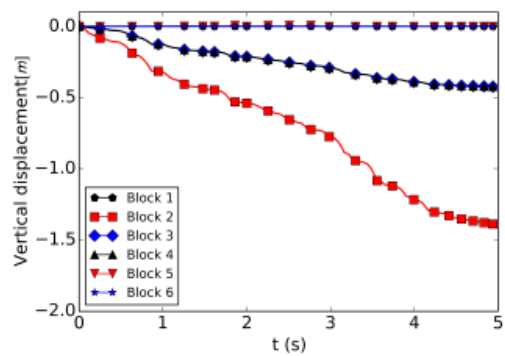
(c) Horizontal displacement for the slope 1:1



(d) Vertical displacement for the slope 1:1



(e) Horizontal displacement for the slope 1:2



(f) Vertical displacement for the slope 1:2

Figure 6.15: Standard deviations for three slopes

respectively, as compared to when cohesion is absent. Therefore, we conclude that cohesion enforces the stability of the breakwater.

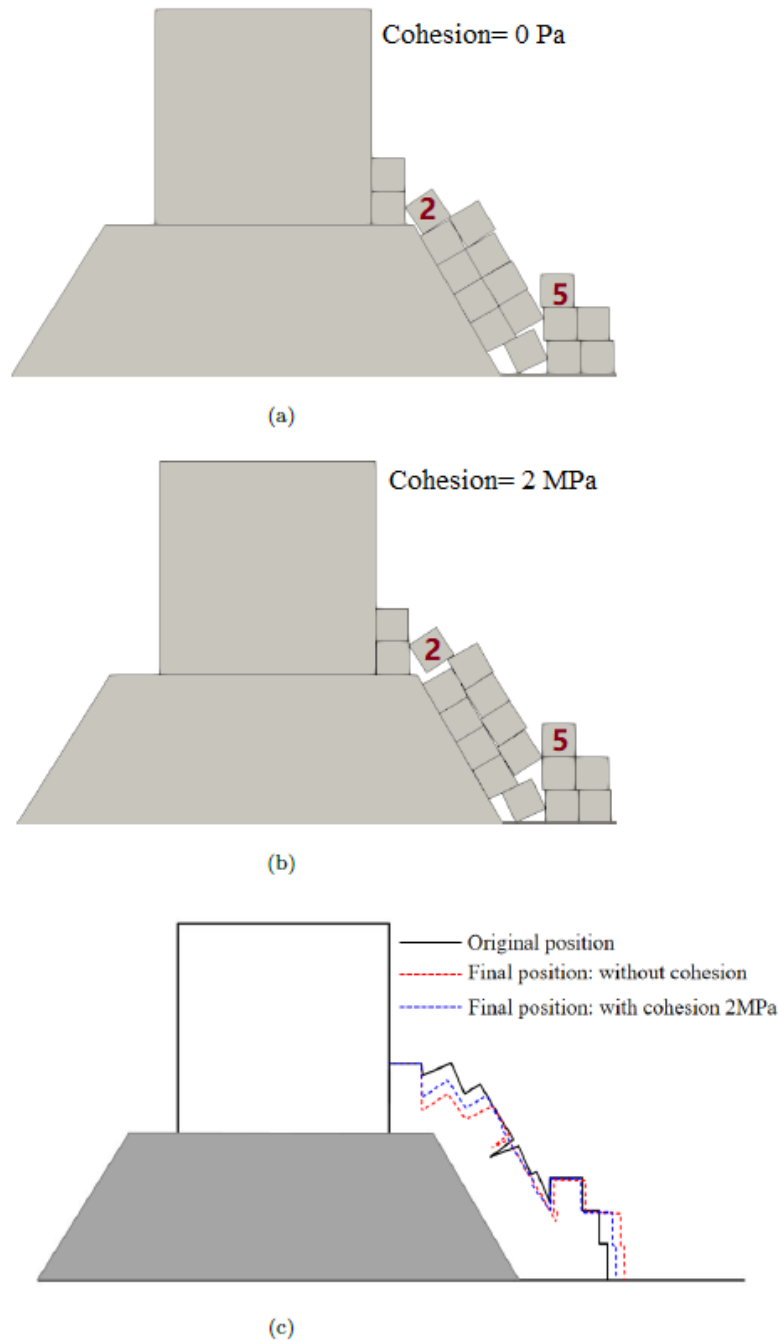


Figure 6.16: Comparison of the motion of cubic units at final position: (a) cohesion=0 Pa, tensile strength $\sigma_t = 0.7$ MPa; (b) cohesion= 2 MPa, tensile strength $\sigma_t = 0.7$ MPa; (c) Comparison of the effect of cohesion. The breakwater was subjected to solitary wave impacts whose external force is calculated by Equation (3.27) (See Figure 6.1 for the wave parameters).

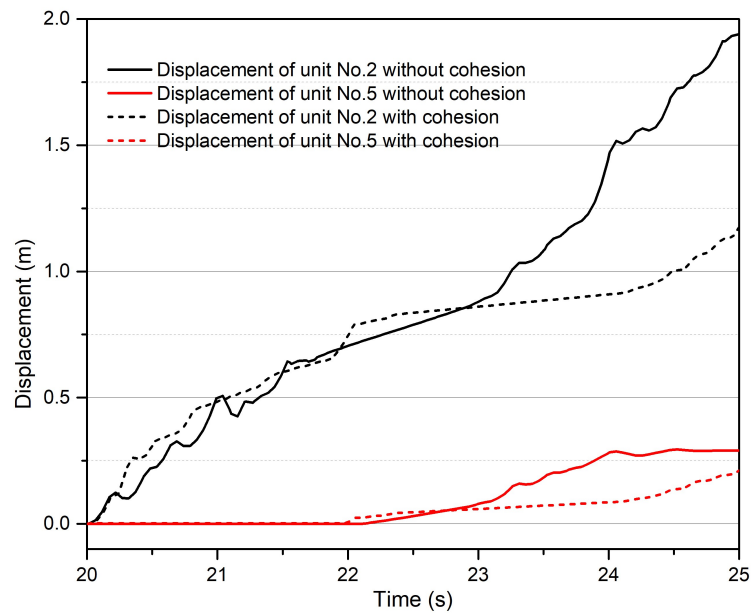


Figure 6.17: Displacement of cubic armour units 2 and 5 with and without cohesion

6.5 Concluding remarks

The stability of a caisson-type breakwater was investigated using the fluid-porous-solid triple coupled model. The fluid model was described by the Volume-Averaged Reynolds-Averaged Navier-Stokes (VARANS) equations in which the nonlinear Forchheimer equations for the porous medium were implemented as the terms of inertia. The solid model was based on the DDA method to take the discrete behavior of armor units into account. The coupling between the fluid and the solid was carried out using a strategy that transmitted the pressure of the fluid mesh nodes to the solid polygon vertices.

The results of the numerical simulation showed that the porosity and the thickness of the porous layer had a significant influence on the distribution of the kinetic energy of turbulence (TKE) around the structure of the breakwater. The greater the thickness, the lower the intensity of the TKE. Indeed, the porous layer, located just in front of the caisson, acts as a support structure that effectively dissipates and absorbs the turbulent kinetic energy of the impacting waves. It reduces the growth of wave crests and the overtopping of the caisson and also allows slope adjustment just in front of the caisson to avoid possible progressive or severe raveling of the lower part of the structure. The results of the numerical simulations also showed that the maximum impacting wave height depended on the slope of the structure of the breakwater. Thus, a new formula has been established for this purpose. Moreover, the results also showed that the shape of the armor units was a

major factor to be taken into account in the study of the stability of the structure. In particular, they showed that tetrapod-shaped units were the most stable, followed by acropod-shaped units and finally by cubic-shaped units, and that cohesion enforces the stability of the breakwater.

Validations and application for 3D-DDA

7.1 Introduction

The mathematical formula of the 3D-DDA method was presented in Chapter 4, and the corresponding 3D-DDA code will be verified by comparing the analytical results and 2D results through three classic examples in this chapter. Then, a 3D coupled fluid-structure interaction procedure will be proposed to investigate the stability of a cracked gravity dam against increasing water level. The following three effects are emphasized:

- The time intervals, interface friction angle and slope angle are studied by a model sliding on an inclined plane;
- The case of multi-blocks is verified by comparing with 2D-DDA results;
- A 3D coupled fluid-structure interaction procedure is proposed to study the gravity dam failure process;
- The effect of increasing water level and of the cohesion between blocks is investigated.

7.2 Validations

7.2.1 Case 1: Free fall

This first academic test case corresponds to the validation of the 3D-DDA method for the dynamic process. It concerns the free fall from a height $h = 10.60 \text{ m}$ of a heavy block of density $\rho = 2500 \text{ kg/m}^3$, with an acceleration of gravity: $g = 9.81 \text{ m/s}^2$ (see Figure 7.1). In this example, we set the objectives of simulating

the temporal evolution of velocity, in order to show the capacity of the developed numerical model to deal with dynamic problems.

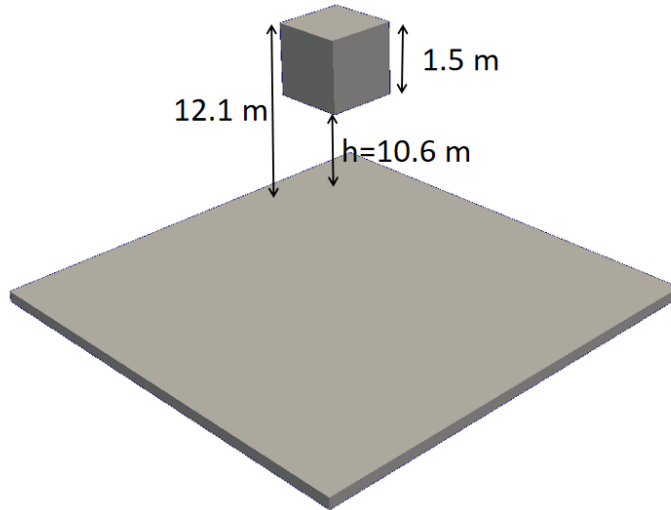


Figure 7.1: Schematic representation of a block in free fall. Falling height $h = 10.60$ m, $g = 9.81$ m/s², initial velocity $V_0 = 0$ m/s.

Figure 7.2 represents the evolution of the velocity of the block during its fall from the height h . The calculations were carried out for a period of time $T = 1.47$ second, which corresponds to the time it takes for the block to reach the ground. The comparison shows a perfect agreement between the numerical and analytical results.

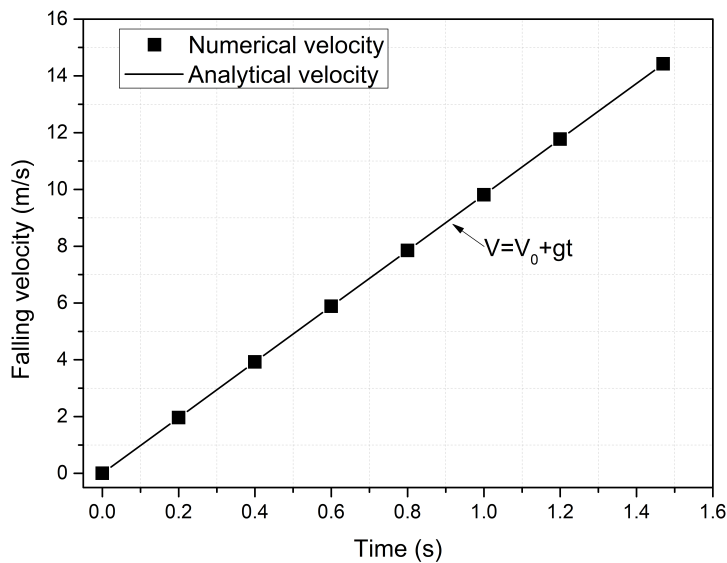


Figure 7.2: Comparison of analytical and numerical velocities. Falling height $h = 10.60$ m, $g = 9.81$ m/s², initial velocity $V_0 = 0$ m/s.

7.2.2 Case 2: Sliding on an inclined plane

A classic dynamics example is used to verify the behavior of a block on an inclined plane [170, 171], as shown in Figure 7.3, the slope angle, the friction angle, and the time integration are studied in this case. The model consists of two blocks, in which the bottom block is fixed and the upper block will accelerate and slides down on the slope due to the gravity loading. The material constants of the two blocks are: Young's modulus $E= 3000 \text{ Pa}$, Poisson ratio $\nu= 0.25$, gravity $g= 9.81 \text{ m/s}^2$, and the normal and shear contact spring stiffness $k_n=k_s= 50000 \text{ N/m}$. Under the action of gravity, the displacement $s(t)$ and velocity $v(t)$ of the block are analytically determined as a function of time t , given as:

$$\begin{aligned} s(t) &= \frac{1}{2}at^2 = \frac{1}{2}(g \sin \alpha - g \cos \alpha \tan \phi)t^2 \\ v(t) &= at = (g \sin \alpha - g \cos \alpha \tan \phi)t \end{aligned} \quad (7.1)$$

where α is the slope angle and ϕ is the friction angle.

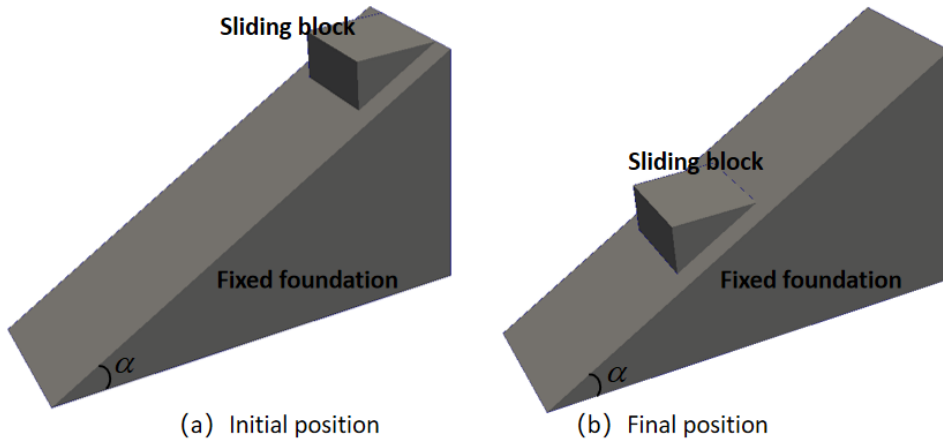


Figure 7.3: (a) Initial and (b) final positions of sliding model. $\alpha = 30^\circ$, $\phi=0$.

Three time intervals: 0.1s, 0.01s and 0.001s are used to verify the time step convergence at the sliding block. Figure 7.4 shows that the results of the three-time step cases are all reasonable. The maximum relative errors for the three time intervals are 1.4%, 0.56%, and 0.018%, respectively. This verifies that the DDA results match the analytical limit equilibrium solutions at different time intervals, while smaller time steps have better accuracy.

Three cases of friction angles, 0° , 10° and 20° , are investigated in this validation. The accumulated displacements and velocities are calculated by Equation (7.1). The variation of the velocity and displacement for different interface friction angles are

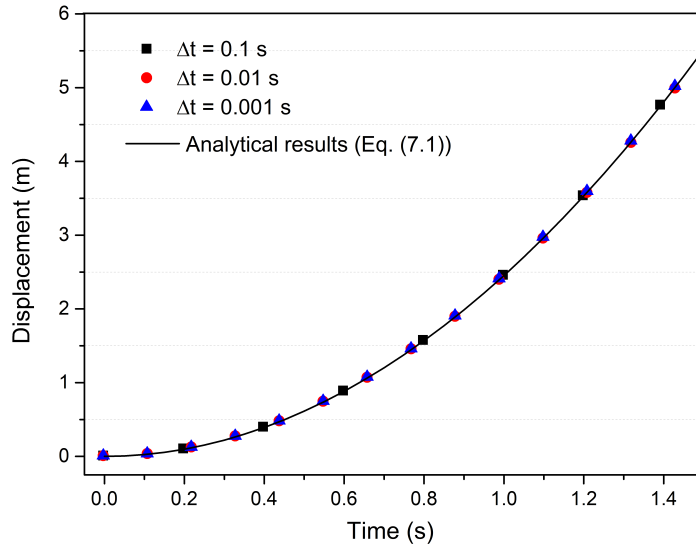


Figure 7.4: Time step convergence at the sliding block. Slope angle $\alpha = 30^\circ$, friction angle $\phi = 0^\circ$, time interval $\Delta t = 0.1s, 0.01s$ and $0.001s$, respectively. Analytical results calculated by the Equation (7.1).

shown in Figure 7.6, which verifies that the DDA results show a good agreement with the analytical solutions (see Equation (7.1)).

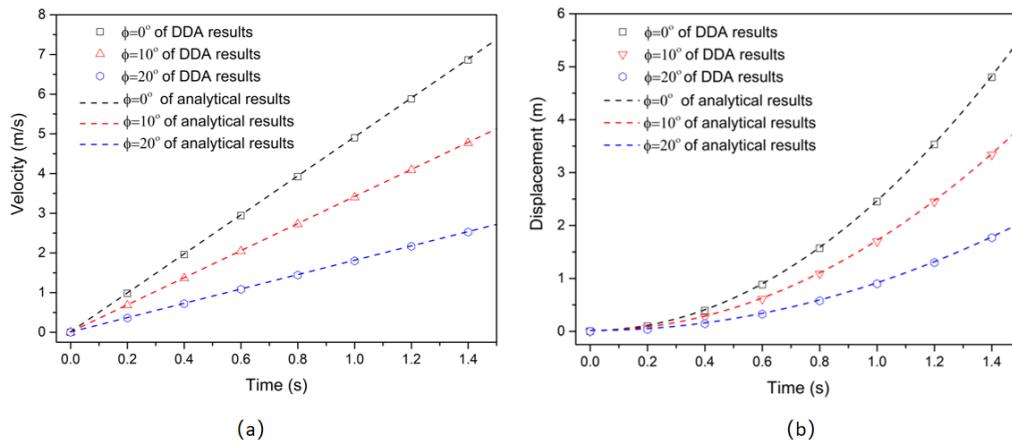


Figure 7.5: Variation of the (a) velocity and (b) displacement for different interface friction angles. Slope angle $\alpha = 30^\circ$, friction angle $\phi = 0^\circ, 10^\circ$ and 20° , respectively, time interval $\Delta t = 0.01 s$. Analytical results calculated by the Equation (7.1).

The slope incline angles also can affect the displacement and velocity of the sliding block by changing the acceleration along the sliding plane (see Equation (7.1)). Three different slope incline angles: $\alpha = 15^\circ, 30^\circ$ and 45° are studied. The variation

of the velocity and displacement for different slope incline angles is shown in Figure 7.6. The comparison between the 3D-DDA and analytical results in different cases validates the accuracy and applicability of the DDA method.

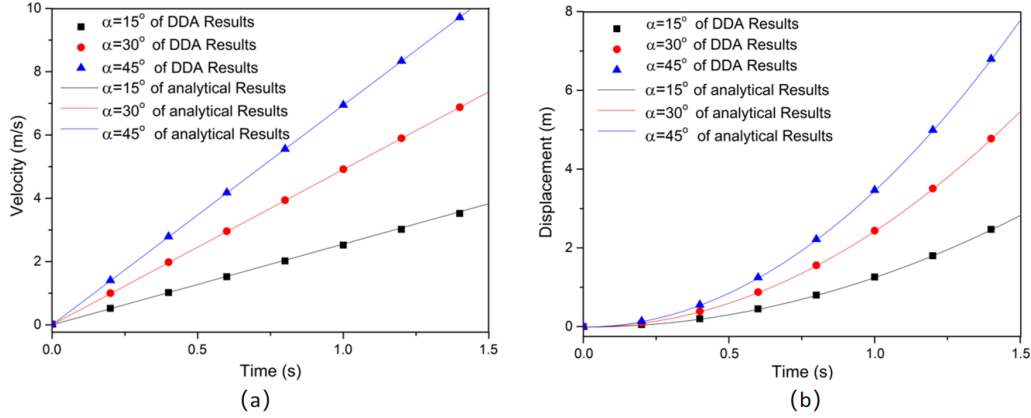


Figure 7.6: Variation of the (a) velocity and (b) displacement for different slope incline angles. Slope angle $\alpha = 15^\circ, 30^\circ$ and 45° , respectively, friction angle $\phi = 0^\circ$, time interval $\Delta t = 0.01$ s. Analytical results calculated by the Equation (7.1)

7.2.3 Case 3: Multi-blocks under gravity loading

The 3D-DDA method also can be valid by comparing with the 2D-DDA results. A multi-block structure model similar to an arch bridge is established, in which the outer sides of the arch blocks at both ends are fixed, and each block is only subject to its own weight. The material constants of all rock blocks are: unit mass $M = 20$ Kg/m^3 , Young's modulus $E = 5e5$ Pa, Poisson's ratio $\nu = 0.2$, the friction angle $\phi = 0^\circ$ and cohesion $C_f = 0$ Pa. Figure 7.7 (a) and (b) are the three-dimensional and two-dimensional calculation results at initial and final position ($\Delta t = 0.01$ s, time steps = 60). The characteristic of this example is that the geometrical configuration, load and fixed points of the block arch are all symmetrical, and all calculation results are also symmetrical.

The velocity and displacement of the marked point which is the centroid of the middle block are shown in Figure 7.8 and Figure 7.9. We can know that the three-dimensional and two-dimensional results are highly consistent, the maximum relative errors of velocity and displacement are 3.8% and 1.7%, respectively.

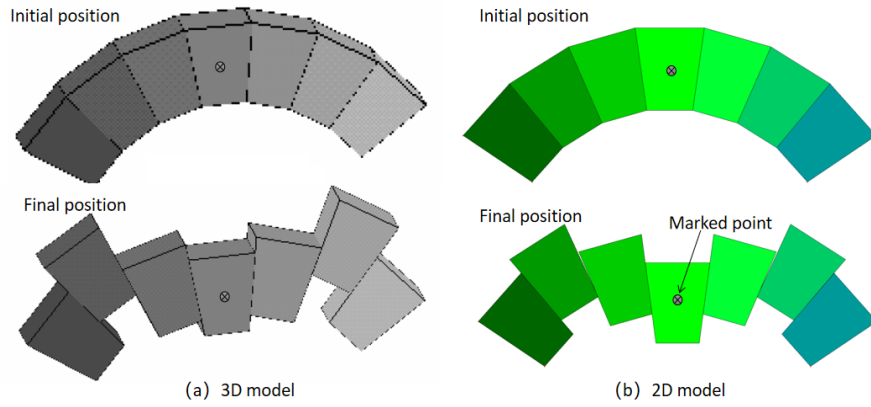


Figure 7.7: Multi-blocks model under gravity loading. $\Delta t = 0.01$ s, time steps = 60.

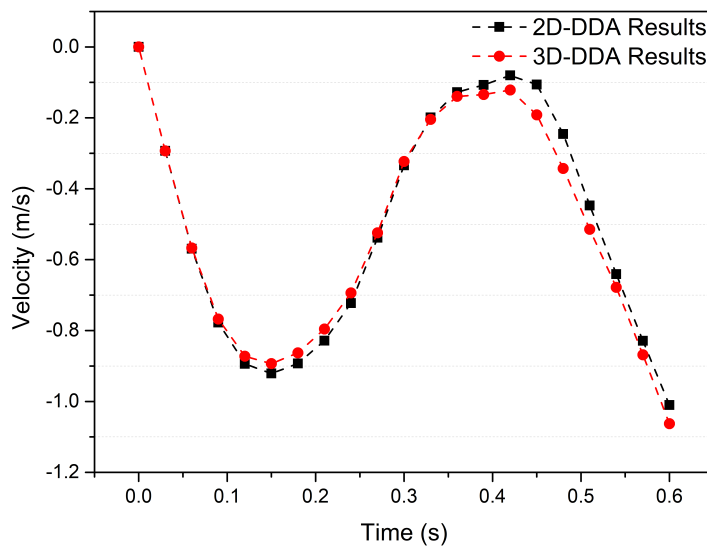


Figure 7.8: Comparison of 2D and 3D velocity at marked point

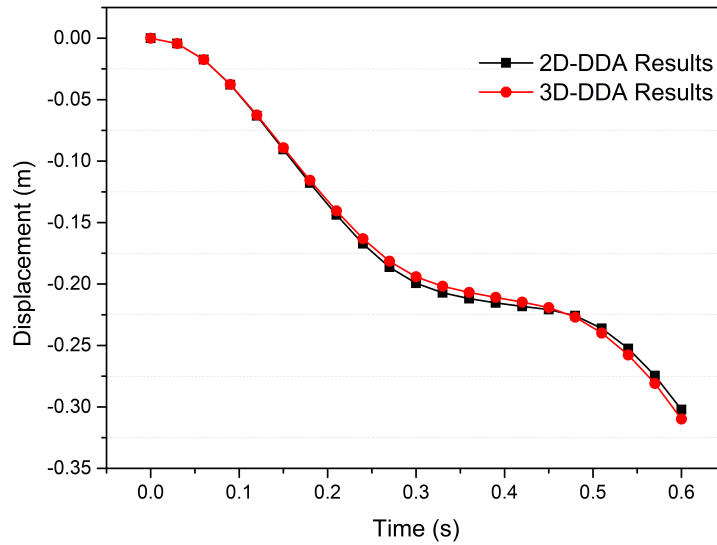


Figure 7.9: Comparison of 2D and 3D displacement at marked point

7.3 Application: gravity dam failure

7.3.1 Numerical model

In this section, we propose a 3D coupled fluid-solid coupling procedure to evaluate the stability of a cracked gravity dam when the water level rises. In this process, the gravity dam is assumed to be a discontinuous structure containing pre-existing cracks. The fluid is assumed to be calm and stable water without violent waves [172, 173].

The properties of concrete gravity dam are: unit mass $M = 2500 \text{ Kg}/\text{m}^3$, Young's modulus $E = 50 \text{ GPa}$, Poisson's ratio $\nu = 0.2$, the friction angle $\phi = 30^\circ$ and cohesion $C_f = 0.3 \text{ MPa}$, while the Fluid density is $\rho = 1000 \text{ Kg}/\text{m}^3$. The geometric of gravity dam and pre-crack position are shown in Figure 7.10.

7.3.2 Fluid-structure coupling

The coupling procedure occurs between the fluid and solid interface, as shown in Figure 7.11, which includes a transmission solution that transfers the fluid pressure to solid vertexes. The pressure exerted upon the dam is assumed to be purely hydrostatic, which can be calculated by [174]:

$$P = P_0 + \rho gh \quad (7.2)$$

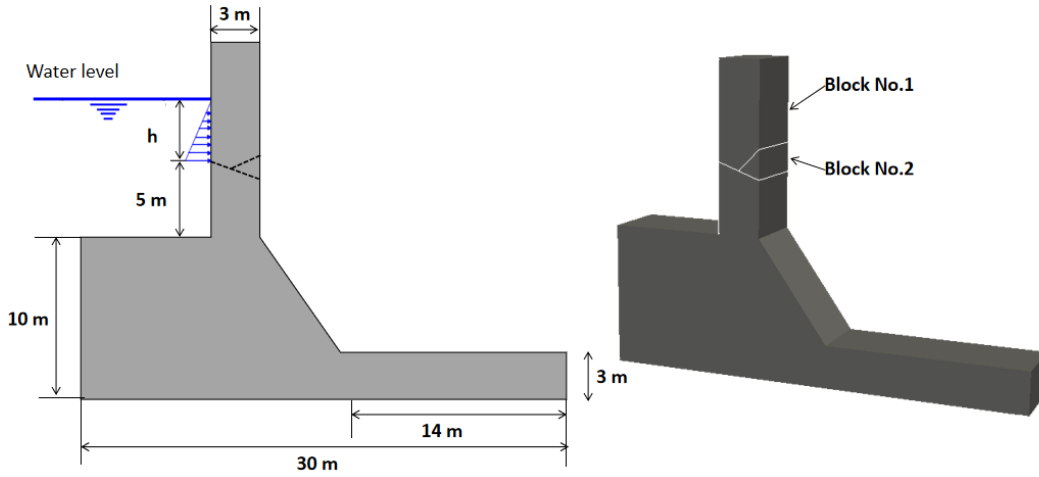


Figure 7.10: Numerical model of gravity dam with pre-existing cracks

where P is the fluid pressure acting on gravity dam at water depth h above the crack position, P_0 is the fluid pressure at crack position. As the height of the water increases, and the corresponding pressure p_i of all cells in the interface is calculated. p_i can then be converted into an external load applied to the boundary of the structure. This process is repeated several times until the dam failure reached. The force on the cells is written as:

$$f_i = p_i s_i \quad (7.3)$$

where p_i is the fluid pressure at cell i , and s_i is the surface of the cell i . Finally, the global forces (F_1, F_2, F_3, F_4) acting on the DDA block, as shown in Figure 7.11, can be represented as:

$$\begin{aligned} F_1 &= \sum_{i=1}^n \left[f_i \left(\frac{d_{i4}}{d_{i1} + d_{i4}} \right) n_y \right] \left(\frac{d_{i2}}{d_{i1} + d_{i2}} \right) n_z = \sum_{i=1}^n f_i \left(\frac{d_{i2} n_z d_{i4} n_y}{RL} \right) \\ F_2 &= \sum_{i=1}^n \left[f_i \left(\frac{d_{i3}}{d_{i2} + d_{i3}} \right) n_y \right] \left(\frac{d_{i1}}{d_{i2} + d_{i3}} \right) n_z = \sum_{i=1}^n f_i \left(\frac{d_{i1} n_z d_{i3} n_y}{RL} \right) \\ F_3 &= \sum_{i=1}^n \left[f_i \left(\frac{d_{i2}}{d_{i2} + d_{i3}} \right) n_y \right] \left(\frac{d_{i4}}{d_{i3} + d_{i4}} \right) n_z = \sum_{i=1}^n f_i \left(\frac{d_{i2} n_y d_{i4} n_z}{RL} \right) \\ F_4 &= \sum_{i=1}^n \left[f_i \left(\frac{d_{i1}}{d_{i1} + d_{i4}} \right) n_y \right] \left(\frac{d_{i3}}{d_{i3} + d_{i4}} \right) n_z = \sum_{i=1}^n f_i \left(\frac{d_{i1} n_y d_{i3} n_z}{RL} \right) \end{aligned} \quad (7.4)$$

where n is the total number of cells on the face, d_{i1}, d_{i2}, d_{i3} and d_{i4} are the distance from the given cell centroid to vertex 1, 2, 3 and 4. n_y and n_z represent the unit vector of y and z direction.

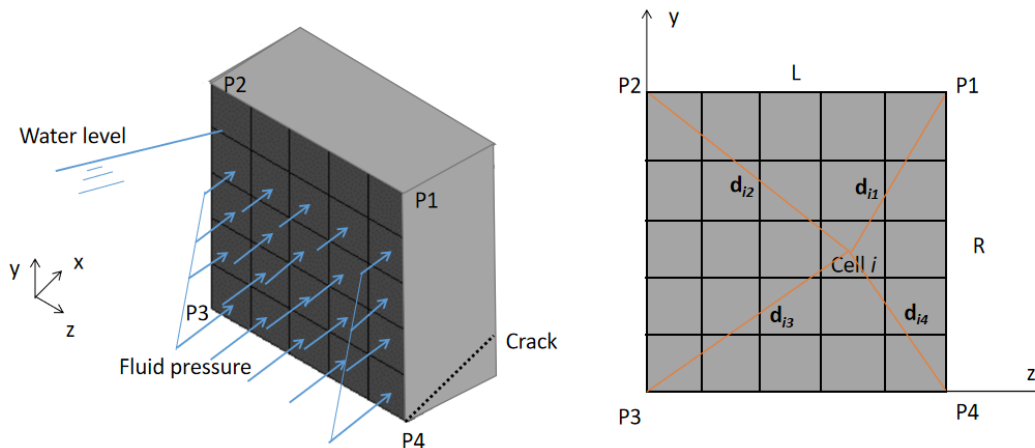


Figure 7.11: Fluid-solid interface.

7.3.3 Simulation results

7.3.3.1 Effect of water level

In order to estimate the relationship between dam failure and water level, the water level gradually increases above the fracture area until structural failure occurs. According to the coupling process between fluid and solid, the forces acting on the gravity dam can be calculated by Equation (7.4). Figure 7.12 shows the time-depending forces exerted on the vertexes of the gravity dam with pre-existing cracks. The results indicate that when the water reaches a height of 4 m above the fracture zone, the pressure limit has been reached, the failure happens.

The failure behavior of the gravity dam is shown in Figure 7.13. It follows that the falling blocks trajectories and displacement show that its movement may be divided into three phases. The first phase sited between $t=0\text{ s}$ and $t=7.5\text{ s}$ corresponds to a sliding state of the blocks move along the crack due to the water pressure. The second phase sited between $t=7.5\text{ s}$ and $t=15.0\text{ s}$ corresponds to falling processes in which the blocks fall into the bottom foundation. The third phase sited after $t=15.0\text{ s}$ corresponds to the stable state. It should be mentioned that the severity and the duration of every phase strongly depend on the initial water pressure.

Figure 7.14 and Figure 7.15 show the variation of displacement of blocks No. 1 and No. 2 for three different water levels. The increased water level induces early movement and may cause large displacement, which results in a more serious consequence.

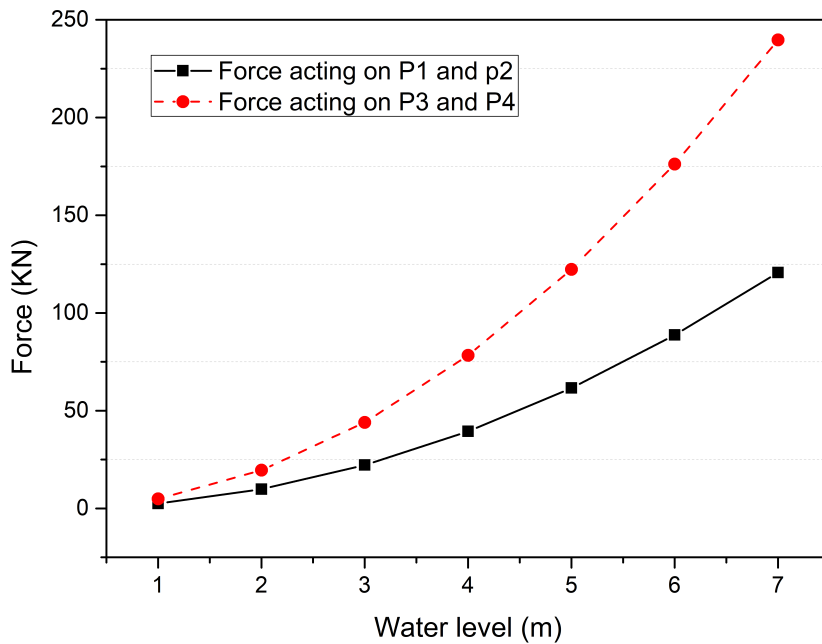


Figure 7.12: Fluid force acting on solid vertex calculated by Equation (7.4).

7.3.3.2 Effect of cohesion

For concrete dams, cohesive strength usually accounts for a large part of the total shear strength of the partially bonded concrete-rock interface [175, 176]. Parts with high and low cohesion values may appear in clusters with a certain relative distance. The reason is that the bond strength depends on many factors, such as the result of cleaning the rock surface before concrete casting, local rock quality and the location of the leak and other degradation processes. In order to investigate the influence of the cohesion over the concrete-rock interface on gravity dam failure stability, three values of cohesion employed in the numerical model and the variation of displacement of block No. 1 for different cohesion are shown in Figure 7.16. There is a significant difference between the displacement with and without cohesion. By comparing the results of 3 MPa with 0 MPa, the displacement has a 16.7 % reduction, and the movement 5.5 s earlier. Therefore, we can conclude that cohesion improves the stability of the gravity dam.

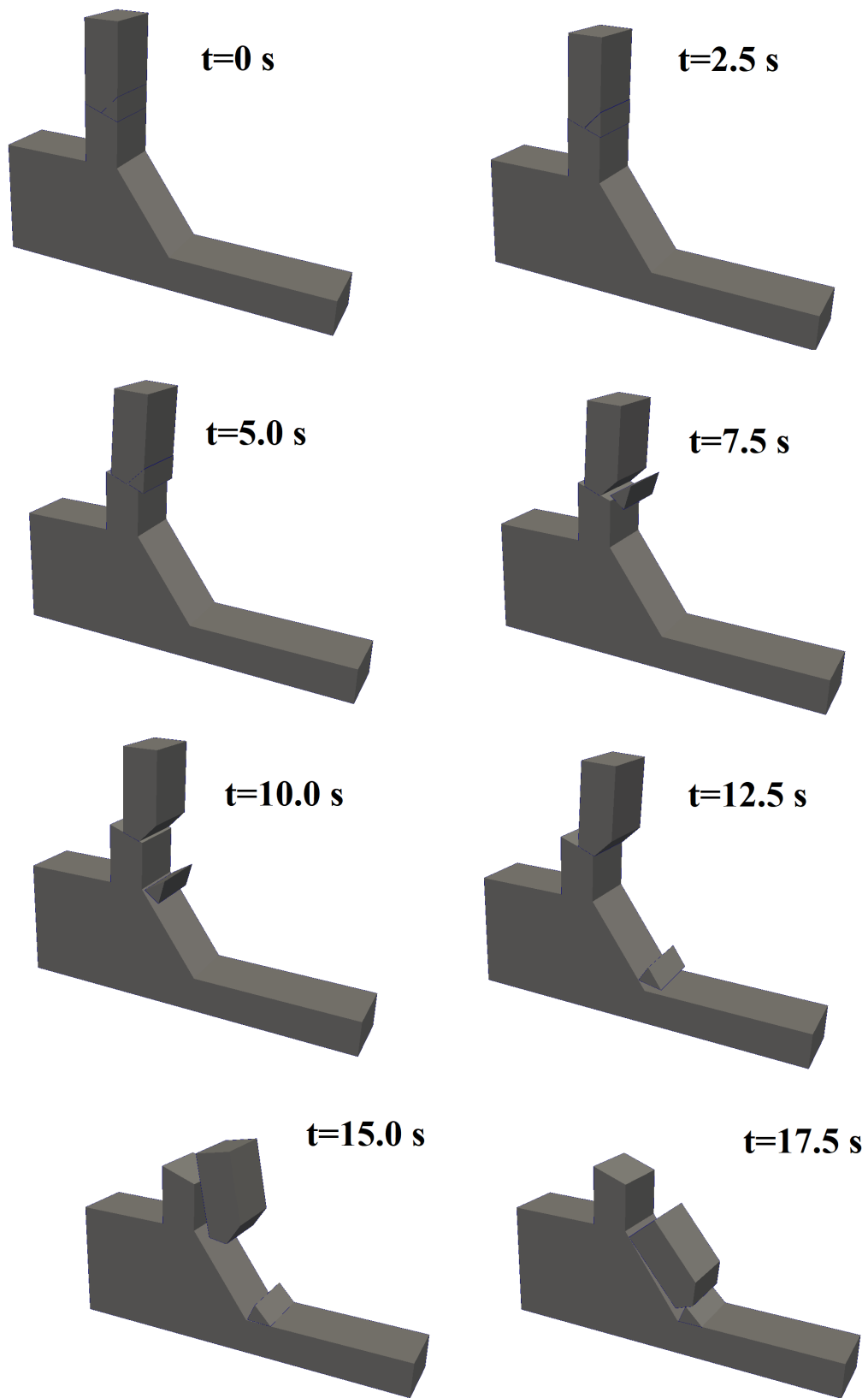


Figure 7.13: Failure behavior of the gravity dam; water height above the cracks $h = 4.0 \text{ m}$.

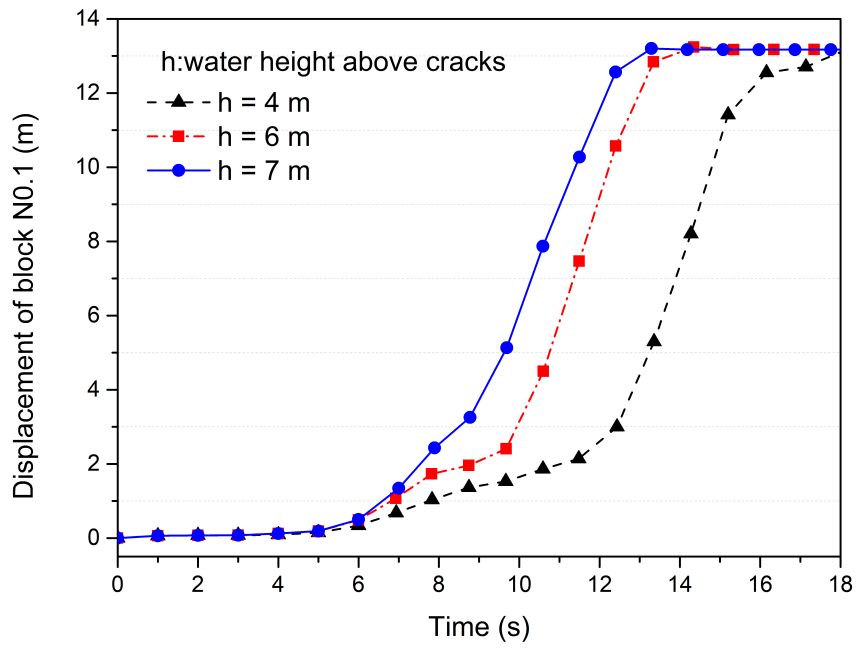


Figure 7.14: Variation of displacement of block No. 1 for three water levels.

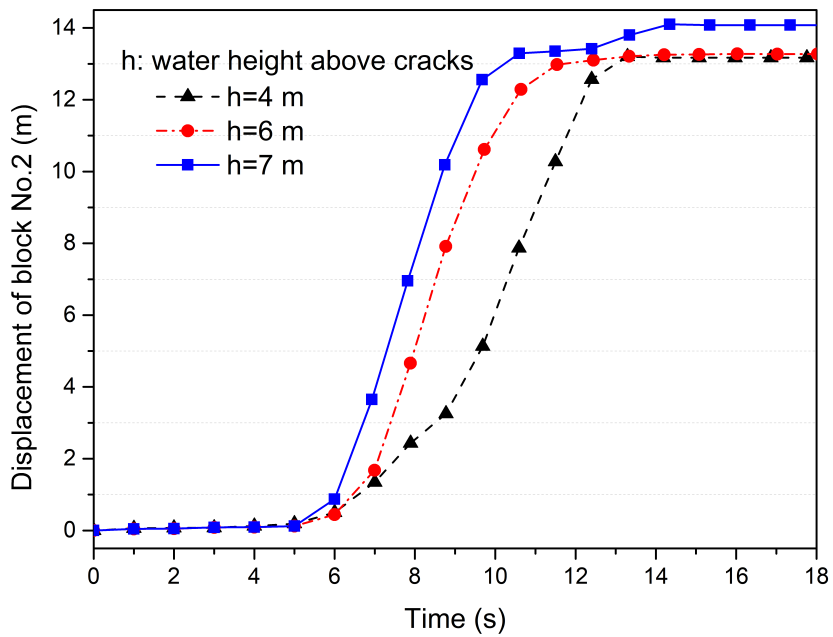


Figure 7.15: Variation of displacement of block No. 2 for three water levels.

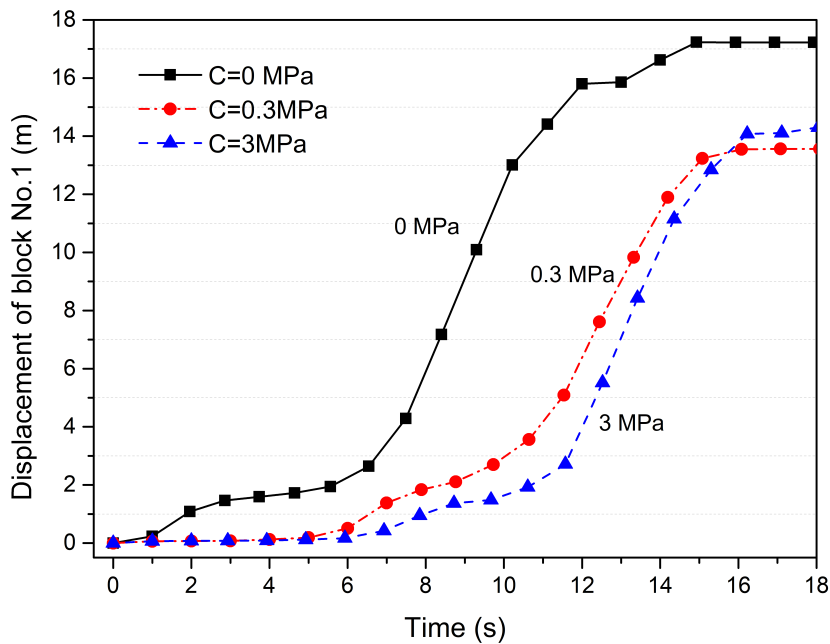


Figure 7.16: Variation of displacement of block No. 1 for different cohesion, water height above the cracks $h = 4.0 \text{ m}$.

7.4 Concluding remarks

In this chapter, the 3D-DDA method was verified by comparing the analytical results and 2D results of three classic examples. Then, a 3D coupled fluid-structure interaction procedure was proposed to study the stability of a cracked gravity dam against increasing water level. The effect of the water level and the cohesion between the blocks was investigated.

- The validation of the 3D-DDA method was done by comparing the numerical results with the analytical results. The time intervals, interface friction angle and slope angle were investigated by sliding on an inclined plane compared with analytical results. The case of multi-blocks was verified by comparing with 2D-DDA results.
- The 3-D coupling procedure between the fluid and solid interface was proposed, which included a transmission solution that transferred the fluid pressure to solid vertexes.
- The effect of increasing the water level and cohesion between the blocks was studied. The results showed that the increased water level induced early

movement and might cause large displacement, which could result in a more serious consequence. The cohesion improved the stability of the gravity dam.

Conclusions and future work

8.1 Conclusions

Discontinuous environmental problems were investigated based on the DDA method. The brief theory of 2D-DDA was introduced and a 2D fluid and solid coupling approach was proposed, wherein the fluid model was described by the Volume-Averaged Reynolds-Averaged Navier-Stokes (VARANS) equations and the solid model was based on the DDA method. Furthermore, the mathematical formulations of 3D-DDA were introduced in detail and the corresponding code was programmed and verified. The DDA method was used on ballast flight, breakwater and cracked gravity dam.

The dynamic behavior of ballast stones and their collision with a snow / ice block were studied using 2D-DDA. The shapes of the ice blocks and the contacts between ballast particles were taken into account. The ballast flight induced by the dropping snow / ice with some variations in intensity depended on the velocity, the incident angle and the shapes of the ice blocks. Hence, setting the maximum operating speed according to the weather conditions is an effective measure to reduce serious consequences. It is noteworthy that in order to significantly reduce the ballast flight caused by the melting of snow / ice blocks, some measures should be taken to prevent snow accumulation in the train and snow settlement.

The stability of a caisson-type breakwater was investigated using the fluid-porous-solid triple coupled model. The fluid model was described by the Volume-Averaged Reynolds-Averaged Navier-Stokes (VARANS) equations in which the nonlinear Forchheimer equations for the porous medium were implemented as the terms of inertia. The solid model was based on the DDA method to take the discrete behavior of armor units into account. The coupling between the fluid and the solid was carried out using a strategy that transmitted the pressure of the fluid mesh nodes to the solid polygon vertices. The results of the numerical simulation showed that the porosity

and the thickness of the porous layer had a significant influence on the distribution of the kinetic energy of turbulence (TKE) around the structure of the breakwater. The greater the thickness, the lower the intensity of the TKE. Moreover, the results also showed that the shape of the armor units was a major factor to be taken into account in the study of the stability of the structure. In particular, they showed that tetrapod-shaped units were the most stable, followed by acropod-shaped units and finally by cubic-shaped units, and that cohesion enforces the stability of the breakwater.

The 3D-DDA method was verified by comparing the analytical results and the 2D results of three classic examples. A 3D coupled fluid-structure interaction procedure was then proposed to study the stability of a cracked gravity dam against increasing water level. The effect of increasing the water level and cohesion between the blocks was studied. The results showed that the increased water level induced early movement and might cause large displacement, which could result in a more serious consequence. The cohesion improved the stability of the gravity dam.

8.2 Future work

To augment the numerical and engineering contributions of this thesis, several improvements are recommended:

- The common-plane method used in the 3D-DDA method can economize on calculations; however, it cannot be used to judge the contact between concave polyhedrons. A highly efficient, universal and suitable contact judgment algorithm should be proposed.
- The 3D fluid and solid coupling procedure were carried out to study purely hydrostatic contexts. A general coupling method should therefore be proposed if studying hydrodynamic problems is intended.
- Other numerical techniques, such as FEM, SPH, CFD, etc., can be developed and coupled with the 2D or 3D DDA method, which will expand the applicability of the DDA method.

With these improvements, the DDA method should be able to simulate more conditions for various environmental problems. The simulation results can be greatly improved for better predictions of their physics.

Bibliography

- [1] JA Hudson. *Engineering Rock Mechanics: Part 2: Illustrative Worked Examples*. Elsevier, 2001.
- [2] MS Khan. *Investigation of discontinuous deformation analysis for application in jointed rock masses*. PhD thesis, Department of Civil Engineering University of Toronto, 2010.
- [3] RE Goodman, RL Taylor, and TL Brekke. A model for the mechanics of jointed rock. *Journal of Soil Mechanics & Foundations Div*, 14(3):637–659, 1968.
- [4] BC Burman. Development of a numerical model for discontinua. *Australian Geomechanics Journal*, 4(1):13–22, 1974.
- [5] V Sarhosis, K Bagi, J Lemos, and G Milani. *Computational modeling of masonry structures using the discrete element method*. IGI Global, 2016.
- [6] Y Jiao, X Zhang, H Zhang, H Li, S Yang, and J Li. A coupled thermo-mechanical discontinuum model for simulating rock cracking induced by temperature stresses. *Computers and Geotechnics*, 67:142–149, 2015.
- [7] G Huang, P Kulatilake, S Shreedharan, and S Cai. 3-D discontinuum numerical modeling of subsidence incorporating ore extraction and backfilling operations in an underground iron mine in China. *International Journal of Mining Science and Technology*, 27(2):191–201, 2017.
- [8] PA Cundall. A computer model for simulating progressive, large-scale movement in blocky rock system. In *Proceedings of the International Symposium on Rock Mechanics, 1971*, pages 1–8, 1971.
- [9] G-H Shi. Discontinuous deformation analysis: a new numerical model for the statics and dynamics of deformable block structures. *Engineering computations*, 9(2):157–168, 1992.
- [10] Y H Hatzor, G Ma, and G-h Shi. *Discontinuous Deformation Analysis in Rock Mechanics Practice*. CRC Press, 2017.

- [11] YH Hatzor, AA Arzi, and M Tsesarsky. Realistic dynamic analysis of jointed rock slopes using DDA. In *Proceedings of 5th International Conference on Analysis of Discontinuous Deformation*, 2002.
- [12] DM Doolin and Nicholas Sitar. Time integration in discontinuous deformation analysis. *Journal of engineering mechanics*, 130(3):249–258, 2004.
- [13] PA Cundall. Distinct element models of rock and soil structure. *Analytical and computational methods in engineering rock mechanics*, pages 129–163, 1987.
- [14] MM MacLaughlin and DM Doolin. Review of validation of the discontinuous deformation analysis (DDA) method. *International journal for numerical and analytical methods in geomechanics*, 30(4):271–305, 2006.
- [15] X Dong and WU AQ. A preliminary application of discontinuous deformation analysis (DDA) to the three gorges project on Yangtze River, China. In *Proceedings of the first international forum on discontinuous deformation analysis (DDA) and simulations of discontinuous media, Berkeley, USA*, pages 310–317, 1996.
- [16] MM MacLaughlin and RD Langston. Discrete element analysis of a mine stope in blocky rock: a comparison study of DDA and UDEC. In *Proceedings of the Fourth International Conference on Analysis of Discontinuous Deformation*, pages 111–120. University of Glasgow Glasgow, 2001.
- [17] G Yagoda-Biran. *Seismic Hazard Analysis Using the Numerical DDA Method*. PhD thesis, Ben-Gurion University of the Negev, 2013.
- [18] G Yagoda-Biran and YH Hatzor. Benchmarking the numerical discontinuous deformation analysis method. *Computers and Geotechnics*, 71:30–46, 2016.
- [19] A McBride and F Scheele. Investigation of discontinuous deformation analysis using physical laboratory models. In *Proc. Fourth International Conference on Discontinuous Deformation Analysis*, pages 73–82, 2001.
- [20] P Cundall, M Voegele, C Fairhurst, et al. Computerized design of rock slopes using interactive graphics for the input and output of geometrical data. In *The 16th US Symposium on Rock Mechanics (USRMS)*. American Rock Mechanics Association, 1975.
- [21] T Ishikawa, Y Ohnishi, and A Namura. DDA applied to deformation analysis of coarse granular materials (ballast). *Proc. 2nd Int. Conf. on Analysis of Discontinuous Deformation. Japan Institute of Systems Research: Kyoto*,

Japan, pages 253–262, 1997.

- [22] D Ding, A Ouahsine, W Xiao, and P Du. Numerical study of ballast-flight caused by dropping snow/ice blocks in high-speed railways using Discontinuous Deformation Analysis (DDA). *Transportation Geotechnics*, 22:100314, 2020.
- [23] DM Doolin and N Sitar. Displacement accuracy of discontinuous deformation analysis method applied to sliding block. *Journal of engineering mechanics*, 128(11):1158–1168, 2002.
- [24] M MacLaughlin, N Sitar, D Doolin, and T Abbot. Investigation of slope-stability kinematics using discontinuous deformation analysis. *International journal of rock mechanics and mining sciences*, 38(5):753–762, 2001.
- [25] MM MacLaughlin, N Sitar, et al. Kinematics of sliding on a hinged failure surface. In *Proceedings of 2nd North American Rock Mechanics Symposium*. American Rock Mechanics Association, 1996.
- [26] O Yuzo, Chen G, and Miki S. Recent development of DDA in rock mechanics practice. In *The First International Conference on Analysis of Discontinuous Deformation*, pages 26–47, Changli, Taiwan, 1995.
- [27] TC Ke. The issue of rigid body rotation in DDA. In *Proceedings of first international forum on discontinuous deformation analysis (DDA) and simulations of discontinuous media*, pages 18–25. Berkeley, 1996.
- [28] CY Koo, JC Chern, and S Chen. Development of second order displacement function for DDA. In *Proceedings of the first international conference on analysis of discontinuous deformation*. National Central University: Chungli, Taiwan ROC, pages 91–108, 1995.
- [29] TC Ke. Application of DDA to simulate fracture propagation in solid. In *Proceedings of the Second International Conference on Analysis of Discontinuous Deformation*, Kyoto, Japan, pages 9–12, 1997.
- [30] DM Doolin and N Sitar. Accuracy of the DDA method for frictionless impact. In *Mining and Tunnelling Innovation and Opportunity, North American Rock Mechanics Symposium-Tunneling Association of Canada*, pages 1289–1296, 2002.
- [31] K Shyu, X Wang, and CT Chang. Dynamic behaviors in discontinuous elastic media using DDA. In *Proceedings of the Third International Conference on Analysis of Discontinuous Deformation from Theory to Practice*, pages 243–

252, 1999.

- [32] D Stewart. Time-stepping methods and the mathematics of rigid body dynamics. *Impact and Friction of Solids, Structures and Machines*, 1, 2000.
- [33] R Kamai. *Estimation of historical seismic ground-motions using back analysis of structural failures in archaeological sites*. Ben-Gurion University of the Negev, 2006.
- [34] S Kaidi, A Ouahsine, P Sergent, and M Rouainia. Analyse des deformations discontinues pour l'évaluation de la stabilité des digues en enrochements sous chargement sismique. *Comptes Rendus Mécanique*, 340(10):731–738, 2012.
- [35] CY Wang, CC Chuang, and Jopan Sheng. Time integration theories for the DDA method with finite element meshes. In *Proceedings of 1st Int. Forum on Discontinuous Deformation Analysis (DDA) and Simulations of Discontinuous Media*, pages 263–287. New Mexico, USA, 1996.
- [36] P Komodromos, L Papaloizou, and P Polycarpou. Simulation of the response of ancient columns under harmonic and earthquake excitations. *Engineering Structures*, 30(8):2154–2164, 2008.
- [37] MM MacLaughlin and KK Clapp. Discrete element analysis of an underground opening in blocky rock: an investigation of the differences between UDEC and DDA results. In *Discrete Element Methods: Numerical Modeling of Discontinua*, pages 329–334. 2002.
- [38] AT McBride and F Scheele. Validation of discontinuous deformation analysis using a physical model. *Structural Engineering, Mechanics and Computation*, pages 719–726, 2001.
- [39] K Irie, T Koyama, S Nishiyama, Y Yasuda, and Y Ohnishi. A numerical study on the effect of shear resistance on the landslide by discontinuous deformation analysis (DDA). *Geomechanics and Geoengineering*, 7(1):57–68, 2012.
- [40] MM MacLaughlin and N Sitar. Rigid body rotations in DDA. In *Proceedings of the first international forum on discontinuous deformation analysis (DDA) and simulation of discontinuous media, Berkeley*, pages 620–635, 1996.
- [41] YM Cheng and YH Zhang. Rigid body rotation and block internal discretization in DDA analysis. *International Journal for Numerical and Analytical Methods in Geomechanics*, 24(6):567–578, 2000.

- [42] CY Koo and Jin-Ching Chern. Modification of the DDA method for rigid block problems. *International Journal of Rock Mechanics and Mining Sciences*, 35(6):683–693, 1998.
- [43] CY Koo and JC Chern. The development of dda with third order displacement function. In *Proceedings of the First International Forum on Discontinuous Deformation Analysis (DDA) and Simulations of Discontinuous Media*, pages 12–14. Berkeley, CA. TSI Press: Albuquerque, 1996.
- [44] Max Y Ma, M Zaman, and JH Zhou. Discontinuous deformation analysis using the third order displacement function. In *Proceedings of the First International Forum on Discontinuous Deformation Analysis (DDA) and Simulations of Discontinuous Media*, pages 383–394. Berkeley, CA. TSI Press: Albuquerque, 1996.
- [45] SM Hsiung. Discontinuous deformation analysis (DDA) with nth order polynomial displacement functions. In *DC Rocks 2001, The 38th US Symposium on Rock Mechanics (USRMS)*. American Rock Mechanics Association, 2001.
- [46] XB Wang, XL Ding, B Lu, and A Wu. DDA with higher order polynomial displacement functions for large elastic deformation problems. In *Proceedings of the 8th International Conference on the analysis of discontinuous deformation, Beijing, China*, pages 89–94, 2007.
- [47] TC Ke and J Bray. Modeling of particulate media using discontinuous deformation analysis. *Journal of engineering mechanics*, 121(11):1234–1243, 1995.
- [48] P Wriggers and G Zavarise. Computational contact mechanics. *Encyclopedia of computational mechanics*, 2004.
- [49] P Papadopoulos and JM Solberg. A lagrange multiplier method for the finite element solution of frictionless contact problems. *Mathematical and computer modelling*, 28(4-8):373–384, 1998.
- [50] T Belytschko and M Neal. Contact-impact by the pinball algorithm with penalty and lagrangian methods. *International Journal for Numerical Methods in Engineering*, 31(3):547–572, 1991.
- [51] B Amadei. Recent extensions to the DDA method. In *Proc. of first Int. Forum on Discontinuous Deformation Analysis (DDA), Berkley, California*, 1996.
- [52] CT Lin, B Amadei, J Jung, and J Dwyer. Extensions of discontinuous deformation analysis for jointed rock masses. *International Journal of Rock*

Mechanics and Mining Sciences, 33(7):671–694, 1996.

- [53] BK Kannan and Steven N Kramer. An augmented lagrange multiplier based method for mixed integer discrete continuous optimization and its applications to mechanical design. *Journal of mechanical design*, 116(2):405–411, 1994.
- [54] V Sarhosis, JV Lemos, and K Bagi. Discrete element modeling. In *Numerical Modeling of Masonry and Historical Structures*, pages 469–501. Elsevier, 2019.
- [55] J Eliáš. Simulation of railway ballast using crushable polyhedral particles. *Powder Technology*, 264:458–465, 2014.
- [56] M Hazay and A Munjiza. Introduction to the combined finite-discrete element method. In *Computational Modeling of Masonry Structures Using the Discrete Element Method*, pages 123–145. IGI Global, 2016.
- [57] Y Ohnishi, S Nishiyama, S Akao, M Yang, and S Miki. DDA for elastic elliptic element. In *Proceedings of the 7th International Conference on Analysis of Discontinuous Deformation*, pages 103–112, 2005.
- [58] C O’Sullivan and JD Bray. A comparative evaluation of two approaches to discrete element modeling of particulate media. In *Proc., Fourth International Conference on Discontinuous Deformation Analysis. Glasgow*, pages 6–8, 2001.
- [59] M Yang, T Fukawa, Y Ohnishi, Y Hirakawa, and S Mori. The application of 3-dimensional DDA with a spherical rigid block for rockfall simulation. *International Journal of Rock Mechanics and Mining Sciences*, 41(SUPPL. 1), 2004.
- [60] GH Shi. *Numerical Manifold Method (NMM) and Discontinuous Deformation Analysis (DDA)*. Beijing: TsingHua University Press, 1997.
- [61] YM Cheng and YH Zhang. Coupling of FEM and DDA methods. *International Journal of Geomechanics*, 2(4):503–517, 2002.
- [62] K Shyu. *Nodal-based discontinuous deformation analysis*. PhD thesis, University of California, Berkeley, 1995.
- [63] H Bao and Z Zhao. Modeling brittle fracture with the nodal-based discontinuous deformation analysis. *International Journal of Computational Methods*, 10(06):1350040, 2013.

- [64] C T Lin. *Extensions to the discontinuous deformation analysis for jointed rock masses and other blocky systems*. PhD thesis, University of Colorado, 1995.
- [65] M Rouainia, H Lewis, C Pearce, N Bicanic, Gary Douglas Couples, and Mark Andrew Reynolds. Hydro-geomechanical modelling of seal behaviour in overpressured basins using discontinuous deformation analysis. *Engineering Geology*, 82(4):222–233, 2006.
- [66] YX Ben, J Xue, QH Miao, and Y Wang. Coupling fluid flow with discontinuous deformation analysis. *Advances in Discontinuous Numerical Methods and Applications in Geomechanics and Geoengineering*, pages 107–112, 2012.
- [67] T Koyama, K Irie, K Nagano, S Nishiyama, N Sakai, and Y Ohnishi. DDA simulations for slope failure/collapse experiment caused by torrential rainfall. *Advances in Discontinuous Numerical Methods and Applications in Geomechanics and Geoengineering*, pages 119–126, 2013.
- [68] S Kaidi, M Rouainia, and A Ouahsine. Stability of breakwaters under hydrodynamic loading using a coupled DDA/FEM approach. *Ocean Engineering*, 55:62–70, 2012.
- [69] RG Mikola and N Sitar. Next generation discontinuous rock mass models: 3-D and rock-fluid interaction. *Front Discontin Numer Methods Pract Simul Eng Disaster Prev*, 12:81–90, 2013.
- [70] X Peng, P Yu, G Chen, M Xia, and Y Zhang. Development of a coupled DDA–SPH method and its application to dynamic simulation of landslides involving solid–fluid interaction. *Rock Mechanics and Rock Engineering*, pages 1–19, 2019.
- [71] W Zhu, Q Zhang, and L Jing. Stability analysis of the ship-lock slopes of the Three-Gorge project by three-dimensional FEM and DEM techniques. In *Proceedings of the Third International Conference of discontinuous deformation Analysis (ICADD-3)*. Alexandria, USA: American Rock Mechanics Association (ARMA), pages 263–72, 1999.
- [72] T Scheldt, M Lu, and A Myrvang. Numerical analysis of gjovik cavern: a comparison of continuous and discontinuous results by using phase two and DDA. In *Fifth International Conference on Analysis of Discontinuous Deformation-Stability of Rock Structures*. Rotterdam: Balkema, pages 125–

132, 2002.

- [73] JT Kottenstette. DDA analysis of the RCC modification for Pueblo Dam. In *Proceedings of Third International Conference on Analysis of Discontinuous Deformation-From Theory to Practice.: Vail Co*, pages 3–4, 1999.
- [74] YH Hatzor, AA Arzi, Y Zaslavsky, and A Shapira. Dynamic stability analysis of jointed rock slopes using the DDA method: King Herod's Palace, Masada, Israel. *International Journal of Rock Mechanics and Mining Sciences*, 41(5):813–832, 2004.
- [75] YH Hatzor et al. Dynamic rock slope stability analysis at masada national monument using block theory and DDA. *Rock Mecganics for Industry*, 1:63–70, 1999.
- [76] J-H Wu, Y Ohnishi, and S Nishiyama. A development of the discontinuous deformation analysis for rock fall analysis. *International journal for numerical and analytical methods in geomechanics*, 29(10):971–988, 2005.
- [77] G Ma, H Matsuyama, S Nishiyama, and Y Ohnishi. Practical studies on rockfall simulation by DDA. *Journal of Rock Mechanics and Geotechnical Engineering*, 3(1):57–63, 2011.
- [78] G Chen, L Zheng, Y Zhang, and J Wu. Numerical simulation in rockfall analysis: a close comparison of 2-D and 3-D DDA. *Rock mechanics and rock engineering*, 46(3):527–541, 2013.
- [79] MR Yeung and LL Leong. Effects of joint attributes on tunnel stability. *International Journal of Rock Mechanics and Mining Sciences*, 34(3-4):348–e1, 1997.
- [80] J-H Wu, Y Ohnishi, and S Nishiyama. Simulation of the mechanical behavior of inclined jointed rock masses during tunnel construction using discontinuous deformation analysis (DDA). *International Journal of Rock Mechanics and Mining Sciences*, 41(5):731–743, 2004.
- [81] M Tsesarsky and YH Hatzor. Tunnel roof deflection in blocky rock masses as a function of joint spacing and friction—a parametric study using discontinuous deformation analysis (DDA). *Tunnelling and Underground Space Technology*, 21(1):29–45, 2006.
- [82] J-H Wu. Seismic landslide simulations in discontinuous deformation analysis. *Computers and Geotechnics*, 37(5):594–601, 2010.

- [83] Y Zhang, G Chen, L Zheng, and Y Li. Numerical analysis of the largest landslide induced by the Wenchuan earthquake, may 12, 2008 using DDA. In *Earthquake-Induced Landslides*, pages 617–626. Springer, 2013.
- [84] Y Zhang, J Wang, Q Xu, G Chen, JX Zhao, and L Zheng. DDA validation of the mobility of earthquake-induced landslides. *Engineering Geology*, 194:38–51, 2015.
- [85] Y Ning, J Yang, X An, and G Ma. Simulation of blast induced crater in jointed rock mass by discontinuous deformation analysis method. *Frontiers of Architecture and Civil Engineering in China*, 4(2):223–232, 2010.
- [86] Y Ning, J Yang, X An, and G Ma. Modelling rock fracturing and blast-induced rock mass failure via advanced discretisation within the discontinuous deformation analysis framework. *Computers and Geotechnics*, 38(1):40–49, 2011.
- [87] CJ Pearce, A Thavalingam, Z Liao, and N Bićanić. Computational aspects of the discontinuous deformation analysis framework for modelling concrete fracture. *Engineering Fracture Mechanics*, 65(2-3):283–298, 2000.
- [88] G-H Shi. Three dimensional discontinuous deformation analyses. In *DC Rocks 2001, The 38th US Symposium on Rock Mechanics (USRMS)*, pages 1–21. American Rock Mechanics Association, 2001.
- [89] G-H Shi. Theory and examples of three dimensional discontinuous deformation analyses. *Frontiers of rock mechanics and sustainable development in the 21st century*, page 27, 2001.
- [90] S Beyabanaki, A Jafari, and MR Yeung. High-order three-dimensional discontinuous deformation analysis (3-D DDA). *International Journal for Numerical Methods in Biomedical Engineering*, 26(12):1522–1547, 2010.
- [91] YY Jiao, GH Huang, and Z Zhao. An improved three-dimensional spherical dda model for simulating rock failure. *Science China Technological Sciences*, 58(9):1533–1541, 2015.
- [92] S Beyabanaki and A Bagtzoglou. Sphere-boundary edge and sphere-boundary corner contacts model in DDA for simulating particulate media in 3-D. *Geomechanics and Geoengineering*, 10(2):83–94, 2015.
- [93] QH Jiang and MR Yeung. A model of point-to-face contact for three-dimensional discontinuous deformation analysis. *Rock Mechanics and Rock Engineering*, 37(2):95–116, 2004.

- [94] J-H Wu, CH Juang, and H Lin. Vertex-to-face contact searching algorithm for three-dimensional frictionless contact problems. *International Journal for Numerical Methods in Engineering*, 63(6):876–897, 2005.
- [95] MR Yeung, QH Jiang, and N Sun. A model of edge-to-edge contact for three-dimensional discontinuous deformation analysis. *Computers and Geotechnics*, 34(3):175–186, 2007.
- [96] JH Wu. New edge-to-edge contact calculating algorithm in three-dimensional discrete numerical analysis. *Advances in Engineering Software*, 39(1):15–24, 2008.
- [97] J Liu, X Kong, and G Lin. Formulations of the three-dimensional discontinuous deformation analysis method. *Acta Mechanica Sinica*, 20(3):270–282, 2004.
- [98] MR Yeung, QH Jiang, and N Sun. Validation of block theory and three-dimensional discontinuous deformation analysis as wedge stability analysis methods. *International journal of rock mechanics and mining sciences*, 40(2):265–275, 2003.
- [99] MR Yeung, N Sun, QH Jiang, and SC Blair. Analysis of large block test data using three-dimensional discontinuous deformation analysis. *International Journal of Rock Mechanics and Mining Sciences*, 41:521–526, 2004.
- [100] AR Keneti, A Jafari, and J Wu. A new algorithm to identify contact patterns between convex blocks for three-dimensional discontinuous deformation analysis. *Computers and Geotechnics*, 35(5):746–759, 2008.
- [101] SAR Beyabanaki, RG Mikola, and K Hatami. Three-dimensional discontinuous deformation analysis (3-D DDA) using a new contact resolution algorithm. *Computers and Geotechnics*, 35(3):346–356, 2008.
- [102] W Wu, H Zhu, X Zhuang, G Ma, and Y Cai. A multi-shell cover algorithm for contact detection in the three dimensional discontinuous deformation analysis. *Theoretical and Applied Fracture Mechanics*, 72:136–149, 2014.
- [103] R Grayeli and K Hatami. Implementation of the finite element method in the three-dimensional discontinuous deformation analysis (3D-DDA). *International journal for numerical and analytical methods in geomechanics*, 32(15):1883–1902, 2008.
- [104] W Wang, K Yin, G Chen, B Chai, Z Han, and J Zhou. Practical application of the coupled DDA-SPH method in dynamic modeling for the formation of

- landslide dam. *Landslides*, 16(5):1021–1032, 2019.
- [105] S Ji, A Ouahsine, H Smaoui, P Sergent, and G Jing. Impacts of ship movement on the sediment transport in shipping channel. *Journal of Hydrodynamics*, 26(5):706–714, 2014.
- [106] F Linde, A Ouahsine, N Huybrechts, and P Sergent. Three-dimensional numerical simulation of ship resistance in restricted waterways: Effect of ship sinkage and channel restriction. *Journal of Waterway, Port, Coastal, and Ocean Engineering*, 143(1):06016003, 2016.
- [107] S Ji, A Ouahsine, H Smaoui, and P Sergent. 3D modeling of sediment movement by ships-generated wakes in confined shipping channel. *International Journal of Sediment Research*, 29(1):49–58, 2014.
- [108] P Du, A Ouahsine, and Y Hoarau. Solid body motion prediction using a unit quaternion-based solver with actuator disk. *Comptes Rendus Mécanique*, 346(12):1136–1152, 2018.
- [109] S Whitaker. The Forchheimer equation: a theoretical development. *Transport in Porous media*, 25(1):27–61, 1996.
- [110] P Higuera, JL Lara, and IJ Losada. Three-dimensional interaction of waves and porous coastal structures using OpenFOAM®. part i: Formulation and validation. *Coastal Engineering*, 83:243–258, 2014.
- [111] FJ Mèndez, IJ Losada, and MA Losada. Mean magnitudes induced by regular waves in permeable submerged breakwaters. *Journal of Waterway, Port, Coastal, and Ocean Engineering*, 127(1):7–15, 2001.
- [112] MR Van Gent. Wave interaction with permeable coastal structures. *International Journal of Rock Mechanics and Mining Sciences and Geomechanics Abstracts*, 6(33):277A, 1996.
- [113] HG Guler, C Baykal, T Arikawa, and AC Yalciner. Numerical assessment of tsunami attack on a rubble mound breakwater using openfoam®. *Applied Ocean Research*, 72:76–91, 2018.
- [114] HG Weller. Derivation, modelling and solution of the conditionally averaged two-phase flow equations. *Nabla Ltd, No Technical Report TR/HGW*, 2:9, 2002.
- [115] LF Chen, J Zang, AJ Hillis, G Morgan, and AR Plummer. Numerical investigation of wave–structure interaction using OpenFOAM. *Ocean Engineering*,

88:91–109, 2014.

- [116] S Cai, A Ouahsine, J Favier, and Y Hoarau. Moving immersed boundary method. *International Journal for Numerical Methods in Fluids*, 85(5):288–323, 2017.
- [117] P Jiménez, F Thomas, and C Torras. 3D collision detection: a survey. *Computers & Graphics*, 25(2):269–285, 2001.
- [118] T-Y Ahn and J-J Song. New contact-definition algorithm using inscribed spheres for 3D discontinuous deformation analysis. *International Journal of Computational Methods*, 8(02):171–191, 2011.
- [119] RE Barbosa-Carrillo. *Discrete element models for granular materials and rock masses*. PhD thesis, Department of Civil and Environmental Engineering, University of Illinois at Urbana- Champaign, 1991.
- [120] Q Jiang. *Continuous change and organizational performance: An exploratory investigation of the perceptions of MBA and PhD business and technology graduates*. PhD thesis, Chinese Academy of Science, 2000.
- [121] PA Cundall. Formulation of a three-dimensional distinct element model—Part I. A scheme to detect and represent contacts in a system composed of many polyhedral blocks. *International Journal of Rock Mechanics and Mining Sciences & Geomechanics Abstracts*, 25(3):107–116, 1988.
- [122] EG Nezami, Y Hashash, D Zhao, and J Ghaboussi. A fast contact detection algorithm for 3-D discrete element method. *Computers and geotechnics*, 31(7):575–587, 2004.
- [123] D Höhner, S Wirtz, and V Scherer. A numerical study on the influence of particle shape on hopper discharge within the polyhedral and multi-sphere discrete element method. *Powder technology*, 226:16–28, 2012.
- [124] O Vorobiev. Simple common plane contact algorithm. *International journal for numerical methods in engineering*, 90(2):243–268, 2012.
- [125] Z-H Zhong. *Finite element procedures for contact-impact problems*. Oxford university press, 1993.
- [126] JH Wu, Y Ohnishi, GH Shi, and S Nishiyama. Theory of three-dimensional discontinuous deformation analysis and its application to a slope toppling at Amatoribashi, Japan. *International Journal of Geomechanics*, 5(3):179–195,

2005.

- [127] H Zhang, S Liu, G Chen, and L Zheng. Extension of three-dimensional discontinuous deformation analysis to frictional-cohesive materials. *International Journal of Rock Mechanics and Mining Sciences*, 86:65–79, 2016.
- [128] W Wu, X Wang, H Zhu, K-J Shou, J-S Lin, and H Zhang. Improvements in DDA program for rockslides with local in-circle contact method and modified open-close iteration. *Engineering Geology*, 265:105433, 2020.
- [129] L He and G Ma. Development of 3D numerical manifold method. *International Journal of Computational Methods*, 7(01):107–129, 2010.
- [130] A. Hadjidimos. Successive overrelaxation (SOR) and related methods. *Journal of Computational and Applied Mathematics*, 123(1):177–199, 2000.
- [131] AD Quinn, M Hayward, CJ Baker, F Schmid, JA Priest, and W Powrie. A full-scale experimental and modelling study of ballast flight under high-speed trains. *Journal of Rail and Rapid Transit*, 224(2):61–74, 2010.
- [132] G Jing, D Ding, and X Liu. High-speed railway ballast flight mechanism analysis and risk management—a literature review. *Construction and Building Materials*, 223:629–642, 2019.
- [133] A Sanz-Andres and F Navarro-Medina. The initiation of rotational motion of a lying object caused by wind gusts. *Journal of Wind Engineering and Industrial Aerodynamics*, 98(12):772–783, 2010.
- [134] A Premoli, D Rocchi, P Schito, C Somaschini, and G Tomasini. Ballast flight under high-speed trains: Wind tunnel full-scale experimental tests. *Journal of Wind Engineering and Industrial Aerodynamics*, 145:351–361, 2015.
- [135] MR Saat, FB Jacobini, and E Tutumluer. Identification of high-speed rail ballast flight risk factors and risk mitigation strategies. Technical report, U.S. Department of Transportation, Federal Railroad Administration, Office of Research and Development, Washington, DC 20590, 2015. Final report, No:DOT/FRA/ORD-15/03, 76 pages.
- [136] TR Loponen, P Salmenperä, H Luomala, and A Nurmikolu. Studies of snow-dropping from a train on a turnout due to dynamic excitations. *Journal of Cold Regions Engineering*, 32(2):04018003, 2018.
- [137] K Kawashima, S Iikura, T Endo, and T Fujii. Experimental studies on ballast-flying phenomenon caused by dropping of accreted snow/ice from

- high-speed trains. *Railway Technical Research Institute Report*, 17(8):31–36, 2003.
- [138] A Khayrullina, B Blocken, W Janssen, and J Straathof. CFD simulation of train aerodynamics: train-induced wind conditions at an underground railroad passenger platform. *Journal of wind engineering and industrial aerodynamics*, 139:100–110, 2015.
- [139] JY Zhu and ZW Hu. Flow between the train underbody and trackbed around the bogie area and its impact on ballast flight. *Journal of Wind Engineering and Industrial Aerodynamics*, 166:20–28, 2017.
- [140] C Paz, E Suárez, and C Gil. Numerical methodology for evaluating the effect of sleepers in the underbody flow of a high-speed train. *Journal of Wind Engineering and Industrial Aerodynamics*, 167:140–147, 2017.
- [141] F Xie, J Zhang, G Gao, K He, Y Zhang, and J Wang. Study of snow accumulation on a high-speed train’s bogies based on the discrete phase model. *Journal of Applied Fluid Mechanics*, 10(6):1729–1745, 2017.
- [142] G-H Shi and RE Goodman. Generalization of two-dimensional discontinuous deformation analysis for forward modelling. *International Journal for Numerical and Analytical Methods in Geomechanics*, 13(4):359–380, 1989.
- [143] JJ Petrovic. Review mechanical properties of ice and snow. *Journal of materials science*, 38(1):1–6, 2003.
- [144] FN Okonta. Effect of grading category on the roundness of degraded and abraded railway quartzites. *Engineering geology*, 193:231–242, 2015.
- [145] B Suhr and K Six. Parametrisation of a DEM model for railway ballast under different load cases. *Granular matter*, 19(4):64:1–16, 2017.
- [146] CJ Cho and Y Park. New monitoring technologies for overhead contact line at 400 km/h. *Engineering*, 2(3):360–365, 2016.
- [147] D Navikas and H Sivilevičius. Modelling of snow cover thickness influence on the railway construction temperature regime under variable weather conditions. *Procedia Engineering journal*, 187:124–134, 2017.
- [148] H Oumeraci. Review and analysis of vertical breakwater failures-lessons learned. *Coastal engineering*, 22(1-2):3–29, 1994.
- [149] S Takahashi, K Shimosako, K Kimura, and K Suzuki. Typical failures of composite breakwaters in Japan. *Coastal engineering*, pages 1899–1910,

2001.

- [150] H Takahashi, S Sassa, Y Morikawa, D Takano, and K Maruyama. Stability of caisson-type breakwater foundation under tsunami-induced seepage. *Soils and Foundations*, 54(4):789–805, 2014.
- [151] G Cuomo, W Allsop, T Bruce, and J Pearson. Breaking wave loads at vertical seawalls and breakwaters. *Coastal Engineering*, 57(4):424–439, 2010.
- [152] NS Doan, J Huh, V Mac, and D Kim. Probabilistic risk evaluation for overall stability of composite caisson breakwaters in Korea. *Journal of Marine Science and Engineering*, 8(3):148, 2020.
- [153] G Elchahal, R Younes, and P Lafon. The effects of reflection coefficient of the harbour sidewall on the performance of floating breakwaters. *Ocean Engineering*, 35(11-12):1102–1112, 2008.
- [154] B Hofland, M Kaminski, and G Wolters. Large scale wave impacts on a vertical wall. *Coastal Engineering Proceedings*, 1(32):15, 2010.
- [155] S Kocaman and H Ozmen-Cagatay. Investigation of dam-break induced shock waves impact on a vertical wall. *Journal of Hydrology*, 525:1–12, 2015.
- [156] S Liu, I Gatin, C Obhrai, MC Ong, and H Jasak. CFD simulations of violent breaking wave impacts on a vertical wall using a two-phase compressible solver. *Coastal Engineering*, 154:103564, 2019.
- [157] J-P Latham, J Mindel, J Xiang, R Guises, X Garcia, C Pain, and G Gorman. Coupled FEM DEM/Fluids for coastal engineers with special reference to armour stability and breakage. *Geomechanics and Geoengineering: An International Journal*, 4(1):39–53, 2009.
- [158] B Ren, Z Jin, R Gao, Y Wang, and Z Xu. SPH-DEM modeling of the hydraulic stability of 2D blocks on a slope. *Journal of Waterway, Port, Coastal, and Ocean Engineering*, 140(6):04014022, 2014.
- [159] T J Hsu, T Sakakiyama, and P Liu. A numerical model for wave motions and turbulence flows in front of a composite breakwater. *Coastal Engineering*, 46(1):25–50, 2002.
- [160] JC Alcérreca-Huerta and H Oumeraci. Wave-induced pressures in porous bonded revetments. part i: Pressures on the revetment. *Coastal Engineering*, 110:87–101, 2016.

- [161] Z Liang and D Jeng. A three-dimensional model for the seabed response induced by waves in conjunction with currents in the vicinity of an offshore pipeline using openfoam. *International Journal of Ocean and Coastal Engineering*, 1(03):1850004, 2018.
- [162] K Fang. A central numerical scheme to 1D Green-Naghdi wave equations. *Journal of Applied Mathematics and Physics*, 3(08):1032–1037, 2015.
- [163] M Martin-Medina, S Abadie, C Mokrani, and D Morichon. Numerical simulation of flip-through impacts of variable steepness on a vertical breakwater. *Applied Ocean Research*, 75:117–131, 2018.
- [164] J Lee, JE Skjelbreia, and F Raichlen. Measurement of velocities in solitary waves. *Journal of the Waterway, Port, Coastal and Ocean Division*, 108(2):200–218, 1982.
- [165] JS Do Carmo, JA Ferreira, L Pinto, and G Romanazzi. An improved serre model: Efficient simulation and comparative evaluation. *Applied Mathematical Modelling*, 56:404–423, 2018.
- [166] JS Do Carmo, JA Ferreira, and L Pinto. On the accurate simulation of nearshore and dam break problems involving dispersive breaking waves. *Wave Motion*, 85:125–143, 2019.
- [167] A Ouahsine, H Smaoui, K Meftah, and P Sergent. Numerical study of coastal sandbar migration, by hydro-morphodynamical coupling. *Environmental fluid mechanics*, 13(2):169–187, 2013.
- [168] JW Van der Meer, NWH Allsop, and T Bruce. Eurotop, 2016. manual on wave overtopping of sea defences and related structures. an overtopping manual largely based on european research, but for worldwide application. *EurOtop, London, UK*, page 264, 2016.
- [169] E Bilyay, B Ozbahceci, G Kiziroglu, and S Bacanli. A new approach to breakwater design-2B block. *Coastal Engineering Proceedings*, 1(35):39, 2017.
- [170] MR Yeung. *Application of Shi's discontinuous deformation analysis to the study of rock behavior*. University of California, Berkeley, 1991.
- [171] Ö Aydan, Y Shimizu, and Y Ichikawa. The effective failure modes and stability of slopes in rock mass with two discontinuity sets. *Rock Mechanics and Rock Engineering*, 22(3):163–188, 1989.

- [172] J Pan, Y Feng, F Jin, C Zhang, and D Owen. Comparison of different fracture modelling approaches to gravity dam failure. *Engineering Computations*, 2014.
- [173] Z Dong, X Ding, and S Huang. Analysis of deep dynamic sliding stability of gravity dam foundation based on DDA method. In *IOP Conference Series: Materials Science and Engineering*, volume 452, page 022100. IOP Publishing, 2018.
- [174] S Kaidi, A Ouahsine, M Rouainia, and H Smaoui. DDA in fluid-structure problems for the study of gravity dam failure. *European Journal of Computational Mechanics/Revue Européenne de Mécanique Numérique*, 19(5-7):533–546, 2010.
- [175] WW Marie and J Fredrik. System reliability of concrete dams with respect to foundation stability: application to a spillway. *Journal of geotechnical and geoenvironmental engineering*, 139(2):308–319, 2013.
- [176] A Krounis, F Johansson, J Spross, and S Larsson. Influence of cohesive strength in probabilistic sliding stability reassessment of concrete dams. *Journal of Geotechnical and Geoenvironmental Engineering*, 143(2):04016094, 2017.

List of publications

A.1 Articles

[1] Ding, D., Ouahsine, A., Xiao, W., Du, P. (2020). Numerical study of ballast-flight caused by dropping snow/ice blocks in high-speed railways using Discontinuous Deformation Analysis (DDA). *Transportation Geotechnics*, 22, 100314.

DOI: <https://doi.org/10.1016/j.trgeo.2019.100314>

Abstract: Frozen snow / ice blocks drop at high speeds from train causing the ballast to fly up and damage the car body. Thus, in this paper, we propose a numerical model based on the discontinuous deformation analysis (DDA) method to study the ballast flight caused by dropping snow / ice blocks in high-speed railways and to analyze the dynamic behavior of ballast particles during their collision with a snow / ice block. The validation of the proposed model is done by comparing the numerical results with the theoretical and the experimental ones. The numerical results show that the velocity, shape and incident angle of snow / ice block play an important role in the ballast flight. Specifically, the number and the maximum displacement of ballast particles increase as the train speed increases and the incident angle greatly affects the movement direction of ballast particles. The shape of the ice block affects the amount and extent of ballast flight.

Keywords: High speed railway; Ballast flight; Snow-dropping; Numerical modeling; Discontinuous deformation analysis

[2] Ding, D., Ouahsine, A., Xiao, W., Du, P. (2021). CFD/DEM coupled approach for the stability of caisson-type breakwater subjected to violent wave impact. *Ocean Engineering*, 223, 108651.

DOI: <https://doi.org/10.1016/j.oceaneng.2021.108651>

Abstract: Wave impacts on vertical caissons may cause breakwaters failures. This paper focuses on the analysis of the stability of breakwaters under violent wave

impacts by using a triple-coupled Fluid-Porous-Solid model. The fluid model is described by the Volume-Averaged Reynolds-Averaged Navier-Stokes equations in which the nonlinear Forchheimer equations for the porous medium are added to the inertia terms. The solid model, based on the DDA method which is an implicit DEM method, has been used to analyze the movement and the stability of the caisson and armour units by taking into account the shapes of the armor units, as well as the contact between blocks. The developed model has been used for multiple purposes. Firstly, to estimate the variation of the maximum height of the impacting wave with the breakwater slope. A new formula has then been established for this purpose. Secondly, to analyze the influence of the porosity and of the thickness of the porous layer on the Turbulence Kinetic Energy (TKE) distribution around the breakwater structure. The results show that the higher the thickness, the lower the TKE intensity will be. Finally, the model has been used to analyze the stability of shaped armour units placed behind the caisson.

Keywords: Breakwater stability; Violent wave impacts; Fluid-Porous model; CFD/-DEM coupling

A.2 Conferences

[1] Ding, D., Ouahsine, A., Discontinuous deformation analysis on ballast-flight phenomenon caused by dropping of accreted snow/ice from high-speed trains. The fourth international conference on railway technology-Railway (Railway2018). 3-7 September, 2018, Barcelona, Spain.

[2] Ding, D., Ouahsine, A., Numerical study of ballast-flying process caused by accreting snow/ice on high-speed trains by using the discontinuous deformation analysis (DDA). XXXIX Ibero-Latin American Congress on Computational Methods in Engineering (CILAMCE 2018), 11-14 November, 2018, Paris/Compiègne, France.

[3] Ding, D., Ouahsine, A., Study of ballast flight by using the Discontinuous deformation analysis. The fourth International Conference on Multi-scale Computational Methods for Solids and Fluids (ECCOMAS MSF 2019). 18 - 20 September ,2019, Sarajevo, Bosnia and Herzegovina.

